New constraints on the late Quaternary landscape evolution of the eastern Tibetan Plateau from 10Be and 26Al in-situ cosmogenic nuclides

Ye Yang, Cong-Qiang Liu, Jérôme van Der Woerd, Sheng Xu, Li-Feng Cui, Zhi-Qi Zhao, Qi-Lian Wang, Guo-Dong Jia, Francois Chabaux

New constraints on the late Quaternary landscape evolution of the eastern Tibetan Plateau from ^{10}Be and ^{26}Al in-situ cosmogenic nuclides

Ye Yang[a,b,c], Cong-Qiang Liu[a,b*], Jérôme Van der Woerd[d*], Sheng Xu[a*], Li-Feng Cui[b], Zhi-Qi Zhao[e,b], Qi-Lian Wang[b], Guo-Dong Jia[a], François Chabaux[c*]

[a] Institute of Surface-Earth System Science, Tianjin University, Tianjin 300072, China

[b] State Key Laboratory of Environmental Geochemistry, Institute of Geochemistry, Chinese Academy of Sciences, Guiyang 550081, China

[c] Laboratoire d'Hydrologie et de Géochimie de Strasbourg (LHyGeS), CNRS UMR 7517, University of Strasbourg, 1 rue Blessig, 67084 Strasbourg cedex, France

[d] Institut de Physique du Globe de Strasbourg (IPGS), CNRS UMR 7516, University of Strasbourg, 5 rue René Descartes, 67084 Strasbourg cedex, France

[e] School of Earth Sciences and Recourses, Chang'an University, Xi'an 710054, China

[*] Corresponding authors.

EE-mail addresses: liucongqiang@vip.skleg.cn (C.Q. Liu), fchabaux@unistra.fr (F. Chabaux)jerome.vanderwoerd@unistra.fr (J. Van der Woerd), sheng.xu@tju.edu.cn (S. Xu), fchabaux@unistra.fr (F. Chabaux).

Abstract

Based on Terrestrial Cosmogenic Nuclide (TCN) constraints from depth profiles of one granitic regolith from Wumingshan and five fluvial terraces from Xianshuihe and Zagunao rivers, we discuss the timing of the last deglaciation, the landscape-scale denudation and fluvial incision rates across the eastern Tibetan Plateau, in relation to previous work. We present a three-dimensional-graph visualization approach and corresponding constraints to better assess the feasibility and applicability of cosmogenic nuclides depth-profile dating. The exposure age (older than 19.4 ka) of the Wumingshan regolith corresponds to the retreat of the palaeo-Daocheng ice cap, which covered the Yidun terrane during the Last Glacial Maximum (LGM). Most basin-wide denudation rate data in the eastern Tibetan Plateau are lower than 130 mm/ka (47 %, n=90), which is consistent with the Wumingshan regolith denudation rate (lower than 52.8 mm/ka), and thus indicate that the landscape-scale denudation has been stabilized after the last deglaciation. Considering the reduction of integrated bulk density due to the accumulation of lower-density loess, we estimate mean exposure ages of Xianshuihe and Zagunao river terraces of 4.0 ± 0.7 ka, 5.9 ± 0.3 ka, 13.4 ± 2.0 ka, and 16.6 ± 1.4 ka. The observed increase in incision rate from 0.39 mm/yr over long timescale (~600 ka) to 5.88 mm/yr over the last 15 ka at the Xianshuihe river site is probably due to the transition from glacial to interglacial climatic

conditions. The fewer abandoned terraces along the Zagunao river after the Heinrich event 1 (H1) indicates that the climate change during the latest glacial-interglacial transition impacted less the landscape evolution in a relatively lower elevation area. Comparison with previously reported fluvial incision rates elsewhere across the eastern ~~Tibetan~~ margin of the Tibetan Plateau indicates that incision rates are mainly influenced by abrupt climate change or intensified summer monsoon since the early Holocene, but probably controlled by regional tectonic uplift or fluvial headward retreat as the timescale increases. Overall, we propose a synthetic pattern of landscape evolution mainly dominated by long-term tectonic uplift together with fluvial headward erosion, episodically influenced by climatic change throughout the late Quaternary.

Key words: Late Quaternary; Cosmogenic nuclides; Regolith; Denudation rate; Fluvial incision; Climate change; Eastern Tibetan Plateau

1. Introduction

Topography is a result of the interaction of tectonic uplift and fluvial incision modulated by climate on geological time scales (Molnar et al., 1994; Kirby et al., 2000; Hancock and Anderson, 2002; Clark et al., 2005; Liu-Zeng et al., 2008; Pan et al., 2009; Molnar et al., 2010; Ouimet et al.,

66 2010; Perrineau et al., 2011; Finnegan et al., 2014). The recent evolution
67 of the gentle gradient of the topography of the southeastern Tibetan
68 Plateau has been explained by two controversial models. On one hand,
69 topography is considered as the result of external processes involving a
70 wave of regressive development of rivers from the margin towards the
71 interior of an-already-high continental plateau, initiated by the onset of
72 the monsoon in the Miocene and modulated by climate (e.g., Métivier et
73 al., 1998; Tapponnier et al., 2001; Liu-Zeng et al., 2008; Roger et al.,
74 2010). On the other hand, it is interpreted as resulting from the recent
75 eastward spread of ductile lower crust from the plateau center towards its
76 rim (e.g., Burchfiel et al., 1995; Royden et al., 1997; Clark and Royden,
77 2000; Clark et al., 2005; Wang et al., 2012). Several approaches have
78 been used to independently constrain the rates of tectonic uplift, erosion
79 and the role of climate. Regional exhumation rates determined from
80 thermochronology or cosmogenic isotopes are classically used to discuss
81 the variations in space and time of regional uplift (Burbank et al., 1996;
82 Kirby et al., 2002; Godard et al., 2010; Ouimet et al., 2010; Ansberque et
83 al., 2015; Liu-Zeng et al., 2018; Tian et al., 2018). Fluvial terrace dating
84 is commonly used to determine rates of river incision (Kirby et al., 2000;
85 Liu et al., 2006; Chen et al., 2008b; Kong et al., 2009; Godard et al., 2010;
86 Zhao et al., 2013; He et al., 2015; Liu et al., 2015; Zhang et al., 2018).
87 The major issue with these approaches is how to disentangle regional

88 tectonic uplift, climate change, and river dynamics from both exhumation
89 and incision rates.
90 The objective of this study is to discuss our ability to determine tectonic
91 exhumation rates from river incision rates derived from well dated inset
92 terraces of two rivers in different tectonic setting (left-lateral strike-slip
93 Xianshuihe Fault system and Longmenshan thrust belt) using in situ
94 cosmogenic isotopes and by comparing these data with regionally
95 published data. The analysis of one granite regolith provides a perspective
96 to the coupling relationship between a surface erosive event caused by the
97 glacial advance and retreat, and the possible source of fluvial sediments.
98 This study also validates the methodology and emphasizes the need for
99 short- (10s ka) and long-term (several 100s ka) chronologies to be able to
100 constrain the long-term exhumation signal from the short-term climatic
101 response of river systems.
102
103 Fig. 1 about here.
104
105 **2. Geological setting and sample descriptions**
106 2.1. Study area
107 The eastern margin of the Tibetan Plateau is characterized by a low-relief,
108 upland erosion surface (Burchfiel et al., 1995; Royden et al., 1997; Clark
109 and Royden, 2000; Clark et al., 2004, 2005, 2006; Liu-Zeng et al., 2008)

that is drained by the Jinsha, Lancang (Mekong), Nu (Salween), and Yellow rivers (Fig. 1a). The geological structure of the study area is characterized by two main tectonic units: 1) the Songpan Ganzi fold belt including Triassic flysch intruded by a series of Jurassic granitic plutons, deformed Paleozoic rocks, crystalline Precambrian basement, low grade metamorphic Mesozoic sedimentary rocks, and limited Cenozoic sediments (e.g., Yin and Harrison, 2000; Roger et al., 2008); 2) the Longmenshan range made of exhumed crystalline rocks of the Yangtze craton and Paleozoic passive margin sediments (e.g., Burchfiel et al., 1995). Climatically, the study region has significant spatial and temporal variations in precipitation, which are dominated by the east Asian monsoon, the Indian monsoon, and the Westerlies (Fig. 1) (e.g., Maussion et al., 2014). Mean annual precipitation decreases from the margin (~2000 mm/yr) towards the plateau (lower than ~500 mm/yr) (Bookhagen, 2018, see Fig. 1b).

2.1.1. Wumingshan regolith

The sampling site (~4000 m above sea level, Table 1) is located in southern Yidun terrane (or Shaluli mountain), surrounded by the Qiangtang Terrane to west, the Songpan-Ganzi Fold Belt to northeast and the Yangtze Craton to southeast. It is bordered by the Jinshajiang Suture Zone (JSZ) in the west and Ganzi-Litang Suture Zone (GLSZ) in the east

(Fig. 1a). Wumingshan regolith is a typical granitic weathering product for studying the local landscape evolution in this area. The sampling location avoids the cover of loess and the presence of colluvial deposition to ensure that the granitic regolith is derived from the underlying bedrock and formed as a vertical weathering profile. The targeted bedrock is a Late Triassic granitic pluton with a zircon U-Pb age of 225 ± 2 Ma (Wu et al., 2017). The slope gradient of the hill is about 25°. Mean annual precipitation and temperature are, respectively, ~654.3 mm/yr and 4.8 °C for the period of 1981-2010 (data from National Meteorological Information Center, China; http://data.cma.cn/en). Previous works suggest that the palaeo-Daocheng Ice Cap with an extension of about 4000 km^2 covered the Yidun terrane during the Last Glacial Maximum (LGM) (Xu and Zhou, 2009; Fu et al., 2013; Zhang et al., 2015).

2.1.2. Xianshuihe and Zagunao fluvial terraces

The sampling sites of the fluvial terraces along the Xianshuihe river (~3150 m above sea level in our study area, Table 1), a tributary of the Yalong River (Fig. 1a), are located southeast of Luhuo County (Fig. 2b). The recent tectonic activity in this high continental plateau area is mainly controlled by the left-lateral strike-slip Xianshuihe Fault system (Fig. 1a) that triggered more than 20 earthquakes of magnitude higher than 6.5 since A.D. 1700, including the 2010 M_w 6.9 Yushu earthquake (Chevalier

et al., 2017, and references therein). Mean annual precipitation and temperature are, respectively, 694.0 mm/yr and 6.7 °C for the period of 1981-2010 (data from National Meteorological Information Center, China; http://data.cma.cn/en). The arcuate Xianshuihe segmented fault system mainly consists of the Yushu-Ganzi Faults (YGF) to the northwest, the Xianshuihe Fault (XSHF) in the middle, and the Xiaojiang Fault (XJF) to the southeast (Fig. 1a) (e.g., Wang and Burchfiel, 2000).

The sampling sites along the Zagunao river (~1800 m above sea level in our study area, Table 1), a tributary of the Minjiang river (Fig. 1a), are located in Li County (Fig. 2c), a few kilometers upstream the main faults of the Longmenshan thrust belt (LMSTB) at the eastern margin of the Tibetan Plateau. The active LMSTB and Minjiang Fault (MJF), along which the devastating 2008 M_w 7.9 Wenchuan and 2013 M_w 7.0 Lushan earthquakes occurred, play a main role in the evolution of topographic and structural features at the eastern margin of the Tibetan Plateau. Mean annual precipitation and temperature are, respectively, 619.2 mm/yr and 11.4 °C for the period of 1981-2010 (data from National Meteorological Information Center, China; http://data.cma.cn/en).

In these two study areas, the abandoned fluvial sediments are covered with over than 50 cm-thick loess at all the sampling sites. The widely distributed loess is proposed to originate from the arid interior of the Tibetan Plateau during the late Quaternary (Qiao et al., 2014; Hu et al.,

176 2015).

177

178 Fig. 2 about here.

179

180 2.2. Sampling strategy

181 Thirty ~4 kg samples, including granitic regolith, amalgamated sands and
182 sandy to pebbly gravels (Fig. 3), were collected (Fig. 1a). The artificial
183 road cuts, modern river erosion profiles and natural gullies (Fig. 3)
184 provided the ideal sampling sites. Samples were analyzed for in situ
185 cosmogenic ^{10}Be and ^{26}Al in quartz. A digital elevation model (DEM)
186 with 30 m resolution was constructed to determine the topographic
187 environment (data from Geospatial Data Cloud site, Computer Network
188 Information Center, Chinese Academy of Sciences;
189 http://www.gscloud.cn). Conservative uncertainties of 10% on elevations
190 were considered to account for field measurement error and
191 morphological roughness.

192 The Wumingshan regolith profile was sampled to constrain the recent
193 Quaternary weathering process and denudation rate of the granitic
194 bedrock. To avoid the disturbing effect of shallow soil in the 2 m-deep
195 profile, four deep samples were selected to determine the cosmogenic
196 nuclides concentration in quartz (Fig. 3a and Table 2).

197 Considering the complex deposition history of loess, three depth-profiles

198 and three deep burial samples were collected from the younger terraces in
199 the Xianshuihe fluvial terraces (Figs. 3c-e). Coarse-grained quartz (> 2
200 mm, XSH-5-1) and fine-grained quartz (< 2 mm, XSH-5-2) were
201 analyzed on duplicate samples to test the variability of inheritance in the
202 different quartz source regions (Table 2). Two depth profiles and four
203 deep burial samples (Table 2) were collected from the younger terraces in
204 the Zagunao fluvial terraces. These abandoned sediments were collected
205 to constrain the exposure age of the fluvial terraces and the incision rate
206 of the river. The loess mantle, the fine fraction (silt and soil), and the
207 coarse material (sand, pebbles, cobbles, and boulders) were assumed to
208 have densities of 1.4 ± 0.1, 1.6 ± 0.1, and 2.6 ± 0.1 g/cm^3, respectively.
209 The bulk density was calculated by estimating the proportion of fine and
210 coarse fractions using field photos and macroscopic description of the
211 horizons (Hancock et al., 1999; Perrineau et al., 2011; Guilbaud et al.,
212 2017).
213
214 **3. Analytical methods**
215 3.1. TCN sample preparation and analyses
216 Chemical preparation was performed at the cosmogenic nuclide
217 laboratory of Institut de Physique du Globe de Strasbourg (UMR_7516,
218 CNRS and University of Strasbourg, France) following standard methods
219 (e.g., Perrineau et al., 2011; Guilbaud et al., 2017). Samples were crushed

and sieved to fractions of 250-500 µm followed by magnetic and gravimetric separation. Oxides and carbonate matter were removed by HNO_3 leaching. Multiple overnight leaches in hot 1% HF/HNO_3 solutions were performed to remove the meteoric cosmogenic nuclides and to obtained purified quartz. Samples were dissolved in 5:1 HF/HNO_3 and spiked with ~250 mg of commercially available Scharlau ICP 1000 mg/l ^{9}Be standard (Table 2). Scharlau ICP 1000 mg/l ^{27}Al standard was added for samples with less than 2 mg of native ^{27}Al determined with ICP-MS AES at LHYGES (Table 2). Subsequently, the separation and purification by ion exchange chromatography, hydroxylation and oxidation were performed. BeO and Al_2O_3 were mixed with niobium and silver powder, respectively to make targets. The $^{10}Be/^{9}Be$ and $^{26}Al/^{27}Al$ ratios were measured on the ASTER AMS French national facility (CEREGE, Aix-en-Provence, France) (Table 2). $^{10}Be/^{9}Be$ and $^{26}Al/^{27}Al$ ratios were calibrated versus the ASTER in-house standard STD-11 ($^{10}Be/^{9}Be$ = (1.191 ± 0.013) × 10^{-11}) and SM-A1-11 (7.401 ± 0.064 × 10^{-12}), respectively (Arnold et al., 2010; Braucher et al., 2015). Both $^{10}Be/^{9}Be$ and $^{26}Al/^{27}Al$ ratios of processed blanks are approximately 3 × 10^{-15}.

3.2. Model setup

3.2.1. Chi-square modeling

Using the classical approximation that subsurface production rate can be

represented by exponential functions different for neutrons, slow muons and fast muons, (Granger and Smith, 2000; Schaller et al., 2002; Braucher et al., 2003, 2011, 2013; Hidy et al., 2010; Balco, 2017) and by making the presuppositions of steady erosion, average inheritance, and constant production rates, the expression of a measured nuclide concentration as a function of denudation rate, exposure age, and inheritance can be written in the following explicit form (Braucher et al., 2003, 2011; Siame et al., 2004; Rodés et al., 2011; Cui et al., 2014, 2016; 2014; Ackerer et al., 2016; Charreau et al., 2017; Schaller et al., 2018; Sordi et al., 2018):

$$C(x,\varepsilon,t) = c_0 e^{-\lambda t} + \sum_{i=spal,slow,fast} \frac{P_i}{\lambda + \frac{\rho_x}{\Lambda_i}\varepsilon} e^{-\frac{\rho_x}{\Lambda_i}x} [1 - e^{-(\lambda + \frac{\rho_x}{\Lambda_i}\varepsilon)t}] \qquad (1)$$

where $C(x,\varepsilon,t)$ is the present nuclide concentration, c_0 is the average cosmogenic inheritance (in at~~oms~~/g), ρ_x is the integrated bulk density at depth x , t is the exposure age, ε is the accumulation rate (negative) or denudation rate (positive), λ is the decay constant 5.00 × 10^{-7} yr^{-1} for ^{10}Be (Chmeleff et al., 2010; Korschinek et al., 2010) and 9.83 × 10^{-7} yr^{-1} for ^{26}Al (Nishiizumi, 2004), P_{spal}, P_{slow}, P_{fast} and Λ_{spal}, Λ_{slow}, Λ_{fast} are the surface production rates and attenuation lengths of neutrons, slow muons and fast muons, respectively. An exponential model for muon production rates provides an acceptable accuracy for shallow depth profiles and relatively slow denudation rates as found at our study sites. Therefore, the

simplified three exponential functions approximation for subsurface production rates was used in all calculations and modeling in this study. The production rates relative to sea level and high latitude (SLHL) as a function of geographic latitude and air pressure (Lal, 1991; Stone, 2000) are listed in Table 1. A global mean SLHL spallogenic production rate of 4.13 at~~om~~/($g_{(qtz)}$ yr) for ^{10}Be (Martin et al., 2017) and a ^{26}Al/^{10}Be spallogenic production ratio of 6.61 (Braucher et al., 2011) are used to scale the local production rates. We also include a correction factor for shielding by the surrounding topography using the online calculator of Balco et al. (2008) and regard the shielding by snow or vegetation as negligible. The spallogenic production rates uncertainty of ^{10}Be and ^{26}Al are assumed to be 7.2% and 10% (Phillips et al., 2016), respectively, after Borchers et al. (2016) by integrating the root mean square error of different previous study sites. Muons production rates (see Table 1) are scaled with atmospheric pressure and we ignore the latitudinal effect (Braucher et al., 2011). Depth scaling of production rates are based on attenuation lengths Λ_{spal}, Λ_{slow}, and Λ_{fast} of ~165, ~1500, and ~4320 g/cm^2 respectively (Braucher et al., 2011; Marrero et al., 2016). The best fit was performed by minimizing the chi-square value (Rodés et al., 2011, and references therein) as follows:

$$\chi^2 = \sum_{i=1}^{n} \left(\frac{C_i - C(x, \varepsilon, t)}{\sigma_{C_i}} \right)^2 \quad (2)$$

Where C_i are the measured concentration at x_i depth, and $C(x,\varepsilon,t)$ is the concentration predicted from Equation (1). Only the uncertainty of the measured concentration (σ_{C_i}) is considered because it would be impossible to simultaneously fit all parameters using only one measured concentration per sample (Borchers et al., 2016). Recently, in order to avoid the problem of "mixed estimator", the $\chi^2_{1\sigma}$ was replaced by the value of $\chi^2_{\min}+1$ (Guralnik et al., 2011; Saint-Carlier et al., 2016; Charreau et al., 2017; Delmas et al., 2018) to obtain the fitting values since the range of solutions is considered as a proxy for 1σ confidence level (Bevington and Robinson, 2003). To estimate the goodness of the fitting, the *p*-value of the chi-square best fit value has been used in this study, and *p*-values larger than 5% are considered as a valid prediction of the fitting model (Aster et al., 2013; Borchers et al., 2016; Phillips et al., 2016).

Fig. 3 about here.

3.2.2. A three-dimensional-graph visualization approach

Based on previous approaches (Braucher et al., 2009; Hidy et al., 2010; Rodés et al., 2011; Marrero et al., 2016), a visual, multi-interpreted, and robust depth-profile simulation approach was designed to model the three parameters (denudation rate, exposure age, and inheritance) for

cosmogenic nuclides depth profile (see detailed description in Appendix A-). In practice, the chi-square value can be minimized by a series of different denudation rate, exposure age, and inheritance values even when the *p*-value is close to 1 (see detail in Fig. S.1). The inability to obtain a unique solution is inevitable for the square sum function. However, to circumvent this difficulty, the bounds of denudation rate, exposure age, or inheritance are constrained by various reliable assumptions, such as the effective total denudation evidence (Hidy et al., 2010; Marrero et al., 2016), a zero denudation (Guralnik et al., 2011; Saint-Carlier et al., 2016), or a considered inheritance (Cui et al., 2016; Hidy et al., 2018). All the assumptions constrain the final fit, so we should be cautious when choosing the various reliable assumptions. Overall, the resulting ranges are sufficiently reliable to avoid over-constraining the inversion while discouraging the complex modeling to calculate the unreliable ranges that are considered to be less likely. Therefore, the 3D-graph visualization approach is used in this study to estimate the impact of the different assumptions and display the interactions among denudation rate, exposure age, and inheritance in one graph. This approach also emphasizes that any paired solutions of age and denudation rate are based on a given inheritance.

3.2.3. Variable-density approach

A significant loess cover is found covering the depth profiles, indicating that the assumption of a constant density based on the present-day outcrop, which includes the loess cover, is invalid. To account for the potential influence of loess after the abandonment of the fluvial terraces, we consider that the integrated bulk density composed of the lower-density covering loess and the higher-density underlying sediments increases or decreases constantly with time due to the denudation or accumulation of the loess in the study area. Equation (1) then becomes (see details in Appendix B.):

$$C(x,\varepsilon,t) = c_0 e^{-\lambda t} + \sum_{i=spal,slow,fast} \frac{P_i}{\lambda + \frac{\rho_{loess}}{\Lambda_i}\varepsilon} e^{-\left(\frac{\rho_{xsed}x_{sed}}{\Lambda_i} + \frac{\rho_{loess}x_{loess}}{\Lambda_i}\right)} \left[1 - e^{-\left(\lambda + \frac{\rho_{loess}}{\Lambda_i}\varepsilon\right)t}\right] \quad (3)$$

where x_{loess} is the current depth of the loess, ρ_{xsed} is the integrated bulk density of sediments at depth x_{sed}, and ρ_{loess} is the density of the loess (Fig. B.1, see details in Appendix B.).

To account for the potential effects of loess after abandonment of the fluvial terraces and without knowledge of the timing and rate of loess deposition, three different simplified deposition models have been used to model the exposure ages (e.g., Charreau et al., 2017). Model 1: instantaneous loess deposition after terrace abandonment and post-deposition constant denudation (maximum age); Model 2: continuous loess deposition at a constant accumulation rate after terrace

abandonment ("mean" age); Model 3: experience a constant terrace denudation before a very recent loess deposition event (minimum age; ignoring the attenuation in the loess) (Fig. B.1, see details in Appendix B-).

Fig. 4 about here.

4. Results

The concentrations of ^{26}Al and ^{10}Be show a linear relationship (Fig. 4a). The average ratio (~7.45) of $^{26}Al/^{10}Be$ is higher than the spallation production ratio of 6.61 (Braucher et al., 2011), which can be explained by the variation in $^{26}Al/^{10}Be$ ratio with increasing bedrock depth (Akçar et al., 2017). The $^{26}Al/^{10}Be$ ratios for all samples, excluding two anomalous results (XSH-5-1-2 and XSH-5-1-3), plot well in the steady state erosion island (Lal, 1991), which indicates that the pre-deposition burial history of the samples is negligible (Fig. 4b).

The results of the four cosmogenic nuclide ^{10}Be and ^{26}Al depth-profile saprolite samples (WMS1-11, WMS1-17, WMS1-22, and WMS1-26) are listed in Table 2 and supplementary Table 1. The ^{10}Be inversion of the depth profile, assuming the net erosion was no more than 100 cm ($\varepsilon \times t < 100$), constrains the age of the regolith to $27.0^{+9.6}_{-7.6}$ ka, the denudation rate to $18.4^{+14.4}_{-18.4}$ mm/ka, and the inheritance to $26.6^{+2.9}_{-3.1} \times 10^4$ at/g (Fig. 5a,

supplementary Table 1 and Fig. S.2). The constant inheritance is interpreted as a result of one erosive event caused by the impact of the last glacial period (see detail in section 5.2). Ignoring the constraint of net erosion, a minimum age of 19.4 ka and a maximum denudation rate of 52.8 mm/ka are obtained. The ^{26}Al inversion shows consistent results (see details in supplementary Table 1 and Fig. S.3). Similar ranges of age (21.6 - 38.6 ka), denudation rate (0 - 29.6 mm/ka) and ^{10}Be inheritance (23.3 - 28.4 $\times 10^4$ at/g) (see details in supplementary Table 1) are calculated when combining ^{26}Al and ^{10}Be cosmogenic nuclides (Rodés et al., 2011, 2014) by assuming negligible pre-deposition burial history, or with the simulator of Hidy et al. (2010; version 1.2) (age: 19.3 – 36.5 ka; denudation rate: 0 – 33.1 mm/ka; inheritance: 22.9 - 29.5 $\times 10^4$ at/g) (see details in Fig. S.4). Such a consistency between the three calculation approaches supports the reliability of the results derived from the depth profiles and the assumption of negligible burial history.

The whole cosmogenic nuclide analyses of fluvial terraces are presented in Table 2 and supplementary Table 2. According to the depth profiles, we calculated the surface exposure age, accumulation/denudation rate, and inheritance of the fluvial sediments using the three-dimensional chi-square inversion approach. Three different models (see details in Appendix B.) were used for each depth profile to estimate the impact caused by different loess deposition scenario. Based on the field

observations, a loess net erosion of less than 20 cm was assumed in Model 1 to constrain the wide range of free parameters. There are no obvious paleosoil between the loess and the fluvial sediments, conservatively, no more than 10 cm net erosion was assumed in Model 3 to constrain the 3D visualization inversion approach. The Model 2 inversion approach, assuming continuous deposition ($\varepsilon \times t = x_{loess}$) and considering the variation of the integrated bulk density, constrains the mean ^{10}Be exposure age to 4.0 ± 0.7 ka, 5.9 ± 1.3 ka, 13.4 ± 2.0 ka, and 16.6 ± 1.4 ka for the sites XSH-3 (T2), XSH-2 (T3), XSH-5 (T4), and ZGN-7 (T1), respectively (Figs. 4b-d, 4f and supplementary Table 2). The mean ^{26}Al exposure ages show consistent results (see details in Fig. S.3). Moreover, two end-member ages of the minimum exposure age (Model 1: instantaneous deposition of loess after terrace abandonment) and the maximum exposure age (Model 3: constant denudation before very recent loess deposition) are presented in Fig. 5 and supplementary Table 2.

Due to the scattering of the XSH-2 (T3) data and the small number of samples, the analytical quality of the XSH-2 (T3) age (5.9 ± 1.3 ka) is slightly less robust. However, this age is consistent with the position of T3 between T2 and T4 with ages of 4.0 ± 0.7 ka and 13.4 ± 2.0 ka, respectively (Fig. 5b). Owing to the tectonic activity and landslides in the Zagunao area (Figs. 2g and 2h), the data of the deepest (8 m) depth

profile (ZGN-2) cannot be fitted due to excessive scatter and insufficient number of samples. We used forward modeling (e.g., Perrineau et al., 2011), assuming no denudation and a two-stages deposition model to constrain the two ~~-stage ages~~ periods of exposure of ~2.0 ka and ~3.3 ka (Fig. 5e).

Coarse-grained quartz (2-10 mm, XSH-5-1) and fine-grained quartz (< 2 mm, XSH-5-2) were analyzed on 3 samples to test whether the various quartz grains have different inheritance values. The ^{10}Be results show very similar concentrations for the two shallow samples but a larger concentration for the deepest coarse-grained quartz. The difference observed in the deepest sample may be explained by a difference in the provenance of the coarse-grained quartz and fine-grained quartz. The coarse-grained quartz could be detached from resistant quartz veins, which have a longer residence time on the hillslopes (e.g., Codilean et al., 2014), recycled from the older sediments, thus with a longer exposure than the fresh rocks (e.g., Wittmann et al., 2011), or derived from the abrasion of cobbles exhumed at high elevations (e.g., Carretier et al., 2015). The result highlights the importance of grain size in the interpretation of cosmogenic nuclide data.

Fig. 6 about here.

5. Discussion

5.1. Feasibility and applicability of the three-dimensional-graph visualization approach for cosmogenic nuclides depth profile

The values derived from the three-dimensional-graph visualization approach provide a reliable estimate of exposure age, denudation rate, and inheritance. However, the chi-square value (Equation (3)) can be minimized for different sets of denudation rates, exposure ages, and inheritance values (e.g., Hidy et al., 2010; Borchers et al., 2016; Saint-Carlier et al., 2016). Even when a local minimum chi-square value is obtained, including the perfect fit of the data (p-value = 1), one can still get a series of possible solutions for exposure ages and denudation rates (Figs. S.1, S.2a and 2b). The self-check of the three-dimensional inversion approach indicates that the assumptions of negligible inheritance or subjective denudation rate should not be made to gain a seemingly plausible exposure age, e.g., exposure dating of surface samples (surface rock, surface sediments and moraine) and excessive constraints should not be imposed to the simulator. Therefore, independent constraints derived from the field investigations are essential to obtain a reliable solution (see details in section 4).

5.2. The timing of the last deglaciation revealed by receding glacier in the eastern Tibetan Plateau.

460 The glacial history of the eastern Tibetan Plateau has been investigated to
461 constrain the timing, extent and climatic conditions of paleoglaciations.
462 The evolution of regional paleoglaciations, which are a proxy for the
463 record of regional climate change (Clark et al., 2009), can be
464 reconstructed using precise dating methods such as ^{10}Be, radiocarbon
465 (^{14}C), optically stimulated luminescence (OSL), and electron spin
466 resonance (ESR). Although a series of glacial deposits is dated in the
467 study area (Fig. 6 and supplementary Table 3), the onset of the last
468 deglaciation still remains controversial (Schäfer et al., 2002; Owen et al.,
469 2003, 2005; Zhou et al., 2005; Kong et al., 2009; Xu and Zhou, 2009;
470 Heyman et al., 2011; Fu et al., 2013; Zhang et al., 2015). These previous
471 data (Fig. 6a) from Ganzi (Chevalier et al., 2017), Litang (Schäfer et al.,
472 2002; Graf et al., 2008; Fu et al., 2013), Daocheng (Xu et al., 2004; Wang
473 et al., 2006; Graf et al., 2008; Xu and Zhou, 2009; Fu et al., 2013; Zhang
474 et al., 2015), Queer mountain (Xu et al., 2010; Zhang et al., 2012; Ou et
475 al., 2013, 2014), and Kangding (Tschudi et al., 2003; Strasky et al., 2009;
476 Yan and Lin, 2017; Bai et al., 2018) provide evidence of two conspicuous
477 glacial advances: one during the Heinrich event 1 (H1) (Heinrich, 1988)
478 at about 16,800 yr (Hemming, 2004, and references therein) and the other
479 one during the Younger Dryas (YD) from 12,823 ± 60 yr to 11,473 ± 100
480 yr (Wang et al., 2001). In our study, the exposure age of ZGN-7 (~16.6 ka)
481 indicates that sediments were abandoned in the valleys and basins after

the LGM (Fig. 7b). Then, the age of ~13.4 ka (XSH-4) corresponds to the period between the H1 and YD glacial advances (Figs. 7a and 7b). Subsequently, the exposure age of XSH-2 (~5.9 ka) and XSH-3 (~4.0 ka) are consistent with the interval of monsoonal Himalayan-Tibetan stages (MOHITS) (Murari et al., 2014) or mid-Holocene climate optimum (Fig. 7b). The spatial and temporal distributions of published exposure or burial ages in the eastern Tibetan Plateau are presented in Fig. 6. We obtain an exposure age for the granitic regolith located in the Yidun terrane older than 19.4 ka (~~unconstraint~~unconstrained) or $27.0^{+9.6}_{-7.6}$ ka (with a net erosion less than 100 cm), which indicates that an erosive event occurred in this area approximately 20 ka ago, coincident with global Late Glacial Maximum (e.g., Clark et al., 2009), likely resulting from glacial or periglacial processes. This age is consistent with the presence of the palaeo-Daocheng ice cap during the LGM (Xu and Zhou, 2009; Fu et al., 2013; Zhang et al., 2015). This age is also found as a peak in the age distribution of Fig. 6c, indicating a regional event, and likely related to the glacial to interglacial transition at the end of the LGM. The profile shows inheritance within the regolith, which can be interpreted~~,~~ as proposed in other geographical contexts (e.g., Ackerer et al., 2016) as an evidence of a complex erosive history of the regolith marked by other intense glacial erosive events, prior to the erosive event at 20 ka. In addition, most basin-wide denudation rate data in the eastern Tibetan

504 Plateau are lower than 130 mm/ka (47 %, n=90) (Fig. 6b) and thus,
505 consistently with the regolith denudation rate (lower than 52.8 mm/ka),
506 ~~thus~~ indicate that the denudation of the landscape is demonstrably stable
507 following the last deglaciation.
508
509 Fig. 7 and 8 about here.
510
511 5.3. The framework for the late Quaternary fluvial incision in the eastern
512 Tibetan Plateau
513 The observation of variable incision rates provides insight into the
514 topographic and geomorphic evolution. Previous studies focused on the
515 onset of incision and paid less attention to the variation of the incision
516 rates after the incision began (Kirby et al., 2002; Clark et al., 2005;
517 Godard et al., 2009; Pan et al., 2009; Ouimet et al., 2010; Perrineau et al.,
518 2011). Fluvial incision rates, assumed to be in equilibrium with external
519 forcings over a wide range of timescales especially in a tectonically rising
520 landscape, were commonly interpreted as a proxy for the quantification of
521 tectonic uplift rate and indicating the strength of climate change under the
522 assumption of steady-state (Burbank et al., 1996; Maddy et al., 2000;
523 Kong et al., 2009; Pan et al., 2009; Huang et al., 2014; Ruszkiczay-
524 Rüdiger et al., 2016; Delmas et al., 2018). However, the significant effect
525 of lag time (Fig. 8) between uplift and incision indicates that the river

incision becomes periodically negligible in hyper-arid conditions or due to very low gravel flux (Whipple, 2004; Ouimet et al., 2010). In addition, the fluvial incision rate is exaggerated due to the fact that long episodic incision hiatuses, including river bed aggradation and return to pre-deposition (Fig. 8), are ignored (Gardner et al., 1987; Mills, 2000; Schumer and Jerolmack, 2009; Lague, 2010; Finnegan et al., 2014; Zhang et al., 2018). Fig. 8 shows a fluvial incision model to account for the relationship among fluvial incision, tectonic uplift and climate change at different timescales. Exaggerated fluvial incision rates at short timescale are seemingly caused by ignoring the hysteresis effect (e.g., Whipple and Tucker, 2002; Ouimet et al., 2010) and/or episodic hiatuses (e.g., Finnegan et al., 2014) (Fig. 8). The negative power-law dependence of bedrock river incision rate on different timescales (e.g., Schumer and Jerolmack, 2009) is used to interpret that the slopes (green and red dashed line in Fig. 8) decrease with increasing timescale.

On the long timescale of several million years, previous studies using multiple thermochronology methods suggest that the eastern margin of the Tibetan Plateau, including Minjiang ~~River~~, Dadu ~~River~~, Yalong ~~River~~, and Jinsha ~~River~~rivers, experienced high exhumation rates on the order of 0.2-1.0 mm/yr (e.g., Kirby et al., 2002; Clark et al., 2005; Godard et al., 2009; Ouimet et al., 2010; Tian et al., 2018) with initiation ages of ca. 8-15 Ma. Liu et al. (2006) and Zhao et al. (2013) propose that the Zagunao

548 and Xianhuihe rivers experience a relative stable average incision rate of
549 ~0.39 mm/yr over a long timescale (~600 ka) by using the ESR dating
550 method (Fig. 7d). Similar results of 0.5-0.8 mm/yr are obtained from river
551 watershed-averaged denudation rates along the Longmenshan range front
552 by using the river sediment load data (Liu-Zeng et al., 2011). The
553 consistency between these rates, representative of long-term processes
554 seemingly shows that the incision rate is a proxy for the tectonic uplift
555 rate. But, fluvial incision rates are not strictly equal to the tectonic uplift
556 rates in all circumstances (Gallen et al., 2015), especially at short
557 timescale. An increase incision rate from 1.32 ± 0.37 mm/yr (59.8 ± 16.9
558 ka) to 4.25 ± 0.76 mm/yr (10.6 ± 1.9 ka) is obtained in the Jinsha fluvial
559 terraces by using the OSL dating method (Chen et al., 2008b). ^{14}C, OSL,
560 and ^{10}Be data from terraces in the frontal region of the Longmenshan
561 show that the erosion rate is less than 0.5 ± 0.1 mm/yr (at the timescale of
562 150 ± 25 ka) and increases to ~1 mm/yr (at the timescale of 20-40 ka)
563 towards the west (Fig. 6a) (Godard et al., 2010). He et al. (2015) also
564 proposed an increase of the incision rate at the timescale of ~60 ka in the
565 lower reach of the Yalong river (Fig. 6a). In our study, a fast incision rate
566 of ~5.88 mm/yr for the last ~10 ka along the Xianshuihe river contrasts
567 with the long-term incision rate of ~0.39 mm/yr. The compilation of
568 previously reported fluvial incision rates (see detail in supplementary
569 Table 5) shows a peak of fast incision rates at the short timescale of ~10

570 ka in the eastern Tibetan Plateau (Fig. 7c). Our results show that the
571 fluvial incision rate varies by at least one order of magnitude depending
572 on the time scale of observation (Figs 6 and 7), implying decoupling
573 between regional long-term landscape erosion rates and fluvial incision
574 (e.g., Zhang et al., 2018). The slight increase of incision rate along the
575 Zagunao river may be due to its lower altitude, less frost shattering and
576 denser vegetation. According to the published data and our cosmogenic
577 ^{10}Be and ^{26}Al results, we propose that the fluvial incision rate is mainly
578 influenced by the abrupt climate change or the intensified summer
579 monsoon in the eastern Tibetan Plateau since the early Holocene (Chen et
580 al., 2008a), and controlled by tectonic uplift or progressive fluvial
581 headward retreat for longer timescales. These results emphasize the need
582 of the integration of data at several time scales to unravel the dynamic of
583 river incision and the role of the different processes operating at different
584 time scales (e.g., Mills, 2000; Whipple and Tucker, 2002; Finnegan et al.,
585 2014; Zhang et al., 2018).
586
587 5.4. An integrated driving mechanisms of landscape evolution in the
588 eastern Tibetan Plateau.
589 The competition between fluvial incision processes and tectonic uplift
590 processes is generally considered for the topographic and geomorphic
591 evolution of mountain belts (e.g., Burbank et al., 1996; Maddy et al.,

2000; Pan et al., 2009; Ruszkiczay-Rüdiger et al., 2016). In addition, the formation of fluvial terraces is mainly controlled by the synergistic effects of fluvial incision, tectonic uplift and climate change (e.g., Bull, 1991; Hancock and Anderson, 2002). However, quantifying the contributions of climate change and tectonic uplift from river incision rates is not straightforward. The great changes of flood magnitude and frequency caused by the climatic transitions are responsible for the formation of fluvial terraces (e.g., Chen et al., 2008b; Huang et al., 2014; He et al., 2015; Delmas et al., 2018; Zhang et al., 2018). During glacial periods, enhanced frost shattering and degradation of vegetation both caused an excess of sediment (on the slopes). Subsequently, these large amounts of sediments are transported in basins or valleys when the climate becomes warmer and wetter during interglacial, which is coupled to the erosive event that occurred on the bedrock surface of Wumingshan regolith (see detail in section 5.2). Because of reworking and/or recycling of the sediment not all glacial-interglacial transitions remain in the terrace record (purple shaded area in Fig. 8) (e.g., Cogez et al., 2018). Fluvial terraces emplaced during previous glacial terminations, as the last seven glacial terminations (Lisiecki and Raymo, 2005), are most probably reworked or recycled by subsequent glacial-interglacial transitions (Fig. 8). On the long-term, crustal isostatic rebound caused by the unloading as a result of deglaciation (e.g., Rohling et al., 2017) and surface

erosion/denudation processes (e.g., Burbank, 1992; Kirby et al., 2000) cannot be ignored (Whipple, 2009; Molnar, 2012). The information of fluvial incision has been recorded and its acceleration during the Holocene is likely the consequence of several processes: (i) the long-term tectonic uplift together with fluvial headward erosion; (ii) the short-term dramatic climate change at glacial-interglacial transitions; and (iii) the long-term isostatic rebound caused by the unloading as a result of deglaciation and surface denudation processes.

6. Conclusions

An integrated analysis of last deglaciation, local denudation and fluvial incision leads to the evaluation of landscape evolution, climate change and tectonic uplift in the eastern Tibetan Plateau. In this study, we obtain the exposure age older than 19.4 ka (or $27.0^{+9.6}_{-7.6}$ ka ~~under~~ without ~~constraint~~constraints) and the denudation rate lower than 52.8 mm/ka (or $18.4^{+14.4}_{-18.4}$ mm/kyr ~~under~~ without ~~constraint~~constraints) (Fig. 5) for the Wumingshan regolith (Yidun pluton) at the eastern ~~Tibet~~ margin of the Tibetan Plateau. These results coincide with the timing of the last deglaciation and reveal a stable landscape after the glacial or periglacial erosive event in this area. Our fluvial incision rates inferred from terrace ages, associated to previous river incision data show that the present fluvial incision rate is mainly influenced by the abrupt climate change or

636 the intensified summer monsoon in the eastern Tibetan Plateau since the
637 early Holocene, and that long-term incision rates are probably linked to
638 tectonic uplift or fluvial headward retreat. The driving mechanisms of
639 accelerated fluvial incision rate during the late Quaternary is interpreted
640 as the synthetic pattern of landscape evolution mainly dominated by long-
641 term tectonic uplift, periodically influenced by the climatic change and
642 isostasy throughout the late Quaternary.
643
644 **Acknowledgements**
645 Constructive comments by Régis Braucher and one anonymous reviewer
646 significantly improved the paper. The authors express gratitude to J.W.
647 Zhang, X.L. Zhang, G.W. Song, R.C. Ye for their help ~~of~~ for field
648 campaigns and sample preparation. We are grateful to René Boutin at
649 LHyGeS and ASTER Team (G. Aumaître, D. Bourlès, and K.
650 Keddadouche) at ASTER-CEREGE for ICP-~~MS~~ AES and AMS
651 measurements, respectively. The first author warmly thanks J. Liu-Zeng,
652 D. Fink and J. Ackerer for enlightening discussions. This work was
653 financially supported by the National Natural Science Foundation of
654 China (Nos. 41661144042, 41673124 and 41603018), the Second Tibetan
655 Plateau Scientific Expedition and Research (2019QZKK0707), and by the
656 INSU-CNRS, France and the University of Strasbourg to F. Chabaux and
657 J. Van der Woerd for the Al and Be concentration analyses at LHyGeS

658 and IPGS, and for $^{10}Be/^{9}Be$ and $^{26}Al/^{27}Al$ ratios measurements on the
659 Aster AMS facility (GEREGE, Aix-en-Provence, France) supported by
660 INSU-CNRS and IRD.
661
662 **Appendix A. The three-dimensional-graph visualization approach.**
663 According to the inequality derived by different confidence level of
664 $\chi^2 < \chi^2_{2\sigma}$, $\chi^2 < \chi^2_{1\sigma}$ or $\chi^2 < \chi^2_{\min} + 1$, one or more shaded area representing
665 all the possible solutions were yielded in the three-dimensional space
666 (Figs. A.1a and b). After a reliable constraint, the plot range of
667 denudation rate, exposure age, and inheritance need to be adjusted so that
668 the black points almost fill the three-dimensional space (Fig. A.1a, the
669 inset box shows the plot range of Fig. A.1b). We use the method of Rodés
670 et al. (2011) and Braucher et al. (2009) to generate a denudation-age-
671 inheritance space. The greater the number of points (can be adjusted by
672 the increments) in the shaded area, the higher the accuracy of the analysis.
673 In addition, it is a time-consuming process to yield a better statistical
674 analysis accuracy. Statistical analysis for all possible solutions in the
675 orange shaded area (Fig. A.1b), which represents a confidence level of
676 $\chi^2_{\min} + 1$, can yield the minimum, maximum, mean, mode, and median
677 solutions of denudation rate, exposure age, and inheritance, respectively
678 (supplementary Table 1). Figs. A.1c, d and e show the χ^2 plots for
679 denudation rate, exposure age, and inheritance values, and the inset

diagrams show the probability distribution functions (PDFs) and cumulative distribution functions (CDFs) for denudation rate, exposure age, and inheritance, respectively.

Appendix B. Constraint on the variable-density approach.

In order to model the complex geological process of the accumulated loess, we combine the method of Charreau et al. (2017) and the variable-density approach. The mean age and two end-member ages have been estimated from the modeling as follows:

Model 1: instantaneous deposition

If we consider that the loess was instantaneously deposited after terrace abandonment and subsequently experienced a constant denudation ($\varepsilon > 0$) (Fig. B.1a), the three free parameters (denudation rate, exposure age, and inheritance), described by Equation (3), are determined by the 3D visualization approach.

Model 2: continuous deposition

Continuous deposition at a constant accumulation rate ($\varepsilon < 0$) after terrace abandonment has been assumed to get the mean age (Fig. B.1b). In addition, the exposure age and accumulation rate are dependent on the total depth of loess ($x_{loess} = -\varepsilon \times t$). Then, Equation (3) becomes:

$$C(x,\varepsilon,t) = c_0 e^{-\lambda t} + \sum_{i=spal,slow,fast} \frac{P_i}{\lambda - \frac{\rho_{loess} x_{loess}}{\Lambda_i t}} e^{-\left(\frac{\rho_{xsed} x_{sed}}{\Lambda_i} + \frac{\rho_{loess} x_{loess}}{\Lambda_i}\right)} \left[1 - e^{-\left(\lambda t - \frac{\rho_{loess} x_{loess}}{\Lambda_i}\right)}\right]$$

(B.1)

In this case, the total depth of loess was used to constrain the 3D visualization approach. Two free parameters (exposure age and inheritance) were determined by the previous method (Siame et al., 2004; Rodés et al., 2011).

Model 3: Very recent deposition

In order to get the minimum end-member age, we assume the profile experienced a constant denudation before the very recent deposition of loess (Fig. B.1c). The 3D visualization approach with no variation of density was used to determine denudation rate, exposure age and inheritance.

References

Ackerer, J., Chabaux, F., Van der Woerd, J., Viville, D., Pelt, E., Kali, E., Lerouge, C., Ackerer, P., di Chiara Roupert, R., Négrel, P., 2016. Regolith evolution on the millennial timescale from combined U–Th–Ra isotopes and in situ cosmogenic ^{10}Be analysis in a weathering profile (Strengbach catchment, France). Earth Planet. Sci. Lett. 453, 33-43.

Akçar, N., Ivy-Ochs, S., Alfimov, V., Schlunegger, F., Claude, A., Reber, R., Christl, M., Vockenhuber, C., Dehnert, A., Rahn, M., Schlüchter, C., 2017. Isochron-burial dating of glaciofluvial deposits: First results from the Swiss Alps. Earth Surface Processes and Landforms 42, 2414-2425.

Ansberque, C., Godard, V., Bellier, O., De Sigoyer, J., Liu-Zeng, J., Xu, X., Ren, Z., Li, Y., Team, A.S.T.E.R., 2015. Denudation pattern across the Longriba fault system and implications for the geomorphological evolution of the eastern Tibetan margin. Geomorphology 246, 542-557.

Arnold, M., Merchel, S., Bourlès, D.L., Braucher, R., Benedetti, L., Finkel, R.C., Aumaître, G., Gottdang, A., Klein, M., 2010. The French accelerator mass spectrometry facility ASTER: Improved performance and developments. Nucl. Instrum. Methods Phys. Res. Sect. B-Beam Interact. Mater. Atoms 268, 1954-1959.

Aster, R.C., Borchers, B., Thurber, C.H., 2013. Parameter Estimation and Inverse Problems (Second Edition). Academic Press, Amsterdam.

Bai, M., Chevalier, M.-L., Pan, J., Replumaz, A., Leloup, P.H., Métois, M., Li, H., 2018. Southeastward increase of the late Quaternary slip-rate of the Xianshuihe fault, eastern Tibet. Geodynamic and seismic hazard implications. Earth Planet. Sci. Lett. 485, 19-31.

Balco, G., 2017. Production rate calculations for cosmic-ray-muon-produced 10 Be and 26 Al benchmarked against geological calibration data. Quat. Geochronol. 39, 150-173.

Balco, G., Stone, J.O., Lifton, N.A., Dunai, T.J., 2008. A complete and easily accessible means of calculating surface exposure ages or erosion rates from ^{10}Be and ^{26}Al measurements. Quat. Geochronol. 3, 174-195.

Bevington, P.R., Robinson, D.K., 2003. Data reduction and error analysis for the physical sciences. McGraw-Hill higher Education, New York.

Bond, G., Broecker, W., Johnsen, S., McManus, J., Labeyrie, L., Jouzel, J., Bonani, G., 1993. Correlations between climate records from North Atlantic sediments and Greenland ice. Nature 365, 143.

Bookhagen, B., 2018. High resolution spatiotemporal distribution of rainfall seasonality and extreme events based on a 12-year TRMM time series. in review.

Borchers, B., Marrero, S., Balco, G., Caffee, M., Goehring, B., Lifton, N., Nishiizumi, K., Phillips, F., Schaefer, J., Stone, J., 2016. Geological calibration of spallation production rates in the CRONUS-Earth project. Quat. Geochronol. 31, 188-198.

Braucher, R., Bourlès, D., Merchel, S., Vidal Romani, J., Fernadez-Mosquera, D., Marti, K., Léanni, L., Chauvet, F., Arnold, M., Aumaître, G., Keddadouche, K., 2013. Determination of muon attenuation lengths in depth profiles from in situ produced cosmogenic nuclides. Nucl. Instrum. Methods Phys. Res. Sect. B-Beam Interact. Mater. Atoms 294, 484-490.

Braucher, R., Brown, E.T., Bourlès, D.L., Colin, F., 2003. In situ produced ^{10}Be measurements at great depths: implications for production rates by fast muons. Earth Planet. Sci. Lett. 211, 251-258.

Braucher, R., Del Castillo, P., Siame, L., Hidy, A.J., Bourlès, D.L., 2009. Determination of both exposure time and denudation rate from an in situ-produced 10Be depth profile: A mathematical proof of uniqueness. Model sensitivity and applications to natural cases. Quat. Geochronol. 4, 56-67.

Braucher, R., Guillou, V., Bourlès, D.L., Arnold, M., Aumaître, G., Keddadouche, K., Nottoli, E., 2015. Preparation of ASTER in-house ^{10}Be/^{9}Be standard solutions. Nucl. Instrum. Methods Phys. Res. Sect. B-Beam Interact. Mater. Atoms 361, 335-340.

Braucher, R., Merchel, S., Borgomano, J., Bourlès, D.L., 2011. Production of cosmogenic radionuclides at great depth: A multi element approach. Earth Planet. Sci. Lett. 309, 1-9.

Bull, W.B., 1991. Geomorphic responses to climatic change. Oxford University Press, New York.

Burbank, D.W., 1992. Causes of recent Himalayan uplift deduced from deposited

776 patterns in the Ganges basin. Nature 357, 680-683.
777 Burbank, D.W., Leland, J., Fielding, E., Anderson, R.S., 1996. Bedrock incision, rock
778 uplift and threshold hillslopes in the northwestern Himalayas. Nature 379, 505.
779 Burchfiel, B.C., Chen, Z., Liu, Y., Royden, L.H., 1995. Tectonics of the Longmen
780 Shan and Adjacent Regions, Central China. Int. Geol. Rev. 37, 661-735.
781 Carretier, S., Regard, V., Vassallo, R., Aguilar, G., Martinod, J., Riquelme, R.,
782 Christophoul, F., Charrier, R., Gayer, E., Farías, M., Audin, L., Lagane, C., 2015.
783 Differences in ^{10}Be concentrations between river sand, gravel and pebbles along
784 the western side of the central Andes. Quat. Geochronol. 27, 33-51.
785 Charreau, J., Saint-Carlier, D., Dominguez, S., Lavé, J., Blard, P.-H., Avouac, J.-P.,
786 Jolivet, M., Chen, Y., Wang, S., Brown, N.D., Malatesta, L.C., Rhodes, E., 2017.
787 Denudation outpaced by crustal thickening in the eastern Tianshan. Earth Planet.
788 Sci. Lett. 479, 179-191.
789 Chen, F., Yu, Z., Yang, M., Ito, E., Wang, S., Madsen, D.B., Huang, X., Zhao, Y.,
790 Sato, T., John B. Birks, H., Boomer, I., Chen, J., An, C., Wünnemann, B., 2008a.
791 Holocene moisture evolution in arid central Asia and its out-of-phase
792 relationship with Asian monsoon history. Quat. Sci. Rev. 27, 351-364.
793 Chen, J., Dai, F., Yao, X., 2008b. Holocene debris-flow deposits and their
794 implications on the climate in the upper Jinsha River valley, China.
795 Geomorphology 93, 493-500.
796 Chevalier, M.-L., Leloup, P.H., Replumaz, A., Pan, J., Métois, M., Li, H., 2017.
797 Temporally constant slip rate along the Ganzi fault, NW Xianshuihe fault system,
798 eastern Tibet. Geol. Soc. Am. Bull. 130, 396-410.
799 Chmeleff, J., von Blanckenburg, F., Kossert, K., Jakob, D., 2010. Determination of
800 the ^{10}Be half-life by multicollector ICP-MS and liquid scintillation counting.
801 Nucl. Instrum. Methods Phys. Res. Sect. B-Beam Interact. Mater. Atoms 268,
802 192-199.
803 Clark, M.K., House, M.A., Royden, L.H., Whipple, K.X., Burchfiel, B.C., Zhang, X.,
804 Tang, W., 2005. Late Cenozoic uplift of southeastern Tibet. Geology 33, 525.
805 Clark, M.K., Royden, L.H., 2000. Topographic ooze: Building the eastern margin of
806 Tibet by lower crustal flow. Geology 28, 703-706.
807 Clark, M.K., Royden, L.H., Whipple, K.X., Burchfiel, B.C., Zhang, X., Tang, W.,
808 2006. Use of a regional, relict landscape to measure vertical deformation of the
809 eastern Tibetan Plateau. J. Geophys. Res.-Earth Surf. 111, F03002.
810 Clark, M.K., Schoenbohm, L.M., Royden, L.H., Whipple, K.X., Burchfiel, B.C.,
811 Zhang, X., Tang, W., Wang, E., Chen, L., 2004. Surface uplift, tectonics, and
812 erosion of eastern Tibet from large-scale drainage patterns. Tectonics 23,
813 TC1006.
814 Clark, P.U., Dyke, A.S., Shakun, J.D., Carlson, A.E., Clark, J., Wohlfarth, B.,
815 Mitrovica, J.X., Hostetler, S.W., McCabe, A.M., 2009. The Last Glacial
816 Maximum. Science 325, 710-714.
817 Codilean, A.T., Fenton, C.R., Fabel, D., Bishop, P., Xu, S., 2014. Discordance
818 between cosmogenic nuclide concentrations in amalgamated sands and
819 individual fluvial pebbles in an arid zone catchment. Quat. Geochronol. 19, 173-

180.
Cogez, A., Herman, F., Pelt, É., Reuschlé, T., Morvan, G., Darvill, C.M., Norton, K.P., Christl, M., Märki, L., Chabaux, F., 2018. U–Th and ^{10}Be constraints on sediment recycling in proglacial settings, Lago Buenos Aires, Patagonia. Earth Surface Dynamics 6, 121-140.
Cui, L.F., Liu, C.Q., Xu, S., Zhao, Z.Q., Liu, T.Z., Liu, W.J., Zhang, Z.J., 2016. Subtropical denudation rates of granitic regolith along a hill ridge in Longnan, SE China derived from cosmogenic nuclide depth-profiles. J. Asian Earth Sci. 117, 146-152.
Cui, L.F., Liu, C.Q., Xu, S., Zhao, Z.Q., Tu, C.L., Liu, T.Z., Ding, H., 2014. The long-term denudation rate of granitic regolith in Qinhuangdao, North China determined from the in situ depth profile of the cosmogenic nuclides ^{26}Al and ^{10}Be. Chin. Sci. Bull. 59, 4823-4828.
Delmas, M., Calvet, M., Gunnell, Y., Voinchet, P., Manel, C., Braucher, R., Tissoux, H., Bahain, J.-J., Perrenoud, C., Saos, T., 2018. Terrestrial ^{10}Be and electron spin resonance dating of fluvial terraces quantifies quaternary tectonic uplift gradients in the eastern Pyrenees. Quat. Sci. Rev. 193, 188-211.
Dykoski, C., Edwards, R., Cheng, H., Yuan, D., Cai, Y., Zhang, M., Lin, Y., Qing, J., An, Z., Revenaugh, J., 2005. A high-resolution, absolute-dated Holocene and deglacial Asian monsoon record from Dongge Cave, China. Earth Planet. Sci. Lett. 233, 71-86.
Finnegan, N.J., Schumer, R., Finnegan, S., 2014. A signature of transience in bedrock river incision rates over timescales of 10^4-10^7 years. Nature 505, 391-394.
Fu, P., Stroeven, A.P., Harbor, J.M., Hättestrand, C., Heyman, J., Caffee, M.W., Zhou, L., 2013. Paleoglaciation of Shaluli Shan, southeastern Tibetan Plateau. Quat. Sci. Rev. 64, 121-135.
Gallen, S.F., Pazzaglia, F.J., Wegmann, K.W., Pederson, J.L., Gardner, T.W., 2015. The dynamic reference frame of rivers and apparent transience in incision rates. Geology 43, 623-626.
Gao, Y.X., 1962. On some problems of Asian monsoon. In: Gao, Y.X. (Ed.), Some Problems on East-Asia Monsoon. Science Press, Beijing, pp. 49-63 (in Chinese).
Gardner, T.W., Jorgensen, D.W., Shuman, C., Lemieux, C.R., 1987. Geomorphic and tectonic process rates: effects of measured time interval. Geology 15, 259-261.
Godard, V., Lavé, J., Carcaillet, J., Cattin, R., Bourlès, D., Zhu, J., 2010. Spatial distribution of denudation in Eastern Tibet and regressive erosion of plateau margins. Tectonophysics 491, 253-274.
Godard, V., Pik, R., Lavé, J., Cattin, R., Tibari, B., de Sigoyer, J., Pubellier, M., Zhu, J., 2009. Late Cenozoic evolution of the central Longmen Shan, eastern Tibet: Insight from (U-Th)/He thermochronometry. Tectonics 28, TC5009.
Graf, A.A., Strasky, S., Zhao, Z., Akcar, N., Ivy-Ochs, S., Kubik, P.W., Christal, M., Kasper, H.U., Wieler, R., Schlüchter, C., 2008. Glacier extension on the eastern Tibetan Plateau in response to MIS 2 cooling, with a contribution to ^{10}Be and ^{21}Ne methodology. In: Strasky, S. (ed.), Glacial response to global climate changes: cosmogenic nuclide chronologies from high and low latitudes. ETH

Zürich (PhD Thesis).
Granger, D.E., Smith, A.L., 2000. Dating buried sediments using radioactive decay and muogenic production of ^{26}Al and ^{10}Be. Nucl. Instrum. Methods Phys. Res. Sect. B-Beam Interact. Mater. Atoms 172, 822-826.
Guilbaud, C., Simoes, M., Barrier, L., Laborde, A., Van der Woerd, J., Li, H., Tapponnier, P., Coudroy, T., Murray, A., 2017. Kinematics of Active Deformation Across the Western Kunlun Mountain Range (Xinjiang, China) and Potential Seismic Hazards Within the Southern Tarim Basin. J. Geophys. Res.-Solid Earth 122, 10398-10426.
Guralnik, B., Matmon, A., Avni, Y., Porat, N., Fink, D., 2011. Constraining the evolution of river terraces with integrated OSL and cosmogenic nuclide data. Quat. Geochronol. 6, 22-32.
Hancock, G.S., Anderson, R.S., 2002. Numerical modeling of fluvial strath-terrace formation in response to oscillating climate. Geol. Soc. Am. Bull. 114, 1131-1142.
Hancock, G.S., Anderson, R.S., Chadwick, O.A., Finkel, R.C., 1999. Dating fluvial terraces with ^{10}Be and ^{26}Al profiles: Application to the Wind River, Wyoming. Geomorphology 27, 41-60.
He, Z., Zhang, X., Qiao, Y., Bao, S., Lu, C., He, X., 2015. Formation of the Yalong Downstream Terraces in the SE Tibetan Plateau and Its Implication for the Uplift of the Plateau. Acta Geologica Sinica (English Edition) 89, 542-560.
Heinrich, H., 1988. Origin and consequences of cyclic ice rafting in the Northeast Atlantic Ocean during the past 130,000 years. Quat. Res. 29, 142-152.
Hemming, S.R., 2004. Heinrich events: Massive late Pleistocene detritus layers of the North Atlantic and their global climate imprint. Rev. Geophys. 42, RG1005.
Heyman, J., Stroeven, A.P., Caffee, M.W., Hättestrand, C., Harbor, J.M., Li, Y., Alexanderson, H., Zhou, L., Hubbard, A., 2011. Palaeoglaciology of Bayan Har Shan, NE Tibetan Plateau: exposure ages reveal a missing LGM expansion. Quat. Sci. Rev. 30, 1988-2001.
Hidy, A.J., Gosse, J.C., Pederson, J.L., Mattern, J.P., Finkel, R.C., 2010. A geologically constrained Monte Carlo approach to modeling exposure ages from profiles of cosmogenic nuclides: An example from Lees Ferry, Arizona. Geochem. Geophys. Geosyst. 11, Q0AA10.
Hidy, A.J., Gosse, J.C., Sanborn, P., Froese, D.G., 2018. Age-erosion constraints on an Early Pleistocene paleosol in Yukon, Canada, with profiles of ^{10}Be and ^{26}Al: Evidence for a significant loess cover effect on cosmogenic nuclide production rates. Catena 165, 260-271.
Hu, P., Liu, Q., Heslop, D., Roberts, A.P., Jin, C., 2015. Soil moisture balance and magnetic enhancement in loess–paleosol sequences from the Tibetan Plateau and Chinese Loess Plateau. Earth Planet. Sci. Lett. 409, 120-132.
Huang, W.-L., Yang, X.-p., Li, A., Thompson, J.A., Zhang, L., 2014. Climatically controlled formation of river terraces in a tectonically active region along the southern piedmont of the Tian Shan, NW China. Geomorphology 220, 15-29.
Kirby, E., Reiners, P.W., Krol, M.A., Whipple, K.X., Hodges, K.V., Farley, K.A.,

908 Tang, W., Chen, Z., 2002. Late Cenozoic evolution of the eastern margin of the
909 Tibetan Plateau: Inferences from $^{40}Ar/^{39}Ar$ and (U - Th)/He thermochronology.
910 Tectonics 21, 1-20.
911 Kirby, E., Whipple, K.X., Burchfiel, B.C., Tang, W., Berger, G., Sun, Z., Chen, Z.,
912 2000. Neotectonics of the Min Shan, China: Implications for mechanisms driving
913 Quaternary deformation along the eastern margin of the Tibetan Plateau. Geol.
914 Soc. Am. Bull. 112, 375-393.
915 Kong, P., Na, C., Fink, D., Zhao, X., Xiao, W., 2009. Moraine dam related to late
916 Quaternary glaciation in the Yulong Mountains, southwest China, and impacts
917 on the Jinsha River. Quat. Sci. Rev. 28, 3224-3235.
918 Korschinek, G., Bergmaier, A., Faestermann, T., Gerstmann, U.C., Knie, K., Rugel,
919 G., Wallner, A., Dillmann, I., Dollinger, G., von Gostomski, C.L., Kossert, K.,
920 Maiti, M., Poutivtsev, M., Remmert, A., 2010. A new value for the half-life of
921 10Be by Heavy-Ion Elastic Recoil Detection and liquid scintillation counting.
922 Nucl. Instrum. Methods Phys. Res. Sect. B-Beam Interact. Mater. Atoms 268,
923 187-191.
924 Lague, D., 2010. Reduction of long-term bedrock incision efficiency by short-term
925 alluvial cover intermittency. J. Geophys. Res.-Earth Surf. 115, F02011.
926 Lal, D., 1991. Cosmic ray labeling of erosion surfaces: in situ nuclide production rates
927 and erosion models. Earth Planet. Sci. Lett. 104, 424-439.
928 Lisiecki, L.E., Raymo, M.E., 2005. A Pliocene-Pleistocene stack of 57 globally
929 distributed benthic $\delta^{18}O$ records. Paleoceanography 20, 1-17.
930 Liu-Zeng, J., Tapponnier, P., Gaudemer, Y., Ding, L., 2008. Quantifying landscape
931 differences across the Tibetan plateau: Implications for topographic relief
932 evolution. J. Geophys. Res. 113, F04018.
933 Liu-Zeng, J., Wen, L., Oskin, M., Zeng, L., 2011. Focused modern denudation of the
934 Longmen Shan margin, eastern Tibetan Plateau. Geochem. Geophys. Geosyst. 12,
935 Q11007.
936 Liu-Zeng, J., Zhang, J., McPhillips, D., Reiners, P., Wang, W., Pik, R., Zeng, L.,
937 Hoke, G., Xie, K., Xiao, P., Zheng, D., Ge, Y., 2018. Multiple episodes of fast
938 exhumation since Cretaceous in southeast Tibet, revealed by low-temperature
939 thermochronology. Earth Planet. Sci. Lett. 490, 62-76.
940 Liu, J., Chen, J., Zhang, X., Li, Y., Rao, Z., Chen, F., 2015. Holocene East Asian
941 summer monsoon records in northern China and their inconsistency with Chinese
942 stalagmite δ18O records. Earth-Sci. Rev. 148, 194-208.
943 Liu, Y., Zhao, Z., Li, C., Zhang, M., Chen, Y., 2006. Formation of the Zagunao River
944 Terraces in Western Sichuan Plateau, China. Acta Geographica Sinica 61, 249-
945 254 (in Chinese with English abstract).
946 Maddy, D., Bridgland, D.R., Green, C.P., 2000. Crustal uplift in southern England:
947 evidence from the river terrace records. Geomorphology 33, 167-181.
948 Marrero, S.M., Phillips, F.M., Borchers, B., Lifton, N., Aumer, R., Balco, G., 2016.
949 Cosmogenic nuclide systematics and the CRONUScalc program. Quat.
950 Geochronol. 31, 160-187.
951 Martin, L.C.P., Blard, P.H., Balco, G., Lavé, J., Delunel, R., Lifton, N., Laurent, V.,

2017. The CREp program and the ICE-D production rate calibration database: A fully parameterizable and updated online tool to compute cosmic-ray exposure ages. Quat. Geochronol. 38, 25-49.

Maussion, F., Scherer, D., Mölg, T., Collier, E., Curio, J., Finkelnburg, R., 2014. Precipitation Seasonality and Variability over the Tibetan Plateau as Resolved by the High Asia Reanalysis. J. Clim. 27, 1910-1927.

Métivier, F., Gaudemer, Y., Tapponnier, P., Meyer, B., 1998. Northeastward growth of the Tibet plateau deduced from balanced reconstruction of two depositional areas: The Qaidam and Hexi Corridor basins, China. Tectonics 17, 823-842.

Mills, H.H., 2000. Apparent increasing rates of stream incision in the eastern United States during the late Cenozoic. Geology 28, 955-957.

Molnar, P., 2012. Isostasy can't be ignored. Nat. Geosci. 5, 83.

Molnar, P., Boos, W.R., Battisti, D.S., 2010. Orographic Controls on Climate and Paleoclimate of Asia: Thermal and Mechanical Roles for the Tibetan Plateau. Annual Review of Earth and Planetary Sciences 38, 77-102.

Molnar, P., Brown, E.T., Burchfiel, B.C., Deng, Q., Feng, X., Li, J., Raisbeck, G.M., Shi, J., Zhangming, W., Yiou, F., You, H., 1994. Quaternary Climate Change and the Formation of River Terraces across Growing Anticlines on the North Flank of the Tien Shan, China. J. Geol. 102, 583-602.

Murari, M.K., Owen, L.A., Dortch, J.M., Caffee, M.W., Dietsch, C., Fuchs, M., Haneberg, W.C., Sharma, M.C., Townsend-Small, A., 2014. Timing and climatic drivers for glaciation across monsoon-influenced regions of the Himalayan–Tibetan orogen. Quat. Sci. Rev. 88, 159-182.

Nishiizumi, K., 2004. Preparation of ^{26}Al AMS standards. Nucl. Instrum. Methods Phys. Res. Sect. B-Beam Interact. Mater. Atoms 223-224, 388-392.

North Greenland Ice Core Project, M., Andersen, K.K., Azuma, N., Barnola, J.M., Bigler, M., Biscaye, P., Caillon, N., Chappellaz, J., Clausen, H.B., Dahl-Jensen, D., Fischer, H., Flückiger, J., Fritzsche, D., Fujii, Y., Goto-Azuma, K., Grønvold, K., Gundestrup, N.S., Hansson, M., Huber, C., Hvidberg, C.S., Johnsen, S.J., Jonsell, U., Jouzel, J., Kipfstuhl, S., Landais, A., Leuenberger, M., Lorrain, R., Masson-Delmotte, V., Miller, H., Motoyama, H., Narita, H., Popp, T., Rasmussen, S.O., Raynaud, D., Rothlisberger, R., Ruth, U., Samyn, D., Schwander, J., Shoji, H., Siggard-Andersen, M.L., Steffensen, J.P., Stocker, T., Sveinbjörnsdóttir, A.E., Svensson, A., Takata, M., Tison, J.L., Thorsteinsson, T., Watanabe, O., Wilhelms, F., White, J.W.C., 2004. High-resolution record of Northern Hemisphere climate extending into the last interglacial period. Nature 431, 147-151.

Ou, X., Lai, Z., Zhou, S., Zeng, L., 2014. Timing of glacier fluctuations and trigger mechanisms in eastern Qinghai–Tibetan Plateau during the late Quaternary. Quat. Res. 81, 464-475.

Ou, X., Zhang, B., Lai, Z., Zhou, S., Zeng, L., 2013. OSL dating study on the glacial evolutions during the Last Glaciation at Dangzi Valley in the eastern Qinghai-Tibetan Plateau. Progress in Geography 32, 262-269 (in Chinese with English abstract).

Ouimet, W., Whipple, K., Royden, L., Reiners, P., Hodges, K., Pringle, M., 2010. Regional incision of the eastern margin of the Tibetan Plateau. Lithosphere 2, 50-63.

Owen, L.A., Finkel, R.C., Barnard, P.L., Haizhou, M., Asahi, K., Caffee, M.W., Derbyshire, E., 2005. Climatic and topographic controls on the style and timing of Late Quaternary glaciation throughout Tibet and the Himalaya defined by ^{10}Be cosmogenic radionuclide surface exposure dating. Quat. Sci. Rev. 24, 1391-1411.

Owen, L.A., Finkel, R.C., Haizhou, M., Spencer, J.Q., Derbyshire, E., Barnard, P.L., Caffee, M.W., 2003. Timing and style of Late Quaternary glaciation in northeastern Tibet. Geol. Soc. Am. Bull. 115, 1356-1364.

Pan, B., Su, H., Hu, Z., Hu, X., Gao, H., Li, J., Kirby, E., 2009. Evaluating the role of climate and tectonics during non-steady incision of the Yellow River: evidence from a 1.24 Ma terrace record near Lanzhou, China. Quat. Sci. Rev. 28, 3281-3290.

Perrineau, A., Van der Woerd, J., Gaudemer, Y., Liu-Zeng, J., Pik, R., Tapponnier, P., Thuizat, R., ~~Rongzhang, ~~Zheng, R.~~.~~, 2011. Incision rate of the Yellow River in Northeastern Tibet constrained by ^{10}Be and ^{26}Al cosmogenic isotope dating of fluvial terraces: implications for catchment evolution and plateau building. Geological Society, London, Special Publications 353, 189-219.

Phillips, F.M., Argento, D.C., Balco, G., Caffee, M.W., Clem, J., Dunai, T.J., Finkel, R., Goehring, B., Gosse, J.C., Hudson, A.M., Jull, A.J.T., Kelly, M.A., Kurz, M., Lal, D., Lifton, N., Marrero, S.M., Nishiizumi, K., Reedy, R.C., Schaefer, J., Stone, J.O.H., Swanson, T., Zreda, M.G., 2016. The CRONUS-Earth Project: A synthesis. Quat. Geochronol. 31, 119-154.

Qiao, Y., Qi, L., Liu, Z., Wang, Y., Yao, H., Yang, J., Zhao, Z., 2014. Intensification of aridity in the eastern margin of the Tibetan Plateau since 300ka BP inferred from loess-soil sequences, western Sichuan Province, southwest China. Paleogeogr. Paleoclimatol. Paleoecol. 414, 192-199.

Rodés, Á., Pallàs, R., Braucher, R., Moreno, X., Masana, E., Bourlès, D.L., 2011. Effect of density uncertainties in cosmogenic ^{10}Be depth-profiles: Dating a cemented Pleistocene alluvial fan (Carboneras Fault, SE Iberia). Quat. Geochronol. 6, 186-194.

Rodés, Á., Pallàs, R., Ortuño, M., García-Melendez, E., Masana, E., 2014. Combining surface exposure dating and burial dating from paired cosmogenic depth profiles. Example of El Límite alluvial fan in Huércal-Overa basin (SE Iberia). Quat. Geochronol. 19, 127-134.

Roger, F., Jolivet, M., Malavieille, J., 2008. Tectonic evolution of the Triassic fold belts of Tibet. C. R. Geosci. 340, 180-189.

Roger, F., Jolivet, M., Malavieille, J., 2010. The tectonic evolution of the Songpan-Garzê (North Tibet) and adjacent areas from Proterozoic to Present: A synthesis. J. Asian Earth Sci. 39, 254-269.

Rohling, E.J., Hibbert, F.D., Williams, F.H., Grant, K.M., Marino, G., Foster, G.L., Hennekam, R., de Lange, G.J., Roberts, A.P., Yu, J., Webster, J.M., Yokoyama, Y., 2017. Differences between the last two glacial maxima and implications for

ice-sheet, $\delta^{18}O$, and sea-level reconstructions. Quat. Sci. Rev. 176, 1-28.
Royden, L.H., Burchfiel, B.C., King, R.W., Wang, E., Chen, Z., Shen, F., Liu, Y., 1997. Surface Deformation and Lower Crustal Flow in Eastern Tibet. Science 276, 788-790.
Ruszkiczay-Rüdiger, Z., Braucher, R., Novothny, Á., Csillag, G., Fodor, L., Molnár, G., Madarász, B., 2016. Tectonic and climatic control on terrace formation: Coupling in situ produced ^{10}Be depth profiles and luminescence approach, Danube River, Hungary, Central Europe. Quat. Sci. Rev. 131, 127-147.
Saint-Carlier, D., Charreau, J., Lavé, J., Blard, P.-H., Dominguez, S., Avouac, J.-P., Wang, S., 2016. Major temporal variations in shortening rate absorbed along a large active fold of the southeastern Tianshan piedmont (China). Earth Planet. Sci. Lett. 434, 333-348.
Schäfer, J.M., Tschudi, S., Zhao, Z., Wu, X., Ivy-Ochs, S., Wieler, R., Baur, H., Kubik, P.W., Schlüchter, C., 2002. The limited influence of glaciations in Tibet on global climate over the past 170 000 yr. Earth Planet. Sci. Lett. 194, 287-297.
Schaller, M., Ehlers, T.A., Lang, K.A.H., Schmid, M., Fuentes-Espoz, J.P., 2018. Addressing the contribution of climate and vegetation cover on hillslope denudation, Chilean Coastal Cordillera (26°–38°S). Earth Planet. Sci. Lett. 489, 111-122.
Schaller, M.F., von Blanckenburg, F., Veldkamp, A., Tebbens, L.A., Hovius, N., Kubik, P.W., 2002. A 30000 yr record of erosion rates from cosmogenic ^{10}Be in Middle European river terraces. Earth Planet. Sci. Lett. 204, 307-320.
Schumer, R., Jerolmack, D.J., 2009. Real and apparent changes in sediment deposition rates through time. J. Geophys. Res. 114, F00A06.
Siame, L., Bellier, O., Braucher, R., Sébrier, M., Cushing, M., Bourlès, D., Hamelin, B., Baroux, E., de Voogd, B., Raisbeck, G., Yiou, F., 2004. Local erosion rates versus active tectonics: cosmic ray exposure modelling in Provence (south-east France). Earth Planet. Sci. Lett. 220, 345-364.
Sordi, V.D.M., Salgado, A.A.R., Siame, L., Bourlès, D., Paisani, J.C., Léanni, L., Braucher, R., Couto, V.d.E., Team, A., 2018. Implications of drainage rearrangement for passive margin escarpment evolution in southern Brazil. Geomorphology 306, 155-169.
Stone, J.O., 2000. Air pressure and cosmogenic isotope production. J. Geophys. Res.-Solid Earth 105, 23753-23759.
Strasky, S., Graf, A.A., Zhao, Z., Kubik, P.W., Baur, H., Schlüchter, C., Wieler, R., 2009. Late Glacial ice advances in southeast Tibet. J. Asian Earth Sci. 34, 458-465.
Tapponnier, P., ~~Zhiqin, X~~Xu, Z., Roger, F., Meyer, B., Arnaud, N., Wittlinger, G., ~~Jingsui,~~ Yang J., 2001. Oblique stepwise rise and growth of the Tibet plateau. Science 294, 1671-1677.
Taylor, M., Yin, A., 2009. Active structures of the Himalayan-Tibetan orogen and their relationships to earthquake distribution, contemporary strain field, and Cenozoic volcanism. Geosphere 5, 199-214.
Tian, Y., Li, R., Tang, Y., Xu, X., Wang, Y., Zhang, P., 2018. Thermochronological

Constraints on the Late Cenozoic Morphotectonic Evolution of the Min Shan, the Eastern Margin of the Tibetan Plateau. Tectonics 37, 1733-1749.
Tschudi, S., Schäfer, J.M., Zhao, Z., Wu, X., Ivy-Ochs, S., Kubik, P.W., Schlüchter, C., 2003. Glacial advances in Tibet during the Younger Dryas? Evidence from cosmogenic ^{10}Be, ^{26}Al, and ^{21}Ne. J. Asian Earth Sci. 22, 301-306.
Vermeesch, P., 2007. CosmoCalc: An Excel add-in for cosmogenic nuclide calculations. Geochem. Geophys. Geosyst. 8, Q08003.
Wang, E., Burchfiel, B.C., 2000. Late Cenozoic to Holocene deformation in southwestern Sichuan and adjacent Yunnan, China, and its role in formation of the southeastern part of the Tibetan Plateau. Geol. Soc. Am. Bull. 112, 413-423.
Wang, E., Kirby, E., Furlong, K.P., van Soest, M., Xu, G., Shi, X., Kamp, P.J.J., Hodges, K.V., 2012. Two-phase growth of high topography in eastern Tibet during the Cenozoic. Nat. Geosci. 5, 640-645.
Wang, J., Raisbeck, G.M., Xu, X., Yiou, F., Bai, S., 2006. In situ cosmogenic 10Be dating of the Quaternary glaciations in the southern Shaluli Mountain on the Southeastern Tibetan Plateau. Science in China Series D: Earth Sciences 49, 1291-1298.
Wang, Y.J., Cheng, H., Edwards, R.L., An, Z.S., Wu, J.Y., Shen, C.C., Dorale, J.A., 2001. A high-resolution absolute-dated late Pleistocene Monsoon record from Hulu Cave, China. Science 294, 2345-2348.
Whipple, K.X., 2004. Bedrock Rivers and the Geomorphology of Active Orogens. Annual Review of Earth and Planetary Sciences 32, 151-185.
Whipple, K.X., 2009. The influence of climate on the tectonic evolution of mountain belts. Nat. Geosci. 2, 97.
Whipple, K.X., Tucker, G.E., 2002. Implications of sediment-flux-dependent river incision models for landscape evolution. J. Geophys. Res.-Solid Earth 107, ETG 3-1-ETG 3-20.
Wittmann, H., von Blanckenburg, F., Maurice, L., Guyot, J.L., Kubik, P.W., 2011. Recycling of Amazon floodplain sediment quantified by cosmogenic ^{26}Al and ^{10}Be. Geology 39, 467-470.
Wu, T., Xiao, L., Wilde, S.A., Ma, C.-Q., Zhou, J.-X., 2017. A mixed source for the Late Triassic Garzê-Daocheng granitic belt and its implications for the tectonic evolution of the Yidun arc belt, eastern Tibetan Plateau. Lithos 288-289, 214-230.
Xu, L., Ou, X., Lai, Z., Zhou, S., Wang, J., Fu, Y., 2010. Timing and style of Late Pleistocene glaciation in the Queer Shan, northern Hengduan Mountains in the eastern Tibetan Plateau. J. Quat. Sci. 25, 957-966.
Xu, L., Zhou, S., 2009. Quaternary glaciations recorded by glacial and fluvial landforms in the Shaluli Mountains, Southeastern Tibetan Plateau. Geomorphology 103, 268-275.
Xu, X., Wang, J., Zhu, J., Jiang, H., Yang, Y., 2004. Study on glacial erosion surface of the southeast of Qinghai-Xizang Plateau using cosmogenic isotopes dating. Scientia Geographica Sinica 24, 101-104 (in Chinese with English abstract).
Yan, B., Lin, A., 2017. Holocene activity and paleoseismicity of the Selaha Fault, southeastern segment of the strike-slip Xianshuihe Fault Zone, Tibetan Plateau.

Tectonophysics 694, 302-318.
Yin, A., Harrison, T.M., 2000. Geologic Evolution of the Himalayan-Tibetan Orogen. Annual Review of Earth & Planetary Sciences 28, 211-280.
Yuan, D., Cheng, H., Edwards, R.L., Dykoski, C.A., Kelly, M.J., Zhang, M., Qing, J., Lin, Y., Wang, Y., Wu, J., Dorale, J.A., An, Z., Cai, Y., 2004. Timing, Duration, and Transitions of the Last Interglacial Asian Monsoon. Science 304, 575-578.
Zhang, B., Ou, X., Lai, Z., 2012. OSL ages revealing the glacier retreat in the Dangzi valley in the eastern Tibetan Plateau during the Last Glacial Maximum. Quat. Geochronol. 10, 244-249.
Zhang, J., Liu-Zeng, J., Scherler, D., Yin, A., Wang, W., Tang, M., Li, Z., 2018. Spatiotemporal variation of late Quaternary river incision rates in southeast Tibet, constrained by dating fluvial terraces. Lithosphere 10, 662-675.
Zhang, Z., Wang, J., Xu, X., BAI, S., Chang, Z.Y., 2015. Cosmogenic ^{10}Be and ^{26}Al Chronology of the Last Glaciation of the Palaeo-Daocheng Ice Cap, Southeastern Qinghai-Tibetan Plateau. Acta Geologica Sinica (English Edition) 89, 575-584.
Zhao, Z.J., Liu, Y., Chen, Y., Zhang, M.H., Shu, Q., Li, C.L., 2013. Quaternary fluvial incision rates of the Western Sichuan Plateau inferred from ESR chronology. Journal of Lanzhou University 49, 160-172 (in Chinese with English abstract).
Zhou, S., Xu, L., Cui, J., Zhang, X., Zhao, J., 2005. Geomorphologic evolution and environmental changes in the Shaluli Mountain region during the Quaternary. Chin. Sci. Bull. 50, 52-57.

Figure captions

Fig. 1. (a) Topographic map of eastern Tibetan Plateau based on 90-m-resolution Shuttle Radar Topography Mission (SRTM) digital elevation model and major geologic structures (modified from Tapponnier et al., 2001; Clark et al., 2005; Taylor and Yin, 2009; Wu et al., 2017; Liu-Zeng et al., 2018). YGF, Yushu-Ganzi Fault; XSHF, Xianshuihe Fault; ANHF, Anninghe Fault; XJF, Xiaojiang Fault; LTF, Litang Fault; MJF, Minjiang Fault; KLF, Kunlun Fault; XJG, Xiaojinhe Fault; BRKF, Barkam Fault; DSF, Dianshan Fault; BNSZ, Bangongcuo-Nujiang Suture Zone; JSZ, Jinshajiang Suture Zone; GLSZ, Ganzi-Litang Suture Zone; LMSTB, Longmenshan Thrust Belt. Inset: Location of study area. Dashed line represents

transition between Eastern Asian monsoon, Indian monsoon and Westerlies (Gao, 1962). (b) Spatial distribution of annually averaged precipitation in eastern Tibetan Plateau from Tropical Rainfall Measuring Mission (TRMM) data (Bookhagen, 2018).

Fig. 2. Sample locations of Wumingshan regolith (a and -d), Xianshuihe (b and -e) and Zagunao rivers (c and -f), superimposed on shaded relief and contour lines, respectively. (g) and (h) show cross-profile sketchs for Xianshuihe and Zagunao fluvial terrace sequences. Red bars indicate sampling sites of depth profiles. Green bars are burial samples. In b, black line is approximate position of synthetic section of figure 8.

Fig. 3. (a-b) Field photographs of Wumingshan regolith showing the vertical section with clear boundary between bedrock and overlying saprolite. (c-e) Field photographs showing location of sampling sites above Xianshuihe river and thick loess cover. (f-g) Field photographs showing five levels of fluvial terraces above Zagunao river and (h) important slope instabilities.

Fig. 4. (a) Correlation of ^{10}Be and ^{26}Al concentrations. Solid line is best fit, excluding two outliers (grey circles). Black dashed line presents production ratio of ^{26}Al/^{10}Be = 6.61 following Braucher et al. (2011). (b) Normalized ^{26}Al/^{10}Be ratios plotted against ^{10}Be concentrations (modified from Vermeesch (2007) and scaled to SLHL).

1183 Steady-state erosion island (shaded yellow) showing saturation values for $^{26}Al/^{10}Be$
1184 for different erosion rates (red line). Open ellipses represent depth profile samples
1185 with 2σ uncertainties. Shaded grey ellipses are burial samples, excluding two
1186 outliers (dashed ellipses).
1187
1188 Fig. 5. Cosmogenic ^{10}Be depth profile data, field photographs and integrated bulk
1189 density of Wumingshan regolith (a), Xianshuihe (b, c, and d) and Zagunao rivers (e
1190 and f). Orange and blue curves show fitting solutions that match χ^2 values within
1191 limits of $[\chi^2_{min}; \chi^2_{min}+1]$ and best group with smallest χ^2 values ($\chi^2_{min} \times 1.01$),
1192 respectively. Red curves show variation of nuclide concentration in loess under the
1193 assumption of a constant inheritance. Inset text gives exposure age, denudation rate,
1194 and inheritance. Solid and dashed green lines, respectively, show integrated bulk
1195 density and bulk density. Purple curve shows forward model solution (e.g.,
1196 Perrineau et al., 2011) with two-stages model.
1197
1198 Fig. 6. (a) Spatial distribution of previous exposure/burial ages (circle), basin-wide
1199 denudation rates (triangle), and fluvial incision rates (square) over eastern Tibetan
1200 Plateau (data in supplementary Tables 3-5). (b) Distribution of basin-wide
1201 denudation rates for modern river sediments. We excluded 18 outliers greater than
1202 800 mm/ka (data in supplementary Table 3). (c) Distribution of exposure and burial
1203 ages (data in supplementary Table 4). Red curve represents relative probability
1204 density function with 1σ error.

Fig. 7. Comparison of fluvial terraces abandonment ages with b) paleoclimatic records from North Greenland Ice Core Project (NGRIP) oxygen isotope record (North Greenland Ice Core Project et al., 2004), Hulu cave stalagmites oxygen isotope record (Wang et al., 2001), Dongge cave stalagmites oxygen isotope record (Yuan et al., 2004; Dykoski et al., 2005), and e) stacked Benthic oxygen isotope curve (Lisiecki and Raymo, 2005). Blue dashed lines in (a) and (d) show linear relationship between terrace elevations and abandonment ages at different timescales. Yellow bands in (b) indicate timing and duration of Younger Dryas (YD) and Heinrich events 1 and 2 (H1 and H2) (Bond et al., 1993; Hemming, 2004). Purple bands in (b) represent continuous glaciation termed monsoonal Himalayan-Tibetan stages (MOHITS) from MOHITS 1A to MOHITS 2D (Murari et al., 2014). Previous data in (c) are presented in supplementary Table 5. ESR ages of Xianshuihe and Zagunao rivers are from Zhao et al. (2013) and Liu et al. (2006), respectively. Red numbers in (d) represent average incision rate from formation of terrace to present.

Fig. 8. Simplified model to illustrate river bed evolution of Xianshuihe river and relationship between bedrock erosion, fluvial incision and terrace formation and abandonment. Yellow bars show the lag time between uplift and incision, when river incision is periodically cancelled during hyper-arid conditions or low sediment discharge (e.g., Whipple, 2004; Ouimet et al., 2010). Blue bars show

episodic incision hiatuses, including river bed aggradation and return to pre-deposition (e.g., Finnegan et al., 2014). TCN and ESR ages are from this study and Zhao et al. (2013), respectively.

Figure captions in Appendix

Fig. A.1. ~~A t~~Three-dimensional-graph visualization approach and statistical analysis of possible solutions. Data from Ackerer et al. (2016). (a) purple and black points represent possible solutions within 2σ and 1σ confidence levels, respectively; (b) black and orange points represent possible solutions within 1σ confidence level and $\chi^2_{\min}+1$, respectively (see detail in Appendix A); (c-e) χ^2 value plots for denudation rate, exposure age and inheritance, in addition, inset diagrams show probability distribution functions (PDFs) and cumulative distribution functions (CDFs); (f) Cosmogenic nuclide concentration as a function of depth for possible solutions within confidence level.

Fig. B.1. Schematic diagrams illustrate variable-density approach with three different loess cover models. (a) Model 1: instantaneous loess deposition after terrace abandonment and post-deposition constant denudation； (b) Model 2: continuous loess deposition at a constant accumulation rate after terrace abandonment; (c) Model 3: experience a constant denudation of terrace before very recent loess deposition event.

Supplementary Figures

Fig. S.1. Model self-check ~~by~~ using theoretical concentrations undergoing an exposure age of 20 ka or 800 ka, denudation rate of 10 mm/ka, and inheritance of 100,000 at/g. (a) ~~The~~ Iinverted solutions calculated from ~~the~~ three-dimensional-graph visualization approach by using theoretical concentrations (presented in insert table with error of about 5%). (b) Five colored curves show that largely different solutions can very well fit the same curve (~~Black~~black) using inversion approach. Inset table shows three free parameter values used for simulation. (c) and (d) 3D-graphs show the possible solutions within 1σ confidence. (e) and (f) Age-denudation rate solution spaces. Orange and blue curves show fitting solutions that match χ^2 values within limits of $[\chi^2_{\min}; \chi^2_{\min}+1]$ and best group with smallest χ^2 values ($\chi^2_{\min}\times 1.01$), respectively.

Fig. S.2. Results of Wumingshan regolith. (a-c) Denudation rate, exposure age and inheritance versus χ^2 values diagrams; (g) Cosmogenic nuclide concentration as a function of depth.

Fig. S.3. Cosmogenic ^{26}Al depth profile data, field photographs and integrated bulk density of Wumingshan regolith (a), Xianshuihe (b, c, and d) and Zagunao ~~rivers~~ (e and f) rivers. Orange and blue curves show fitting solutions that match χ^2 values within limits of $[\chi^2_{\min}; \chi^2_{\min}+1]$ and best group with smallest χ^2 values ($\chi^2_{\min}\times 1.01$), respectively. Red curves show variation of nuclide concentration in

loess under the assumption of a constant inheritance. Inset text gives exposure age, denudation rate, and inheritance. Solid and dashed green lines, respectively, show integrated bulk density and bulk density. Purple curve shows forward model solution (e.g., Perrineau et al., 2011) with two-stages model.

Fig. S.4. Results of Wumingshan regolith ~~by~~ using ~~the~~ method of Hidy et al. (2010).

Table captions

Table 1. Sampling sites, scaled surface cosmogenic ^{10}Be and ^{27}Al production rates and modeled exposure ages.

Table 2. ^{10}Be and ^{26}Al cosmogenic isotope data.

Supplementary table captions

Supplementary table 1. Statistical analysis for all possible solutions in ~~the~~ shaded area of ~~the~~ depth profile. Depth profiles of Ackerer et al. (2016) and Wumingshan (this study).

Supplementary table 2. Statistical analysis for all possible solutions in ~~the~~ orange shaded area of ~~the~~ ^{10}Be depth profile.

Supplementary table 3. Summary of published ~~of~~ basin-wide denudation rates data.

Supplementary table 4. Summary of published exposure/burial ages data.

Supplementary table 5. Summary of published ~~of~~ fluvial incision rates data.

Research Highlights

- **Late Quaternary landscape evolution of eastern Tibetan Plateau**
- **In-situ cosmogenic ^{10}Be and ^{26}Al depth profiles dating of granitic regolith and fluvial sediments**
- **Local landscape denudation and fluvial incision rates**
- **Time scales of tectonic and climate interactions**
- **A new three-dimensional-graph visualization for cosmogenic nuclides depth profile interpretation**

New constraints on the late Quaternary landscape evolution of the eastern Tibetan Plateau from ^{10}Be and ^{26}Al in-situ cosmogenic nuclides

Ye Yang[a,b,c], Cong-Qiang Liu[a,b*], Jérôme Van der Woerd[d*], Sheng Xu[a*], Li-Feng Cui[b], Zhi-Qi Zhao[e,b], Qi-Lian Wang[b], Guo-Dong Jia[a], François Chabaux[c*]

[a] Institute of Surface-Earth System Science, Tianjin University, Tianjin 300072, China

[b] State Key Laboratory of Environmental Geochemistry, Institute of Geochemistry, Chinese Academy of Sciences, Guiyang 550081, China

[c] Laboratoire d'Hydrologie et de Géochimie de Strasbourg (LHyGeS), CNRS UMR 7517, University of Strasbourg, 1 rue Blessig, 67084 Strasbourg cedex, France

[d] Institut de Physique du Globe de Strasbourg (IPGS), CNRS UMR 7516, University of Strasbourg, 5 rue René Descartes, 67084 Strasbourg cedex, France

[e] School of Earth Sciences and Recourses, Chang'an University, Xi'an 710054, China

[*] Corresponding authors.

E-mail addresses: liucongqiang@vip.skleg.cn (C.Q. Liu), jerome.vanderwoerd@unistra.fr (J. Van der Woerd), sheng.xu@tju.edu.cn (S. Xu), fchabaux@unistra.fr (F. Chabaux).

Abstract

Based on Terrestrial Cosmogenic Nuclide (TCN) constraints from depth profiles of one granitic regolith from Wumingshan and five fluvial terraces from Xianshuihe and Zagunao rivers, we discuss the timing of the last deglaciation, the landscape-scale denudation and fluvial incision rates across the eastern Tibetan Plateau, in relation to previous work. We present a three-dimensional-graph visualization approach and corresponding constraints to better assess the feasibility and applicability of cosmogenic nuclides depth-profile dating. The exposure age (older than 19.4 ka) of the Wumingshan regolith corresponds to the retreat of the palaeo-Daocheng ice cap, which covered the Yidun terrane during the Last Glacial Maximum (LGM). Most basin-wide denudation rate data in the eastern Tibetan Plateau are lower than 130 mm/ka (47 %, n=90), which is consistent with the Wumingshan regolith denudation rate (lower than 52.8 mm/ka), and thus indicate that the landscape-scale denudation has been stabilized after the last deglaciation. Considering the reduction of integrated bulk density due to the accumulation of lower-density loess, we estimate mean exposure ages of Xianshuihe and Zagunao river terraces of 4.0 ± 0.7 ka, 5.9 ± 0.3 ka, 13.4 ± 2.0 ka, and 16.6 ± 1.4 ka. The observed increase in incision rate from 0.39 mm/yr over long timescale (~600 ka) to 5.88 mm/yr over the last 15 ka at the Xianshuihe river site is probably due to the transition from glacial to interglacial climatic

conditions. The fewer abandoned terraces along the Zagunao river after the Heinrich event 1 (H1) indicates that the climate change during the latest glacial-interglacial transition impacted less the landscape evolution in a relatively lower elevation area. Comparison with previously reported fluvial incision rates elsewhere across the eastern margin of the Tibetan Plateau indicates that incision rates are mainly influenced by abrupt climate change or intensified summer monsoon since the early Holocene, but probably controlled by regional tectonic uplift or fluvial headward retreat as the timescale increases. Overall, we propose a synthetic pattern of landscape evolution mainly dominated by long-term tectonic uplift together with fluvial headward erosion, episodically influenced by climatic change throughout the late Quaternary.

Key words: Late Quaternary; Cosmogenic nuclides; Regolith; Denudation rate; Fluvial incision; Climate change; Eastern Tibetan Plateau

1. Introduction

Topography is a result of the interaction of tectonic uplift and fluvial incision modulated by climate on geological time scales (Molnar et al., 1994; Kirby et al., 2000; Hancock and Anderson, 2002; Clark et al., 2005; Liu-Zeng et al., 2008; Pan et al., 2009; Molnar et al., 2010; Ouimet et al.,

66 2010; Perrineau et al., 2011; Finnegan et al., 2014). The recent evolution
67 of the gentle gradient of the topography of the southeastern Tibetan
68 Plateau has been explained by two controversial models. On one hand,
69 topography is considered as the result of external processes involving a
70 wave of regressive development of rivers from the margin towards the
71 interior of an-already-high continental plateau, initiated by the onset of
72 the monsoon in the Miocene and modulated by climate (e.g., Métivier et
73 al., 1998; Tapponnier et al., 2001; Liu-Zeng et al., 2008; Roger et al.,
74 2010). On the other hand, it is interpreted as resulting from the recent
75 eastward spread of ductile lower crust from the plateau center towards its
76 rim (e.g., Burchfiel et al., 1995; Royden et al., 1997; Clark and Royden,
77 2000; Clark et al., 2005; Wang et al., 2012). Several approaches have
78 been used to independently constrain the rates of tectonic uplift, erosion
79 and the role of climate. Regional exhumation rates determined from
80 thermochronology or cosmogenic isotopes are classically used to discuss
81 the variations in space and time of regional uplift (Burbank et al., 1996;
82 Kirby et al., 2002; Godard et al., 2010; Ouimet et al., 2010; Ansberque et
83 al., 2015; Liu-Zeng et al., 2018; Tian et al., 2018). Fluvial terrace dating
84 is commonly used to determine rates of river incision (Kirby et al., 2000;
85 Liu et al., 2006; Chen et al., 2008b; Kong et al., 2009; Godard et al., 2010;
86 Zhao et al., 2013; He et al., 2015; Liu et al., 2015; Zhang et al., 2018).
87 The major issue with these approaches is how to disentangle regional

88 tectonic uplift, climate change, and river dynamics from both exhumation
89 and incision rates.
90 The objective of this study is to discuss our ability to determine tectonic
91 exhumation rates from river incision rates derived from well dated inset
92 terraces of two rivers in different tectonic setting (left-lateral strike-slip
93 Xianshuihe Fault system and Longmenshan thrust belt) using in situ
94 cosmogenic isotopes and by comparing these data with regionally
95 published data. The analysis of one granite regolith provides a perspective
96 to the coupling relationship between a surface erosive event caused by the
97 glacial advance and retreat, and the possible source of fluvial sediments.
98 This study also validates the methodology and emphasizes the need for
99 short- (10s ka) and long-term (several 100s ka) chronologies to be able to
100 constrain the long-term exhumation signal from the short-term climatic
101 response of river systems.
102
103 Fig. 1 about here.
104
105 **2. Geological setting and sample descriptions**
106 2.1. Study area
107 The eastern margin of the Tibetan Plateau is characterized by a low-relief,
108 upland erosion surface (Burchfiel et al., 1995; Royden et al., 1997; Clark
109 and Royden, 2000; Clark et al., 2004, 2005, 2006; Liu-Zeng et al., 2008)

that is drained by the Jinsha, Lancang (Mekong), Nu (Salween), and Yellow rivers (Fig. 1a). The geological structure of the study area is characterized by two main tectonic units: 1) the Songpan Ganzi fold belt including Triassic flysch intruded by a series of Jurassic granitic plutons, deformed Paleozoic rocks, crystalline Precambrian basement, low grade metamorphic Mesozoic sedimentary rocks, and limited Cenozoic sediments (e.g., Yin and Harrison, 2000; Roger et al., 2008); 2) the Longmenshan range made of exhumed crystalline rocks of the Yangtze craton and Paleozoic passive margin sediments (e.g., Burchfiel et al., 1995). Climatically, the study region has significant spatial and temporal variations in precipitation, which are dominated by the east Asian monsoon, the Indian monsoon, and the Westerlies (Fig. 1) (e.g., Maussion et al., 2014). Mean annual precipitation decreases from the margin (~2000 mm/yr) towards the plateau (lower than ~500 mm/yr) (Bookhagen, 2018, see Fig. 1b).

2.1.1. Wumingshan regolith

The sampling site (~4000 m above sea level, Table 1) is located in southern Yidun terrane (or Shaluli mountain), surrounded by the Qiangtang Terrane to west, the Songpan-Ganzi Fold Belt to northeast and the Yangtze Craton to southeast. It is bordered by the Jinshajiang Suture Zone (JSZ) in the west and Ganzi-Litang Suture Zone (GLSZ) in the east

(Fig. 1a). Wumingshan regolith is a typical granitic weathering product for studying the local landscape evolution in this area. The sampling location avoids the cover of loess and the presence of colluvial deposition to ensure that the granitic regolith is derived from the underlying bedrock and formed as a vertical weathering profile. The targeted bedrock is a Late Triassic granitic pluton with a zircon U-Pb age of 225 ± 2 Ma (Wu et al., 2017). The slope gradient of the hill is about 25°. Mean annual precipitation and temperature are, respectively, 654.3 mm/yr and 4.8 °C for the period of 1981-2010 (data from National Meteorological Information Center, China; http://data.cma.cn/en). Previous works suggest that the palaeo-Daocheng Ice Cap with an extension of about 4000 km^2 covered the Yidun terrane during the Last Glacial Maximum (LGM) (Xu and Zhou, 2009; Fu et al., 2013; Zhang et al., 2015).

2.1.2. Xianshuihe and Zagunao fluvial terraces

The sampling sites of the fluvial terraces along the Xianshuihe river (~3150 m above sea level in our study area, Table 1), a tributary of the Yalong River (Fig. 1a), are located southeast of Luhuo County (Fig. 2b). The recent tectonic activity in this high continental plateau area is mainly controlled by the left-lateral strike-slip Xianshuihe Fault system (Fig. 1a) that triggered more than 20 earthquakes of magnitude higher than 6.5 since A.D. 1700, including the 2010 M_w 6.9 Yushu earthquake (Chevalier

et al., 2017, and references therein). Mean annual precipitation and temperature are, respectively, 694.0 mm/yr and 6.7 °C for the period of 1981-2010 (data from National Meteorological Information Center, China; http://data.cma.cn/en). The arcuate Xianshuihe segmented fault system mainly consists of the Yushu-Ganzi Faults (YGF) to the northwest, the Xianshuihe Fault (XSHF) in the middle, and the Xiaojiang Fault (XJF) to the southeast (Fig. 1a) (e.g., Wang and Burchfiel, 2000).

The sampling sites along the Zagunao river (~1800 m above sea level in our study area, Table 1), a tributary of the Minjiang river (Fig. 1a), are located in Li County (Fig. 2c), a few kilometers upstream the main faults of the Longmenshan thrust belt (LMSTB) at the eastern margin of the Tibetan Plateau. The active LMSTB and Minjiang Fault (MJF), along which the devastating 2008 M_w 7.9 Wenchuan and 2013 M_w 7.0 Lushan earthquakes occurred, play a main role in the evolution of topographic and structural features at the eastern margin of the Tibetan Plateau. Mean annual precipitation and temperature are, respectively, 619.2 mm/yr and 11.4 °C for the period of 1981-2010 (data from National Meteorological Information Center, China; http://data.cma.cn/en).

In these two study areas, the abandoned fluvial sediments are covered with over than 50 cm-thick loess at all the sampling sites. The widely distributed loess is proposed to originate from the arid interior of the Tibetan Plateau during the late Quaternary (Qiao et al., 2014; Hu et al.,

176 2015).

177

178 Fig. 2 about here.

179

180 2.2. Sampling strategy

181 Thirty ~4 kg samples, including granitic regolith, amalgamated sands and
182 sandy to pebbly gravels (Fig. 3), were collected (Fig. 1a). The artificial
183 road cuts, modern river erosion profiles and natural gullies (Fig. 3)
184 provided the ideal sampling sites. Samples were analyzed for in situ
185 cosmogenic ^{10}Be and ^{26}Al in quartz. A digital elevation model (DEM)
186 with 30 m resolution was constructed to determine the topographic
187 environment (data from Geospatial Data Cloud site, Computer Network
188 Information Center, Chinese Academy of Sciences;
189 http://www.gscloud.cn). Conservative uncertainties of 10% on elevations
190 were considered to account for field measurement error and
191 morphological roughness.

192 The Wumingshan regolith profile was sampled to constrain the recent
193 Quaternary weathering process and denudation rate of the granitic
194 bedrock. To avoid the disturbing effect of shallow soil in the 2 m-deep
195 profile, four deep samples were selected to determine the cosmogenic
196 nuclides concentration in quartz (Fig. 3a and Table 2).

197 Considering the complex deposition history of loess, three depth-profiles

198 and three deep burial samples were collected from the younger terraces in
199 the Xianshuihe fluvial terraces (Figs. 3c-e). Coarse-grained quartz (> 2
200 mm, XSH-5-1) and fine-grained quartz (< 2 mm, XSH-5-2) were
201 analyzed on duplicate samples to test the variability of inheritance in the
202 different quartz source regions (Table 2). Two depth profiles and four
203 deep burial samples (Table 2) were collected from the younger terraces in
204 the Zagunao fluvial terraces. These abandoned sediments were collected
205 to constrain the exposure age of the fluvial terraces and the incision rate
206 of the river. The loess mantle, the fine fraction (silt and soil), and the
207 coarse material (sand, pebbles, cobbles, and boulders) were assumed to
208 have densities of 1.4 ± 0.1, 1.6 ± 0.1, and 2.6 ± 0.1 g/cm^3, respectively.
209 The bulk density was calculated by estimating the proportion of fine and
210 coarse fractions using field photos and macroscopic description of the
211 horizons (Hancock et al., 1999; Perrineau et al., 2011; Guilbaud et al.,
212 2017).
213
214 **3. Analytical methods**
215 3.1. TCN sample preparation and analyses
216 Chemical preparation was performed at the cosmogenic nuclide
217 laboratory of Institut de Physique du Globe de Strasbourg (UMR 7516,
218 CNRS and University of Strasbourg, France) following standard methods
219 (e.g., Perrineau et al., 2011; Guilbaud et al., 2017). Samples were crushed

and sieved to fractions of 250-500 µm followed by magnetic and gravimetric separation. Oxides and carbonate matter were removed by HNO_3 leaching. Multiple overnight leaches in hot 1% HF/HNO_3 solutions were performed to remove the meteoric cosmogenic nuclides and to obtain purified quartz. Samples were dissolved in 5:1 HF/HNO_3 and spiked with ~250 mg of commercially available Scharlau ICP 1000 mg/l ^{9}Be standard (Table 2). Scharlau ICP 1000 mg/l ^{27}Al standard was added for samples with less than 2 mg of native ^{27}Al determined with ICP-AES at LHYGES (Table 2). Subsequently, the separation and purification by ion exchange chromatography, hydroxylation and oxidation were performed. BeO and Al_2O_3 were mixed with niobium and silver powder, respectively to make targets. The $^{10}Be/^{9}Be$ and $^{26}Al/^{27}Al$ ratios were measured on the ASTER AMS French national facility (CEREGE, Aix-en-Provence, France) (Table 2). $^{10}Be/^{9}Be$ and $^{26}Al/^{27}Al$ ratios were calibrated versus the ASTER in-house standard STD-11 ($^{10}Be/^{9}Be$ = $(1.191 \pm 0.013) \times 10^{-11}$) and SM-A1-11 ($7.401 \pm 0.064 \times 10^{-12}$), respectively (Arnold et al., 2010; Braucher et al., 2015). Both $^{10}Be/^{9}Be$ and $^{26}Al/^{27}Al$ ratios of processed blanks are approximately 3×10^{-15}.

3.2. Model setup

3.2.1. Chi-square modeling

Using the classical approximation that subsurface production rate can be

represented by exponential functions different for neutrons, slow muons and fast muons (Granger and Smith, 2000; Schaller et al., 2002; Braucher et al., 2003, 2011, 2013; Hidy et al., 2010; Balco, 2017) and by making the presuppositions of steady erosion, average inheritance, and constant production rates, the expression of a measured nuclide concentration as a function of denudation rate, exposure age, and inheritance can be written in the following explicit form (Braucher et al., 2003, 2011; Siame et al., 2004; Rodés et al., 2011; Cui et al., 2014, 2016; 2014; Ackerer et al., 2016; Charreau et al., 2017; Schaller et al., 2018; Sordi et al., 2018):

$$C(x,\varepsilon,t) = c_0 e^{-\lambda t} + \sum_{i=spal,slow,fast} \frac{P_i}{\lambda + \frac{\rho_x}{\Lambda_i}\varepsilon} e^{-\frac{\rho_x}{\Lambda_i}x} [1 - e^{-(\lambda + \frac{\rho_x}{\Lambda_i}\varepsilon)t}] \qquad (1)$$

where $C(x,\varepsilon,t)$ is the present nuclide concentration, c_0 is the average cosmogenic inheritance (in at/g), ρ_x is the integrated bulk density at depth x , t is the exposure age, ε is the accumulation rate (negative) or denudation rate (positive), λ is the decay constant 5.00×10^{-7} yr^{-1} for ^{10}Be (Chmeleff et al., 2010; Korschinek et al., 2010) and 9.83×10^{-7} yr^{-1} for ^{26}Al (Nishiizumi, 2004), P_{spal}, P_{slow}, P_{fast} and Λ_{spal}, Λ_{slow}, Λ_{fast} are the surface production rates and attenuation lengths of neutrons, slow muons and fast muons, respectively. An exponential model for muon production rates provides an acceptable accuracy for shallow depth profiles and relatively slow denudation rates as found at our study sites. Therefore, the simplified three exponential functions approximation for subsurface

263 production rates was used in all calculations and modeling in this study.
264 The production rates relative to sea level and high latitude (SLHL) as a
265 function of geographic latitude and air pressure (Lal, 1991; Stone, 2000)
266 are listed in Table 1. A global mean SLHL spallogenic production rate of
267 4.13 at/($g_{(qtz)}$ yr) for ^{10}Be (Martin et al., 2017) and a ^{26}Al/^{10}Be spallogenic
268 production ratio of 6.61 (Braucher et al., 2011) are used to scale the local
269 production rates. We also include a correction factor for shielding by the
270 surrounding topography using the online calculator of Balco et al. (2008)
271 and regard the shielding by snow or vegetation as negligible. The
272 spallogenic production rates uncertainty of ^{10}Be and ^{26}Al are assumed to
273 be 7.2% and 10% (Phillips et al., 2016), respectively, after Borchers et al.
274 (2016) by integrating the root mean square error of different previous
275 study sites. Muons production rates (see Table 1) are scaled with
276 atmospheric pressure and we ignore the latitudinal effect (Braucher et al.,
277 2011). Depth scaling of production rates are based on attenuation lengths
278 Λ_{spal}, Λ_{slow}, and Λ_{fast} of ~165, ~1500, and ~4320 g/cm^2 respectively
279 (Braucher et al., 2011; Marrero et al., 2016). The best fit was performed
280 by minimizing the chi-square value (Rodés et al., 2011, and references
281 therein) as follows:

282 $$\chi^2 = \sum_{i=1}^{n} \left(\frac{C_i - C(x,\varepsilon,t)}{\sigma_{C_i}}\right)^2$$

283 (2)

284 Where C_i are the measured concentration at x_i depth, and $C(x,\varepsilon,t)$ is

285 the concentration predicted from Equation (1). Only the uncertainty of the
286 measured concentration (σ_{C_i}) is considered because it would be
287 impossible to simultaneously fit all parameters using only one measured
288 concentration per sample (Borchers et al., 2016). Recently, in order to
289 avoid the problem of "mixed estimator", the $\chi^2_{1\sigma}$ was replaced by the
290 value of $\chi^2_{\min}+1$ (Guralnik et al., 2011; Saint-Carlier et al., 2016;
291 Charreau et al., 2017; Delmas et al., 2018) to obtain the fitting values
292 since the range of solutions is considered as a proxy for 1σ confidence
293 level (Bevington and Robinson, 2003). To estimate the goodness of the
294 fitting, the *p*-value of the chi-square best fit value has been used in this
295 study, and *p*-values larger than 5% are considered as a valid prediction of
296 the fitting model (Aster et al., 2013; Borchers et al., 2016; Phillips et al.,
297 2016).
298
299 Fig. 3 about here.
300
301 3.2.2. A three-dimensional-graph visualization approach
302 Based on previous approaches (Braucher et al., 2009; Hidy et al., 2010;
303 Rodés et al., 2011; Marrero et al., 2016), a visual, multi-interpreted, and
304 robust depth-profile simulation approach was designed to model the three
305 parameters (denudation rate, exposure age, and inheritance) for
306 cosmogenic nuclides depth profile (see detailed description in Appendix

307 A). In practice, the chi-square value can be minimized by a series of
308 different denudation rate, exposure age, and inheritance values even when
309 the *p*-value is close to 1 (see detail in Fig. S.1). The inability to obtain a
310 unique solution is inevitable for the square sum function. However, to
311 circumvent this difficulty, the bounds of denudation rate, exposure age, or
312 inheritance are constrained by various reliable assumptions, such as the
313 effective total denudation evidence (Hidy et al., 2010; Marrero et al.,
314 2016), a zero denudation (Guralnik et al., 2011; Saint-Carlier et al., 2016),
315 or a considered inheritance (Cui et al., 2016; Hidy et al., 2018). All the
316 assumptions constrain the final fit, so we should be cautious when
317 choosing the various reliable assumptions. Overall, the resulting ranges
318 are sufficiently reliable to avoid over-constraining the inversion while
319 discouraging the complex modeling to calculate the unreliable ranges that
320 are considered to be less likely. Therefore, the 3D-graph visualization
321 approach is used in this study to estimate the impact of the different
322 assumptions and display the interactions among denudation rate,
323 exposure age, and inheritance in one graph. This approach also
324 emphasizes that any paired solutions of age and denudation rate are based
325 on a given inheritance.
326
327 3.2.3. Variable-density approach
328 A significant loess cover is found covering the depth profiles, indicating

329 that the assumption of a constant density based on the present-day
330 outcrop, which includes the loess cover, is invalid. To account for the
331 potential influence of loess after the abandonment of the fluvial terraces,
332 we consider that the integrated bulk density composed of the lower-
333 density covering loess and the higher-density underlying sediments
334 increases or decreases constantly with time due to the denudation or
335 accumulation of the loess in the study area. Equation (1) then becomes
336 (see details in Appendix B):

337 $$C(x,\varepsilon,t) = c_0 e^{-\lambda t} + \sum_{i=spal,slow,fast} \frac{P_i}{\lambda + \frac{\rho_{loess}}{\Lambda_i}\varepsilon} e^{-\left(\frac{\rho_{xsed} x_{sed}}{\Lambda_i} + \frac{\rho_{loess} x_{loess}}{\Lambda_i}\right)} \left[1 - e^{-\left(\lambda + \frac{\rho_{loess}}{\Lambda_i}\varepsilon\right)t}\right]$$

338 (3)

339 where x_{loess} is the current depth of the loess, ρ_{xsed} is the integrated bulk
340 density of sediments at depth x_{sed}, and ρ_{loess} is the density of the loess
341 (Fig. B.1, see details in Appendix B).

342 To account for the potential effects of loess after abandonment of the
343 fluvial terraces and without knowledge of the timing and rate of loess
344 deposition, three different simplified deposition models have been used to
345 model the exposure ages (e.g., Charreau et al., 2017). Model 1:
346 instantaneous loess deposition after terrace abandonment and post-
347 deposition constant denudation (maximum age); Model 2: continuous
348 loess deposition at a constant accumulation rate after terrace
349 abandonment ("mean" age); Model 3: experience a constant terrace

denudation before a very recent loess deposition event (minimum age; ignoring the attenuation in the loess) (Fig. B.1, see details in Appendix B).

Fig. 4 about here.

4. Results

The concentrations of ^{26}Al and ^{10}Be show a linear relationship (Fig. 4a). The average ratio (~7.45) of ^{26}Al/^{10}Be is higher than the spallation production ratio of 6.61 (Braucher et al., 2011), which can be explained by the variation in ^{26}Al/^{10}Be ratio with increasing bedrock depth (Akçar et al., 2017). The ^{26}Al/^{10}Be ratios for all samples, excluding two anomalous results (XSH-5-1-2 and XSH-5-1-3), plot well in the steady state erosion island (Lal, 1991), which indicates that the pre-deposition burial history of the samples is negligible (Fig. 4b).

The results of the four cosmogenic nuclide ^{10}Be and ^{26}Al depth-profile saprolite samples (WMS1-11, WMS1-17, WMS1-22, and WMS1-26) are listed in Table 2 and supplementary Table 1. The ^{10}Be inversion of the depth profile, assuming the net erosion was no more than 100 cm ($\varepsilon \times t < 100$), constrains the age of the regolith to $27.0^{+9.6}_{-7.6}$ ka, the denudation rate to $18.4^{+14.4}_{-18.4}$ mm/ka, and the inheritance to $26.6^{+2.9}_{-3.1} \times 10^4$ at/g (Fig. 5a, supplementary Table 1 and Fig. S.2). The constant inheritance is interpreted as a result of one erosive event caused by the impact of the

372 last glacial period (see detail in section 5.2). Ignoring the constraint of net
373 erosion, a minimum age of 19.4 ka and a maximum denudation rate of
374 52.8 mm/ka are obtained. The ^{26}Al inversion shows consistent results (see
375 details in supplementary Table 1 and Fig. S.3). Similar ranges of age
376 (21.6 - 38.6 ka), denudation rate (0 - 29.6 mm/ka) and ^{10}Be inheritance
377 (23.3 - 28.4 $\times 10^4$ at/g) (see details in supplementary Table 1) are
378 calculated when combining ^{26}Al and ^{10}Be cosmogenic nuclides (Rodés et
379 al., 2011, 2014) by assuming negligible pre-deposition burial history, or
380 with the simulator of Hidy et al. (2010; version 1.2) (age: 19.3 – 36.5 ka;
381 denudation rate: 0 – 33.1 mm/ka; inheritance: 22.9 - 29.5 $\times 10^4$ at/g) (see
382 details in Fig. S.4). Such a consistency between the three calculation
383 approaches supports the reliability of the results derived from the depth
384 profiles and the assumption of negligible burial history.
385 The whole cosmogenic nuclide analyses of fluvial terraces are presented
386 in Table 2 and supplementary Table 2. According to the depth profiles,
387 we calculated the surface exposure age, accumulation/denudation rate,
388 and inheritance of the fluvial sediments using the three-dimensional chi-
389 square inversion approach. Three different models (see details in
390 Appendix B) were used for each depth profile to estimate the impact
391 caused by different loess deposition scenario. Based on the field
392 observations, a loess net erosion of less than 20 cm was assumed in
393 Model 1 to constrain the wide range of free parameters. There are no

obvious paleosoil between the loess and the fluvial sediments, conservatively, no more than 10 cm net erosion was assumed in Model 3 to constrain the 3D visualization inversion approach. The Model 2 inversion approach, assuming continuous deposition ($\varepsilon \times t = x_{loess}$) and considering the variation of the integrated bulk density, constrains the mean ^{10}Be exposure age to 4.0 ± 0.7 ka, 5.9 ± 1.3 ka, 13.4 ± 2.0 ka, and 16.6 ± 1.4 ka for the sites XSH-3 (T2), XSH-2 (T3), XSH-5 (T4), and ZGN-7 (T1), respectively (Figs. 4b-d, 4f and supplementary Table 2). The mean ^{26}Al exposure ages show consistent results (see details in Fig. S.3). Moreover, two end-member ages of the minimum exposure age (Model 1: instantaneous deposition of loess after terrace abandonment) and the maximum exposure age (Model 3: constant denudation before very recent loess deposition) are presented in Fig. 5 and supplementary Table 2.

Due to the scattering of the XSH-2 (T3) data and the small number of samples, the analytical quality of the XSH-2 (T3) age (5.9 ± 1.3 ka) is slightly less robust. However, this age is consistent with the position of T3 between T2 and T4 with ages of 4.0 ± 0.7 ka and 13.4 ± 2.0 ka, respectively (Fig. 5b). Owing to the tectonic activity and landslides in the Zagunao area (Figs. 2g and 2h), the data of the deepest (8 m) depth profile (ZGN-2) cannot be fitted due to excessive scatter and insufficient number of samples. We used forward modeling (e.g., Perrineau et al.,

2011), assuming no denudation and a two-stages deposition model to constrain the two periods of exposure of ~2.0 ka and ~3.3 ka (Fig. 5e). Coarse-grained quartz (2-10 mm, XSH-5-1) and fine-grained quartz (< 2 mm, XSH-5-2) were analyzed on 3 samples to test whether the various quartz grains have different inheritance values. The ^{10}Be results show very similar concentrations for the two shallow samples but a larger concentration for the deepest coarse-grained quartz. The difference observed in the deepest sample may be explained by a difference in the provenance of the coarse-grained quartz and fine-grained quartz. The coarse-grained quartz could be detached from resistant quartz veins, which have a longer residence time on the hillslopes (e.g., Codilean et al., 2014), recycled from the older sediments, thus with a longer exposure than the fresh rocks (e.g., Wittmann et al., 2011), or derived from the abrasion of cobbles exhumed at high elevations (e.g., Carretier et al., 2015). The result highlights the importance of grain size in the interpretation of cosmogenic nuclide data.

Fig. 6 about here.

5. Discussion

5.1. Feasibility and applicability of the three-dimensional-graph visualization approach for cosmogenic nuclides depth profile

438 The values derived from the three-dimensional-graph visualization
439 approach provide a reliable estimate of exposure age, denudation rate,
440 and inheritance. However, the chi-square value (Equation (3)) can be
441 minimized for different sets of denudation rates, exposure ages, and
442 inheritance values (e.g., Hidy et al., 2010; Borchers et al., 2016; Saint-
443 Carlier et al., 2016). Even when a local minimum chi-square value is
444 obtained, including the perfect fit of the data (p-value = 1), one can still
445 get a series of possible solutions for exposure ages and denudation rates
446 (Figs. S.1, S.2a and 2b). The self-check of the three-dimensional
447 inversion approach indicates that the assumptions of negligible
448 inheritance or subjective denudation rate should not be made to gain a
449 seemingly plausible exposure age, e.g., exposure dating of surface
450 samples (surface rock, surface sediments and moraine) and excessive
451 constraints should not be imposed to the simulator. Therefore,
452 independent constraints derived from the field investigations are essential
453 to obtain a reliable solution (see details in section 4).
454
455 5.2. The timing of the last deglaciation revealed by receding glacier in the
456 eastern Tibetan Plateau.
457 The glacial history of the eastern Tibetan Plateau has been investigated to
458 constrain the timing, extent and climatic conditions of paleoglaciations.
459 The evolution of regional paleoglaciations, which are a proxy for the

460 record of regional climate change (Clark et al., 2009), can be
461 reconstructed using precise dating methods such as ^{10}Be, radiocarbon
462 (^{14}C), optically stimulated luminescence (OSL), and electron spin
463 resonance (ESR). Although a series of glacial deposits is dated in the
464 study area (Fig. 6 and supplementary Table 3), the onset of the last
465 deglaciation still remains controversial (Schäfer et al., 2002; Owen et al.,
466 2003, 2005; Zhou et al., 2005; Kong et al., 2009; Xu and Zhou, 2009;
467 Heyman et al., 2011; Fu et al., 2013; Zhang et al., 2015). These previous
468 data (Fig. 6a) from Ganzi (Chevalier et al., 2017), Litang (Schäfer et al.,
469 2002; Graf et al., 2008; Fu et al., 2013), Daocheng (Xu et al., 2004; Wang
470 et al., 2006; Graf et al., 2008; Xu and Zhou, 2009; Fu et al., 2013; Zhang
471 et al., 2015), Queer mountain (Xu et al., 2010; Zhang et al., 2012; Ou et
472 al., 2013, 2014), and Kangding (Tschudi et al., 2003; Strasky et al., 2009;
473 Yan and Lin, 2017; Bai et al., 2018) provide evidence of two conspicuous
474 glacial advances: one during the Heinrich event 1 (H1) (Heinrich, 1988)
475 at about 16,800 yr (Hemming, 2004, and references therein) and the other
476 one during the Younger Dryas (YD) from 12,823 ± 60 yr to 11,473 ± 100
477 yr (Wang et al., 2001). In our study, the exposure age of ZGN-7 (~16.6 ka)
478 indicates that sediments were abandoned in the valleys and basins after
479 the LGM (Fig. 7b). Then, the age of ~13.4 ka (XSH-4) corresponds to the
480 period between the H1 and YD glacial advances (Figs. 7a and 7b).
481 Subsequently, the exposure age of XSH-2 (~5.9 ka) and XSH-3 (~4.0 ka)

482 are consistent with the interval of monsoonal Himalayan-Tibetan stages
483 (MOHITS) (Murari et al., 2014) or mid-Holocene climate optimum (Fig.
484 7b). The spatial and temporal distributions of published exposure or
485 burial ages in the eastern Tibetan Plateau are presented in Fig. 6. We
486 obtain an exposure age for the granitic regolith located in the Yidun
487 terrane older than 19.4 ka (unconstrained) or $27.0^{+9.6}_{-7.6}$ ka (with a net
488 erosion less than 100 cm), which indicates that an erosive event occurred
489 in this area approximately 20 ka ago, coincident with global Late Glacial
490 Maximum (e.g., Clark et al., 2009), likely resulting from glacial or
491 periglacial processes. This age is consistent with the presence of the
492 palaeo-Daocheng ice cap during the LGM (Xu and Zhou, 2009; Fu et al.,
493 2013; Zhang et al., 2015). This age is also found as a peak in the age
494 distribution of Fig. 6c, indicating a regional event, and likely related to
495 the glacial to interglacial transition at the end of the LGM. The profile
496 shows inheritance within the regolith, which can be interpreted as
497 proposed in other geographical contexts (e.g., Ackerer et al., 2016) as an
498 evidence of a complex erosive history of the regolith marked by other
499 intense glacial erosive events, prior to the erosive event at 20 ka. In
500 addition, most basin-wide denudation rate data in the eastern Tibetan
501 Plateau are lower than 130 mm/ka (47 %, n=90) (Fig. 6b) and thus,
502 consistently with the regolith denudation rate (lower than 52.8 mm/ka),
503 indicate that the denudation of the landscape is demonstrably stable

following the last deglaciation.

Fig. 7 and 8 about here.

5.3. The framework for the late Quaternary fluvial incision in the eastern Tibetan Plateau

The observation of variable incision rates provides insight into the topographic and geomorphic evolution. Previous studies focused on the onset of incision and paid less attention to the variation of the incision rates after the incision began (Kirby et al., 2002; Clark et al., 2005; Godard et al., 2009; Pan et al., 2009; Ouimet et al., 2010; Perrineau et al., 2011). Fluvial incision rates, assumed to be in equilibrium with external forcings over a wide range of timescales especially in a tectonically rising landscape, were commonly interpreted as a proxy for the quantification of tectonic uplift rate and indicating the strength of climate change under the assumption of steady-state (Burbank et al., 1996; Maddy et al., 2000; Kong et al., 2009; Pan et al., 2009; Huang et al., 2014; Ruszkiczay-Rüdiger et al., 2016; Delmas et al., 2018). However, the significant effect of lag time (Fig. 8) between uplift and incision indicates that the river incision becomes periodically negligible in hyper-arid conditions or due to very low gravel flux (Whipple, 2004; Ouimet et al., 2010). In addition, the fluvial incision rate is exaggerated due to the fact that long episodic

526 incision hiatuses, including river bed aggradation and return to pre-
527 deposition (Fig. 8), are ignored (Gardner et al., 1987; Mills, 2000;
528 Schumer and Jerolmack, 2009; Lague, 2010; Finnegan et al., 2014; Zhang
529 et al., 2018). Fig. 8 shows a fluvial incision model to account for the
530 relationship among fluvial incision, tectonic uplift and climate change at
531 different timescales. Exaggerated fluvial incision rates at short timescale
532 are seemingly caused by ignoring the hysteresis effect (e.g., Whipple and
533 Tucker, 2002; Ouimet et al., 2010) and/or episodic hiatuses (e.g.,
534 Finnegan et al., 2014) (Fig. 8). The negative power-law dependence of
535 bedrock river incision rate on different timescales (e.g., Schumer and
536 Jerolmack, 2009) is used to interpret that the slopes (green and red dashed
537 line in Fig. 8) decrease with increasing timescale.
538 On the long timescale of several million years, previous studies using
539 multiple thermochronology methods suggest that the eastern margin of
540 the Tibetan Plateau, including Minjiang, Dadu, Yalong, and Jinsha rivers,
541 experienced high exhumation rates on the order of 0.2-1.0 mm/yr (e.g.,
542 Kirby et al., 2002; Clark et al., 2005; Godard et al., 2009; Ouimet et al.,
543 2010; Tian et al., 2018) with initiation ages of ca. 8-15 Ma. Liu et al.
544 (2006) and Zhao et al. (2013) propose that the Zagunao and Xianhuihe
545 rivers experience a relative stable average incision rate of ~0.39 mm/yr
546 over a long timescale (~600 ka) by using the ESR dating method (Fig. 7d).
547 Similar results of 0.5-0.8 mm/yr are obtained from river watershed-

548 averaged denudation rates along the Longmenshan range front by using
549 the river sediment load data (Liu-Zeng et al., 2011). The consistency
550 between these rates, representative of long-term processes seemingly
551 shows that the incision rate is a proxy for the tectonic uplift rate. But,
552 fluvial incision rates are not strictly equal to the tectonic uplift rates in all
553 circumstances (Gallen et al., 2015), especially at short timescale. An
554 increase incision rate from 1.32 ± 0.37 mm/yr (59.8 ± 16.9 ka) to 4.25 ±
555 0.76 mm/yr (10.6 ± 1.9 ka) is obtained in the Jinsha fluvial terraces by
556 using the OSL dating method (Chen et al., 2008b). ^{14}C, OSL, and ^{10}Be
557 data from terraces in the frontal region of the Longmenshan show that the
558 erosion rate is less than 0.5 ± 0.1 mm/yr (at the timescale of 150 ± 25 ka)
559 and increases to ~1 mm/yr (at the timescale of 20-40 ka) towards the west
560 (Fig. 6a) (Godard et al., 2010). He et al. (2015) also proposed an increase
561 of the incision rate at the timescale of ~60 ka in the lower reach of the
562 Yalong river (Fig. 6a). In our study, a fast incision rate of ~5.88 mm/yr
563 for the last ~10 ka along the Xianshuihe river contrasts with the long-term
564 incision rate of ~0.39 mm/yr. The compilation of previously reported
565 fluvial incision rates (see detail in supplementary Table 5) shows a peak
566 of fast incision rates at the short timescale of ~10 ka in the eastern
567 Tibetan Plateau (Fig. 7c). Our results show that the fluvial incision rate
568 varies by at least one order of magnitude depending on the time scale of
569 observation (Figs 6 and 7), implying decoupling between regional long-

570 term landscape erosion rates and fluvial incision (e.g., Zhang et al., 2018).
571 The slight increase of incision rate along the Zagunao river may be due to
572 its lower altitude, less frost shattering and denser vegetation. According
573 to the published data and our cosmogenic ^{10}Be and ^{26}Al results, we
574 propose that the fluvial incision rate is mainly influenced by the abrupt
575 climate change or the intensified summer monsoon in the eastern Tibetan
576 Plateau since the early Holocene (Chen et al., 2008a), and controlled by
577 tectonic uplift or progressive fluvial headward retreat for longer
578 timescales. These results emphasize the need of the integration of data at
579 several time scales to unravel the dynamic of river incision and the role of
580 the different processes operating at different time scales (e.g., Mills, 2000;
581 Whipple and Tucker, 2002; Finnegan et al., 2014; Zhang et al., 2018).
582
583 5.4. An integrated driving mechanisms of landscape evolution in the
584 eastern Tibetan Plateau.
585 The competition between fluvial incision processes and tectonic uplift
586 processes is generally considered for the topographic and geomorphic
587 evolution of mountain belts (e.g., Burbank et al., 1996; Maddy et al.,
588 2000; Pan et al., 2009; Ruszkiczay-Rüdiger et al., 2016). In addition, the
589 formation of fluvial terraces is mainly controlled by the synergistic
590 effects of fluvial incision, tectonic uplift and climate change (e.g., Bull,
591 1991; Hancock and Anderson, 2002). However, quantifying the

592 contributions of climate change and tectonic uplift from river incision
593 rates is not straightforward. The great changes of flood magnitude and
594 frequency caused by the climatic transitions are responsible for the
595 formation of fluvial terraces (e.g., Chen et al., 2008b; Huang et al., 2014;
596 He et al., 2015; Delmas et al., 2018; Zhang et al., 2018). During glacial
597 periods, enhanced frost shattering and degradation of vegetation both
598 caused an excess of sediment (on the slopes). Subsequently, these large
599 amounts of sediments are transported in basins or valleys when the
600 climate becomes warmer and wetter during interglacial, which is coupled
601 to the erosive event that occurred on the bedrock surface of Wumingshan
602 regolith (see detail in section 5.2). Because of reworking and/or recycling
603 of the sediment not all glacial-interglacial transitions remain in the terrace
604 record (purple shaded area in Fig. 8) (e.g., Cogez et al., 2018). Fluvial
605 terraces emplaced during previous glacial terminations, as the last seven
606 glacial terminations (Lisiecki and Raymo, 2005), are most probably
607 reworked or recycled by subsequent glacial-interglacial transitions (Fig.
608 8). On the long-term, crustal isostatic rebound caused by the unloading as
609 a result of deglaciation (e.g., Rohling et al., 2017) and surface
610 erosion/denudation processes (e.g., Burbank, 1992; Kirby et al., 2000)
611 cannot be ignored (Whipple, 2009; Molnar, 2012). The information of
612 fluvial incision has been recorded and its acceleration during the
613 Holocene is likely the consequence of several processes: (i) the long-term

614 tectonic uplift together with fluvial headward erosion; (ii) the short-term
615 dramatic climate change at glacial-interglacial transitions; and (iii) the
616 long-term isostatic rebound caused by the unloading as a result of
617 deglaciation and surface denudation processes.
618
619 **6. Conclusions**
620 An integrated analysis of last deglaciation, local denudation and fluvial
621 incision leads to the evaluation of landscape evolution, climate change
622 and tectonic uplift in the eastern Tibetan Plateau. In this study, we obtain
623 the exposure age older than 19.4 ka (or $27.0^{+9.6}_{-7.6}$ ka without constraints)
624 and the denudation rate lower than 52.8 mm/ka (or $18.4^{+14.4}_{-18.4}$ mm/kyr
625 without constraints) (Fig. 5) for the Wumingshan regolith (Yidun pluton)
626 at the eastern margin of the Tibetan Plateau. These results coincide with
627 the timing of the last deglaciation and reveal a stable landscape after the
628 glacial or periglacial erosive event in this area. Our fluvial incision rates
629 inferred from terrace ages, associated to previous river incision data show
630 that the present fluvial incision rate is mainly influenced by the abrupt
631 climate change or the intensified summer monsoon in the eastern Tibetan
632 Plateau since the early Holocene, and that long-term incision rates are
633 probably linked to tectonic uplift or fluvial headward retreat. The driving
634 mechanisms of accelerated fluvial incision rate during the late Quaternary
635 is interpreted as the synthetic pattern of landscape evolution mainly

636 dominated by long-term tectonic uplift, periodically influenced by the
637 climatic change and isostasy throughout the late Quaternary.
638
639 **Acknowledgements**
640 Constructive comments by Régis Braucher and one anonymous reviewer
641 significantly improved the paper. The authors express gratitude to J.W.
642 Zhang, X.L. Zhang, G.W. Song, R.C. Ye for their help for field
643 campaigns and sample preparation. We are grateful to René Boutin at
644 LHyGeS and ASTER Team (G. Aumaître, D. Bourlès, and K.
645 Keddadouche) at ASTER-CEREGE for ICP-AES and AMS
646 measurements, respectively. The first author warmly thanks J. Liu-Zeng,
647 D. Fink and J. Ackerer for enlightening discussions. This work was
648 financially supported by the National Natural Science Foundation of
649 China (Nos. 41661144042, 41673124 and 41603018), the Second Tibetan
650 Plateau Scientific Expedition and Research (2019QZKK0707), and by the
651 INSU-CNRS, France and the University of Strasbourg to F. Chabaux and
652 J. Van der Woerd for the Al and Be concentration analyses at LHyGeS
653 and IPGS, and for $^{10}Be/^{9}Be$ and $^{26}Al/^{27}Al$ ratios measurements on the
654 Aster AMS facility (GEREGE, Aix-en-Provence, France) supported by
655 INSU-CNRS and IRD.
656

657 **Appendix A. The three-dimensional-graph visualization approach.**

According to the inequality derived by different confidence level of $\chi^2 < \chi^2_{2\sigma}$, $\chi^2 < \chi^2_{1\sigma}$ or $\chi^2 < \chi^2_{\min} + 1$, one or more shaded area representing all the possible solutions were yielded in the three-dimensional space (Figs. A.1a and b). After a reliable constraint, the plot range of denudation rate, exposure age, and inheritance need to be adjusted so that the black points almost fill the three-dimensional space (Fig. A.1a, the inset box shows the plot range of Fig. A.1b). We use the method of Rodés et al. (2011) and Braucher et al. (2009) to generate a denudation-age-inheritance space. The greater the number of points (can be adjusted by the increments) in the shaded area, the higher the accuracy of the analysis. In addition, it is a time-consuming process to yield a better statistical analysis accuracy. Statistical analysis for all possible solutions in the orange shaded area (Fig. A.1b), which represents a confidence level of $\chi^2_{\min} + 1$, can yield the minimum, maximum, mean, mode, and median solutions of denudation rate, exposure age, and inheritance, respectively (supplementary Table 1). Figs. A.1c, d and e show the χ^2 plots for denudation rate, exposure age, and inheritance values, and the inset diagrams show the probability distribution functions (PDFs) and cumulative distribution functions (CDFs) for denudation rate, exposure age, and inheritance, respectively.

Appendix B. Constraint on the variable-density approach.

In order to model the complex geological process of the accumulated loess, we combine the method of Charreau et al. (2017) and the variable-density approach. The mean age and two end-member ages have been estimated from the modeling as follows:

Model 1: instantaneous deposition

If we consider that the loess was instantaneously deposited after terrace abandonment and subsequently experienced a constant denudation ($\varepsilon > 0$) (Fig. B.1a), the three free parameters (denudation rate, exposure age, and inheritance), described by Equation (3), are determined by the 3D visualization approach.

Model 2: continuous deposition

Continuous deposition at a constant accumulation rate ($\varepsilon < 0$) after terrace abandonment has been assumed to get the mean age (Fig. B.1b). In addition, the exposure age and accumulation rate are dependent on the total depth of loess ($x_{loess} = -\varepsilon \times t$). Then, Equation (3) becomes:

$$C(x,\varepsilon,t) = c_0 e^{-\lambda t} + \sum_{i=spal,slow,fast} \frac{P_i}{\lambda - \frac{\rho_{loess} x_{loess}}{\Lambda_i t}} e^{-\left(\frac{\rho_{xsed} x_{sed}}{\Lambda_i} + \frac{\rho_{loess} x_{loess}}{\Lambda_i}\right)} \left[1 - e^{-\left(\lambda t - \frac{\rho_{loess} x_{loess}}{\Lambda_i}\right)}\right] \quad (B.1)$$

In this case, the total depth of loess was used to constrain the 3D visualization approach. Two free parameters (exposure age and inheritance) were determined by the previous method (Siame et al., 2004; Rodés et al., 2011).

Model 3: Very recent deposition

In order to get the minimum end-member age, we assume the profile experienced a constant denudation before the very recent deposition of loess (Fig. B.1c). The 3D visualization approach with no variation of density was used to determine denudation rate, exposure age and inheritance.

References

Ackerer, J., Chabaux, F., Van der Woerd, J., Viville, D., Pelt, E., Kali, E., Lerouge, C., Ackerer, P., di Chiara Roupert, R., Négrel, P., 2016. Regolith evolution on the millennial timescale from combined U–Th–Ra isotopes and in situ cosmogenic ^{10}Be analysis in a weathering profile (Strengbach catchment, France). Earth Planet. Sci. Lett. 453, 33-43.

Akçar, N., Ivy-Ochs, S., Alfimov, V., Schlunegger, F., Claude, A., Reber, R., Christl, M., Vockenhuber, C., Dehnert, A., Rahn, M., Schlüchter, C., 2017. Isochron-burial dating of glaciofluvial deposits: First results from the Swiss Alps. Earth Surface Processes and Landforms 42, 2414-2425.

Ansberque, C., Godard, V., Bellier, O., De Sigoyer, J., Liu-Zeng, J., Xu, X., Ren, Z., Li, Y., Team, A.S.T.E.R., 2015. Denudation pattern across the Longriba fault system and implications for the geomorphological evolution of the eastern Tibetan margin. Geomorphology 246, 542-557.

Arnold, M., Merchel, S., Bourlès, D.L., Braucher, R., Benedetti, L., Finkel, R.C., Aumaître, G., Gottdang, A., Klein, M., 2010. The French accelerator mass spectrometry facility ASTER: Improved performance and developments. Nucl. Instrum. Methods Phys. Res. Sect. B-Beam Interact. Mater. Atoms 268, 1954-1959.

Aster, R.C., Borchers, B., Thurber, C.H., 2013. Parameter Estimation and Inverse Problems (Second Edition). Academic Press, Amsterdam.

Bai, M., Chevalier, M.-L., Pan, J., Replumaz, A., Leloup, P.H., Métois, M., Li, H., 2018. Southeastward increase of the late Quaternary slip-rate of the Xianshuihe fault, eastern Tibet. Geodynamic and seismic hazard implications. Earth Planet. Sci. Lett. 485, 19-31.

Balco, G., 2017. Production rate calculations for cosmic-ray-muon-produced 10 Be and 26 Al benchmarked against geological calibration data. Quat. Geochronol. 39, 150-173.

Balco, G., Stone, J.O., Lifton, N.A., Dunai, T.J., 2008. A complete and easily

accessible means of calculating surface exposure ages or erosion rates from ^{10}Be and ^{26}Al measurements. Quat. Geochronol. 3, 174-195.

Bevington, P.R., Robinson, D.K., 2003. Data reduction and error analysis for the physical sciences. McGraw-Hill higher Education, New York.

Bond, G., Broecker, W., Johnsen, S., McManus, J., Labeyrie, L., Jouzel, J., Bonani, G., 1993. Correlations between climate records from North Atlantic sediments and Greenland ice. Nature 365, 143.

Bookhagen, B., 2018. High resolution spatiotemporal distribution of rainfall seasonality and extreme events based on a 12-year TRMM time series. in review.

Borchers, B., Marrero, S., Balco, G., Caffee, M., Goehring, B., Lifton, N., Nishiizumi, K., Phillips, F., Schaefer, J., Stone, J., 2016. Geological calibration of spallation production rates in the CRONUS-Earth project. Quat. Geochronol. 31, 188-198.

Braucher, R., Bourlès, D., Merchel, S., Vidal Romani, J., Fernadez-Mosquera, D., Marti, K., Léanni, L., Chauvet, F., Arnold, M., Aumaître, G., Keddadouche, K., 2013. Determination of muon attenuation lengths in depth profiles from in situ produced cosmogenic nuclides. Nucl. Instrum. Methods Phys. Res. Sect. B-Beam Interact. Mater. Atoms 294, 484-490.

Braucher, R., Brown, E.T., Bourlès, D.L., Colin, F., 2003. In situ produced ^{10}Be measurements at great depths: implications for production rates by fast muons. Earth Planet. Sci. Lett. 211, 251-258.

Braucher, R., Del Castillo, P., Siame, L., Hidy, A.J., Bourlès, D.L., 2009. Determination of both exposure time and denudation rate from an in situ-produced 10Be depth profile: A mathematical proof of uniqueness. Model sensitivity and applications to natural cases. Quat. Geochronol. 4, 56-67.

Braucher, R., Guillou, V., Bourlès, D.L., Arnold, M., Aumaître, G., Keddadouche, K., Nottoli, E., 2015. Preparation of ASTER in-house ^{10}Be/^{9}Be standard solutions. Nucl. Instrum. Methods Phys. Res. Sect. B-Beam Interact. Mater. Atoms 361, 335-340.

Braucher, R., Merchel, S., Borgomano, J., Bourlès, D.L., 2011. Production of cosmogenic radionuclides at great depth: A multi element approach. Earth Planet. Sci. Lett. 309, 1-9.

Bull, W.B., 1991. Geomorphic responses to climatic change. Oxford University Press, New York.

Burbank, D.W., 1992. Causes of recent Himalayan uplift deduced from deposited patterns in the Ganges basin. Nature 357, 680-683.

Burbank, D.W., Leland, J., Fielding, E., Anderson, R.S., 1996. Bedrock incision, rock uplift and threshold hillslopes in the northwestern Himalayas. Nature 379, 505.

Burchfiel, B.C., Chen, Z., Liu, Y., Royden, L.H., 1995. Tectonics of the Longmen Shan and Adjacent Regions, Central China. Int. Geol. Rev. 37, 661-735.

Carretier, S., Regard, V., Vassallo, R., Aguilar, G., Martinod, J., Riquelme, R., Christophoul, F., Charrier, R., Gayer, E., Farías, M., Audin, L., Lagane, C., 2015. Differences in ^{10}Be concentrations between river sand, gravel and pebbles along the western side of the central Andes. Quat. Geochronol. 27, 33-51.

Charreau, J., Saint-Carlier, D., Dominguez, S., Lavé, J., Blard, P.-H., Avouac, J.-P.,

781 Jolivet, M., Chen, Y., Wang, S., Brown, N.D., Malatesta, L.C., Rhodes, E., 2017.
782 Denudation outpaced by crustal thickening in the eastern Tianshan. Earth Planet.
783 Sci. Lett. 479, 179-191.
784 Chen, F., Yu, Z., Yang, M., Ito, E., Wang, S., Madsen, D.B., Huang, X., Zhao, Y.,
785 Sato, T., John B. Birks, H., Boomer, I., Chen, J., An, C., Wünnemann, B., 2008a.
786 Holocene moisture evolution in arid central Asia and its out-of-phase
787 relationship with Asian monsoon history. Quat. Sci. Rev. 27, 351-364.
788 Chen, J., Dai, F., Yao, X., 2008b. Holocene debris-flow deposits and their
789 implications on the climate in the upper Jinsha River valley, China.
790 Geomorphology 93, 493-500.
791 Chevalier, M.-L., Leloup, P.H., Replumaz, A., Pan, J., Métois, M., Li, H., 2017.
792 Temporally constant slip rate along the Ganzi fault, NW Xianshuihe fault system,
793 eastern Tibet. Geol. Soc. Am. Bull. 130, 396-410.
794 Chmeleff, J., von Blanckenburg, F., Kossert, K., Jakob, D., 2010. Determination of
795 the ^{10}Be half-life by multicollector ICP-MS and liquid scintillation counting.
796 Nucl. Instrum. Methods Phys. Res. Sect. B-Beam Interact. Mater. Atoms 268,
797 192-199.
798 Clark, M.K., House, M.A., Royden, L.H., Whipple, K.X., Burchfiel, B.C., Zhang, X.,
799 Tang, W., 2005. Late Cenozoic uplift of southeastern Tibet. Geology 33, 525.
800 Clark, M.K., Royden, L.H., 2000. Topographic ooze: Building the eastern margin of
801 Tibet by lower crustal flow. Geology 28, 703-706.
802 Clark, M.K., Royden, L.H., Whipple, K.X., Burchfiel, B.C., Zhang, X., Tang, W.,
803 2006. Use of a regional, relict landscape to measure vertical deformation of the
804 eastern Tibetan Plateau. J. Geophys. Res.-Earth Surf. 111, F03002.
805 Clark, M.K., Schoenbohm, L.M., Royden, L.H., Whipple, K.X., Burchfiel, B.C.,
806 Zhang, X., Tang, W., Wang, E., Chen, L., 2004. Surface uplift, tectonics, and
807 erosion of eastern Tibet from large-scale drainage patterns. Tectonics 23,
808 TC1006.
809 Clark, P.U., Dyke, A.S., Shakun, J.D., Carlson, A.E., Clark, J., Wohlfarth, B.,
810 Mitrovica, J.X., Hostetler, S.W., McCabe, A.M., 2009. The Last Glacial
811 Maximum. Science 325, 710-714.
812 Codilean, A.T., Fenton, C.R., Fabel, D., Bishop, P., Xu, S., 2014. Discordance
813 between cosmogenic nuclide concentrations in amalgamated sands and
814 individual fluvial pebbles in an arid zone catchment. Quat. Geochronol. 19, 173-
815 180.
816 Cogez, A., Herman, F., Pelt, É., Reuschlé, T., Morvan, G., Darvill, C.M., Norton,
817 K.P., Christl, M., Märki, L., Chabaux, F., 2018. U–Th and ^{10}Be constraints on
818 sediment recycling in proglacial settings, Lago Buenos Aires, Patagonia. Earth
819 Surface Dynamics 6, 121-140.
820 Cui, L.F., Liu, C.Q., Xu, S., Zhao, Z.Q., Liu, T.Z., Liu, W.J., Zhang, Z.J., 2016.
821 Subtropical denudation rates of granitic regolith along a hill ridge in Longnan,
822 SE China derived from cosmogenic nuclide depth-profiles. J. Asian Earth Sci.
823 117, 146-152.
824 Cui, L.F., Liu, C.Q., Xu, S., Zhao, Z.Q., Tu, C.L., Liu, T.Z., Ding, H., 2014. The

long-term denudation rate of granitic regolith in Qinhuangdao, North China determined from the in situ depth profile of the cosmogenic nuclides ^{26}Al and ^{10}Be. Chin. Sci. Bull. 59, 4823-4828.

Delmas, M., Calvet, M., Gunnell, Y., Voinchet, P., Manel, C., Braucher, R., Tissoux, H., Bahain, J.-J., Perrenoud, C., Saos, T., 2018. Terrestrial ^{10}Be and electron spin resonance dating of fluvial terraces quantifies quaternary tectonic uplift gradients in the eastern Pyrenees. Quat. Sci. Rev. 193, 188-211.

Dykoski, C., Edwards, R., Cheng, H., Yuan, D., Cai, Y., Zhang, M., Lin, Y., Qing, J., An, Z., Revenaugh, J., 2005. A high-resolution, absolute-dated Holocene and deglacial Asian monsoon record from Dongge Cave, China. Earth Planet. Sci. Lett. 233, 71-86.

Finnegan, N.J., Schumer, R., Finnegan, S., 2014. A signature of transience in bedrock river incision rates over timescales of 10^4-10^7 years. Nature 505, 391-394.

Fu, P., Stroeven, A.P., Harbor, J.M., Hättestrand, C., Heyman, J., Caffee, M.W., Zhou, L., 2013. Paleoglaciation of Shaluli Shan, southeastern Tibetan Plateau. Quat. Sci. Rev. 64, 121-135.

Gallen, S.F., Pazzaglia, F.J., Wegmann, K.W., Pederson, J.L., Gardner, T.W., 2015. The dynamic reference frame of rivers and apparent transience in incision rates. Geology 43, 623-626.

Gao, Y.X., 1962. On some problems of Asian monsoon. In: Gao, Y.X. (Ed.), Some Problems on East-Asia Monsoon. Science Press, Beijing, pp. 49-63 (in Chinese).

Gardner, T.W., Jorgensen, D.W., Shuman, C., Lemieux, C.R., 1987. Geomorphic and tectonic process rates: effects of measured time interval. Geology 15, 259-261.

Godard, V., Lavé, J., Carcaillet, J., Cattin, R., Bourlès, D., Zhu, J., 2010. Spatial distribution of denudation in Eastern Tibet and regressive erosion of plateau margins. Tectonophysics 491, 253-274.

Godard, V., Pik, R., Lavé, J., Cattin, R., Tibari, B., de Sigoyer, J., Pubellier, M., Zhu, J., 2009. Late Cenozoic evolution of the central Longmen Shan, eastern Tibet: Insight from (U-Th)/He thermochronometry. Tectonics 28, TC5009.

Graf, A.A., Strasky, S., Zhao, Z., Akcar, N., Ivy-Ochs, S., Kubik, P.W., Christal, M., Kasper, H.U., Wieler, R., Schlüchter, C., 2008. Glacier extension on the eastern Tibetan Plateau in response to MIS 2 cooling, with a contribution to ^{10}Be and ^{21}Ne methodology. In: Strasky, S. (ed.), Glacial response to global climate changes: cosmogenic nuclide chronologies from high and low latitudes. ETH Zürich (PhD Thesis).

Granger, D.E., Smith, A.L., 2000. Dating buried sediments using radioactive decay and muogenic production of ^{26}Al and ^{10}Be. Nucl. Instrum. Methods Phys. Res. Sect. B-Beam Interact. Mater. Atoms 172, 822-826.

Guilbaud, C., Simoes, M., Barrier, L., Laborde, A., Van der Woerd, J., Li, H., Tapponnier, P., Coudroy, T., Murray, A., 2017. Kinematics of Active Deformation Across the Western Kunlun Mountain Range (Xinjiang, China) and Potential Seismic Hazards Within the Southern Tarim Basin. J. Geophys. Res.-Solid Earth 122, 10398-10426.

Guralnik, B., Matmon, A., Avni, Y., Porat, N., Fink, D., 2011. Constraining the

evolution of river terraces with integrated OSL and cosmogenic nuclide data. Quat. Geochronol. 6, 22-32.
Hancock, G.S., Anderson, R.S., 2002. Numerical modeling of fluvial strath-terrace formation in response to oscillating climate. Geol. Soc. Am. Bull. 114, 1131-1142.
Hancock, G.S., Anderson, R.S., Chadwick, O.A., Finkel, R.C., 1999. Dating fluvial terraces with ^{10}Be and ^{26}Al profiles: Application to the Wind River, Wyoming. Geomorphology 27, 41-60.
He, Z., Zhang, X., Qiao, Y., Bao, S., Lu, C., He, X., 2015. Formation of the Yalong Downstream Terraces in the SE Tibetan Plateau and Its Implication for the Uplift of the Plateau. Acta Geologica Sinica (English Edition) 89, 542-560.
Heinrich, H., 1988. Origin and consequences of cyclic ice rafting in the Northeast Atlantic Ocean during the past 130,000 years. Quat. Res. 29, 142-152.
Hemming, S.R., 2004. Heinrich events: Massive late Pleistocene detritus layers of the North Atlantic and their global climate imprint. Rev. Geophys. 42, RG1005.
Heyman, J., Stroeven, A.P., Caffee, M.W., Hättestrand, C., Harbor, J.M., Li, Y., Alexanderson, H., Zhou, L., Hubbard, A., 2011. Palaeoglaciology of Bayan Har Shan, NE Tibetan Plateau: exposure ages reveal a missing LGM expansion. Quat. Sci. Rev. 30, 1988-2001.
Hidy, A.J., Gosse, J.C., Pederson, J.L., Mattern, J.P., Finkel, R.C., 2010. A geologically constrained Monte Carlo approach to modeling exposure ages from profiles of cosmogenic nuclides: An example from Lees Ferry, Arizona. Geochem. Geophys. Geosyst. 11, Q0AA10.
Hidy, A.J., Gosse, J.C., Sanborn, P., Froese, D.G., 2018. Age-erosion constraints on an Early Pleistocene paleosol in Yukon, Canada, with profiles of ^{10}Be and ^{26}Al: Evidence for a significant loess cover effect on cosmogenic nuclide production rates. Catena 165, 260-271.
Hu, P., Liu, Q., Heslop, D., Roberts, A.P., Jin, C., 2015. Soil moisture balance and magnetic enhancement in loess–paleosol sequences from the Tibetan Plateau and Chinese Loess Plateau. Earth Planet. Sci. Lett. 409, 120-132.
Huang, W.-L., Yang, X.-p., Li, A., Thompson, J.A., Zhang, L., 2014. Climatically controlled formation of river terraces in a tectonically active region along the southern piedmont of the Tian Shan, NW China. Geomorphology 220, 15-29.
Kirby, E., Reiners, P.W., Krol, M.A., Whipple, K.X., Hodges, K.V., Farley, K.A., Tang, W., Chen, Z., 2002. Late Cenozoic evolution of the eastern margin of the Tibetan Plateau: Inferences from ^{40}Ar/^{39}Ar and (U - Th)/He thermochronology. Tectonics 21, 1-20.
Kirby, E., Whipple, K.X., Burchfiel, B.C., Tang, W., Berger, G., Sun, Z., Chen, Z., 2000. Neotectonics of the Min Shan, China: Implications for mechanisms driving Quaternary deformation along the eastern margin of the Tibetan Plateau. Geol. Soc. Am. Bull. 112, 375-393.
Kong, P., Na, C., Fink, D., Zhao, X., Xiao, W., 2009. Moraine dam related to late Quaternary glaciation in the Yulong Mountains, southwest China, and impacts on the Jinsha River. Quat. Sci. Rev. 28, 3224-3235.

913 Korschinek, G., Bergmaier, A., Faestermann, T., Gerstmann, U.C., Knie, K., Rugel,
914 G., Wallner, A., Dillmann, I., Dollinger, G., von Gostomski, C.L., Kossert, K.,
915 Maiti, M., Poutivtsev, M., Remmert, A., 2010. A new value for the half-life of
916 10Be by Heavy-Ion Elastic Recoil Detection and liquid scintillation counting.
917 Nucl. Instrum. Methods Phys. Res. Sect. B-Beam Interact. Mater. Atoms 268,
918 187-191.
919 Lague, D., 2010. Reduction of long-term bedrock incision efficiency by short-term
920 alluvial cover intermittency. J. Geophys. Res.-Earth Surf. 115, F02011.
921 Lal, D., 1991. Cosmic ray labeling of erosion surfaces: in situ nuclide production rates
922 and erosion models. Earth Planet. Sci. Lett. 104, 424-439.
923 Lisiecki, L.E., Raymo, M.E., 2005. A Pliocene-Pleistocene stack of 57 globally
924 distributed benthic $\delta^{18}O$ records. Paleoceanography 20, 1-17.
925 Liu-Zeng, J., Tapponnier, P., Gaudemer, Y., Ding, L., 2008. Quantifying landscape
926 differences across the Tibetan plateau: Implications for topographic relief
927 evolution. J. Geophys. Res. 113, F04018.
928 Liu-Zeng, J., Wen, L., Oskin, M., Zeng, L., 2011. Focused modern denudation of the
929 Longmen Shan margin, eastern Tibetan Plateau. Geochem. Geophys. Geosyst. 12,
930 Q11007.
931 Liu-Zeng, J., Zhang, J., McPhillips, D., Reiners, P., Wang, W., Pik, R., Zeng, L.,
932 Hoke, G., Xie, K., Xiao, P., Zheng, D., Ge, Y., 2018. Multiple episodes of fast
933 exhumation since Cretaceous in southeast Tibet, revealed by low-temperature
934 thermochronology. Earth Planet. Sci. Lett. 490, 62-76.
935 Liu, J., Chen, J., Zhang, X., Li, Y., Rao, Z., Chen, F., 2015. Holocene East Asian
936 summer monsoon records in northern China and their inconsistency with Chinese
937 stalagmite δ18O records. Earth-Sci. Rev. 148, 194-208.
938 Liu, Y., Zhao, Z., Li, C., Zhang, M., Chen, Y., 2006. Formation of the Zagunao River
939 Terraces in Western Sichuan Plateau, China. Acta Geographica Sinica 61, 249-
940 254 (in Chinese with English abstract).
941 Maddy, D., Bridgland, D.R., Green, C.P., 2000. Crustal uplift in southern England:
942 evidence from the river terrace records. Geomorphology 33, 167-181.
943 Marrero, S.M., Phillips, F.M., Borchers, B., Lifton, N., Aumer, R., Balco, G., 2016.
944 Cosmogenic nuclide systematics and the CRONUScalc program. Quat.
945 Geochronol. 31, 160-187.
946 Martin, L.C.P., Blard, P.H., Balco, G., Lavé, J., Delunel, R., Lifton, N., Laurent, V.,
947 2017. The CREp program and the ICE-D production rate calibration database: A
948 fully parameterizable and updated online tool to compute cosmic-ray exposure
949 ages. Quat. Geochronol. 38, 25-49.
950 Maussion, F., Scherer, D., Mölg, T., Collier, E., Curio, J., Finkelnburg, R., 2014.
951 Precipitation Seasonality and Variability over the Tibetan Plateau as Resolved by
952 the High Asia Reanalysis. J. Clim. 27, 1910-1927.
953 Métivier, F., Gaudemer, Y., Tapponnier, P., Meyer, B., 1998. Northeastward growth
954 of the Tibet plateau deduced from balanced reconstruction of two depositional
955 areas: The Qaidam and Hexi Corridor basins, China. Tectonics 17, 823-842.
956 Mills, H.H., 2000. Apparent increasing rates of stream incision in the eastern United

States during the late Cenozoic. Geology 28, 955-957.
Molnar, P., 2012. Isostasy can't be ignored. Nat. Geosci. 5, 83.
Molnar, P., Boos, W.R., Battisti, D.S., 2010. Orographic Controls on Climate and Paleoclimate of Asia: Thermal and Mechanical Roles for the Tibetan Plateau. Annual Review of Earth and Planetary Sciences 38, 77-102.
Molnar, P., Brown, E.T., Burchfiel, B.C., Deng, Q., Feng, X., Li, J., Raisbeck, G.M., Shi, J., Zhangming, W., Yiou, F., You, H., 1994. Quaternary Climate Change and the Formation of River Terraces across Growing Anticlines on the North Flank of the Tien Shan, China. J. Geol. 102, 583-602.
Murari, M.K., Owen, L.A., Dortch, J.M., Caffee, M.W., Dietsch, C., Fuchs, M., Haneberg, W.C., Sharma, M.C., Townsend-Small, A., 2014. Timing and climatic drivers for glaciation across monsoon-influenced regions of the Himalayan–Tibetan orogen. Quat. Sci. Rev. 88, 159-182.
Nishiizumi, K., 2004. Preparation of ^{26}Al AMS standards. Nucl. Instrum. Methods Phys. Res. Sect. B-Beam Interact. Mater. Atoms 223-224, 388-392.
North Greenland Ice Core Project, M., Andersen, K.K., Azuma, N., Barnola, J.M., Bigler, M., Biscaye, P., Caillon, N., Chappellaz, J., Clausen, H.B., Dahl-Jensen, D., Fischer, H., Flückiger, J., Fritzsche, D., Fujii, Y., Goto-Azuma, K., Grønvold, K., Gundestrup, N.S., Hansson, M., Huber, C., Hvidberg, C.S., Johnsen, S.J., Jonsell, U., Jouzel, J., Kipfstuhl, S., Landais, A., Leuenberger, M., Lorrain, R., Masson-Delmotte, V., Miller, H., Motoyama, H., Narita, H., Popp, T., Rasmussen, S.O., Raynaud, D., Rothlisberger, R., Ruth, U., Samyn, D., Schwander, J., Shoji, H., Siggard-Andersen, M.L., Steffensen, J.P., Stocker, T., Sveinbjörnsdóttir, A.E., Svensson, A., Takata, M., Tison, J.L., Thorsteinsson, T., Watanabe, O., Wilhelms, F., White, J.W.C., 2004. High-resolution record of Northern Hemisphere climate extending into the last interglacial period. Nature 431, 147-151.
Ou, X., Lai, Z., Zhou, S., Zeng, L., 2014. Timing of glacier fluctuations and trigger mechanisms in eastern Qinghai–Tibetan Plateau during the late Quaternary. Quat. Res. 81, 464-475.
Ou, X., Zhang, B., Lai, Z., Zhou, S., Zeng, L., 2013. OSL dating study on the glacial evolutions during the Last Glaciation at Dangzi Valley in the eastern Qinghai-Tibetan Plateau. Progress in Geography 32, 262-269 (in Chinese with English abstract).
Ouimet, W., Whipple, K., Royden, L., Reiners, P., Hodges, K., Pringle, M., 2010. Regional incision of the eastern margin of the Tibetan Plateau. Lithosphere 2, 50-63.
Owen, L.A., Finkel, R.C., Barnard, P.L., Haizhou, M., Asahi, K., Caffee, M.W., Derbyshire, E., 2005. Climatic and topographic controls on the style and timing of Late Quaternary glaciation throughout Tibet and the Himalaya defined by ^{10}Be cosmogenic radionuclide surface exposure dating. Quat. Sci. Rev. 24, 1391-1411.
Owen, L.A., Finkel, R.C., Haizhou, M., Spencer, J.Q., Derbyshire, E., Barnard, P.L., Caffee, M.W., 2003. Timing and style of Late Quaternary glaciation in northeastern Tibet. Geol. Soc. Am. Bull. 115, 1356-1364.

Pan, B., Su, H., Hu, Z., Hu, X., Gao, H., Li, J., Kirby, E., 2009. Evaluating the role of climate and tectonics during non-steady incision of the Yellow River: evidence from a 1.24 Ma terrace record near Lanzhou, China. Quat. Sci. Rev. 28, 3281-3290.

Perrineau, A., Van der Woerd, J., Gaudemer, Y., Liu-Zeng, J., Pik, R., Tapponnier, P., Thuizat, R., Zheng, R., 2011. Incision rate of the Yellow River in Northeastern Tibet constrained by ^{10}Be and ^{26}Al cosmogenic isotope dating of fluvial terraces: implications for catchment evolution and plateau building. Geological Society, London, Special Publications 353, 189-219.

Phillips, F.M., Argento, D.C., Balco, G., Caffee, M.W., Clem, J., Dunai, T.J., Finkel, R., Goehring, B., Gosse, J.C., Hudson, A.M., Jull, A.J.T., Kelly, M.A., Kurz, M., Lal, D., Lifton, N., Marrero, S.M., Nishiizumi, K., Reedy, R.C., Schaefer, J., Stone, J.O.H., Swanson, T., Zreda, M.G., 2016. The CRONUS-Earth Project: A synthesis. Quat. Geochronol. 31, 119-154.

Qiao, Y., Qi, L., Liu, Z., Wang, Y., Yao, H., Yang, J., Zhao, Z., 2014. Intensification of aridity in the eastern margin of the Tibetan Plateau since 300ka BP inferred from loess-soil sequences, western Sichuan Province, southwest China. Paleogeogr. Paleoclimatol. Paleoecol. 414, 192-199.

Rodés, Á., Pallàs, R., Braucher, R., Moreno, X., Masana, E., Bourlès, D.L., 2011. Effect of density uncertainties in cosmogenic ^{10}Be depth-profiles: Dating a cemented Pleistocene alluvial fan (Carboneras Fault, SE Iberia). Quat. Geochronol. 6, 186-194.

Rodés, Á., Pallàs, R., Ortuño, M., García-Melendez, E., Masana, E., 2014. Combining surface exposure dating and burial dating from paired cosmogenic depth profiles. Example of El Límite alluvial fan in Huércal-Overa basin (SE Iberia). Quat. Geochronol. 19, 127-134.

Roger, F., Jolivet, M., Malavieille, J., 2008. Tectonic evolution of the Triassic fold belts of Tibet. C. R. Geosci. 340, 180-189.

Roger, F., Jolivet, M., Malavieille, J., 2010. The tectonic evolution of the Songpan-Garzê (North Tibet) and adjacent areas from Proterozoic to Present: A synthesis. J. Asian Earth Sci. 39, 254-269.

Rohling, E.J., Hibbert, F.D., Williams, F.H., Grant, K.M., Marino, G., Foster, G.L., Hennekam, R., de Lange, G.J., Roberts, A.P., Yu, J., Webster, J.M., Yokoyama, Y., 2017. Differences between the last two glacial maxima and implications for ice-sheet, δ^{18}O, and sea-level reconstructions. Quat. Sci. Rev. 176, 1-28.

Royden, L.H., Burchfiel, B.C., King, R.W., Wang, E., Chen, Z., Shen, F., Liu, Y., 1997. Surface Deformation and Lower Crustal Flow in Eastern Tibet. Science 276, 788-790.

Ruszkiczay-Rüdiger, Z., Braucher, R., Novothny, Á., Csillag, G., Fodor, L., Molnár, G., Madarász, B., 2016. Tectonic and climatic control on terrace formation: Coupling in situ produced ^{10}Be depth profiles and luminescence approach, Danube River, Hungary, Central Europe. Quat. Sci. Rev. 131, 127-147.

Saint-Carlier, D., Charreau, J., Lavé, J., Blard, P.-H., Dominguez, S., Avouac, J.-P., Wang, S., 2016. Major temporal variations in shortening rate absorbed along a

large active fold of the southeastern Tianshan piedmont (China). Earth Planet. Sci. Lett. 434, 333-348.
Schäfer, J.M., Tschudi, S., Zhao, Z., Wu, X., Ivy-Ochs, S., Wieler, R., Baur, H., Kubik, P.W., Schlüchter, C., 2002. The limited influence of glaciations in Tibet on global climate over the past 170 000 yr. Earth Planet. Sci. Lett. 194, 287-297.
Schaller, M., Ehlers, T.A., Lang, K.A.H., Schmid, M., Fuentes-Espoz, J.P., 2018. Addressing the contribution of climate and vegetation cover on hillslope denudation, Chilean Coastal Cordillera (26°–38°S). Earth Planet. Sci. Lett. 489, 111-122.
Schaller, M.F., von Blanckenburg, F., Veldkamp, A., Tebbens, L.A., Hovius, N., Kubik, P.W., 2002. A 30000 yr record of erosion rates from cosmogenic ^{10}Be in Middle European river terraces. Earth Planet. Sci. Lett. 204, 307-320.
Schumer, R., Jerolmack, D.J., 2009. Real and apparent changes in sediment deposition rates through time. J. Geophys. Res. 114, F00A06.
Siame, L., Bellier, O., Braucher, R., Sébrier, M., Cushing, M., Bourlès, D., Hamelin, B., Baroux, E., de Voogd, B., Raisbeck, G., Yiou, F., 2004. Local erosion rates versus active tectonics: cosmic ray exposure modelling in Provence (south-east France). Earth Planet. Sci. Lett. 220, 345-364.
Sordi, V.D.M., Salgado, A.A.R., Siame, L., Bourlès, D., Paisani, J.C., Léanni, L., Braucher, R., Couto, V.d.E., Team, A., 2018. Implications of drainage rearrangement for passive margin escarpment evolution in southern Brazil. Geomorphology 306, 155-169.
Stone, J.O., 2000. Air pressure and cosmogenic isotope production. J. Geophys. Res.-Solid Earth 105, 23753-23759.
Strasky, S., Graf, A.A., Zhao, Z., Kubik, P.W., Baur, H., Schlüchter, C., Wieler, R., 2009. Late Glacial ice advances in southeast Tibet. J. Asian Earth Sci. 34, 458-465.
Tapponnier, P., Xu, Z., Roger, F., Meyer, B., Arnaud, N., Wittlinger, G., Yang J., 2001. Oblique stepwise rise and growth of the Tibet plateau. Science 294, 1671-1677.
Taylor, M., Yin, A., 2009. Active structures of the Himalayan-Tibetan orogen and their relationships to earthquake distribution, contemporary strain field, and Cenozoic volcanism. Geosphere 5, 199-214.
Tian, Y., Li, R., Tang, Y., Xu, X., Wang, Y., Zhang, P., 2018. Thermochronological Constraints on the Late Cenozoic Morphotectonic Evolution of the Min Shan, the Eastern Margin of the Tibetan Plateau. Tectonics 37, 1733-1749.
Tschudi, S., Schäfer, J.M., Zhao, Z., Wu, X., Ivy-Ochs, S., Kubik, P.W., Schlüchter, C., 2003. Glacial advances in Tibet during the Younger Dryas? Evidence from cosmogenic ^{10}Be, ^{26}Al, and ^{21}Ne. J. Asian Earth Sci. 22, 301-306.
Vermeesch, P., 2007. CosmoCalc: An Excel add-in for cosmogenic nuclide calculations. Geochem. Geophys. Geosyst. 8, Q08003.
Wang, E., Burchfiel, B.C., 2000. Late Cenozoic to Holocene deformation in southwestern Sichuan and adjacent Yunnan, China, and its role in formation of the southeastern part of the Tibetan Plateau. Geol. Soc. Am. Bull. 112, 413-423.

Wang, E., Kirby, E., Furlong, K.P., van Soest, M., Xu, G., Shi, X., Kamp, P.J.J., Hodges, K.V., 2012. Two-phase growth of high topography in eastern Tibet during the Cenozoic. Nat. Geosci. 5, 640-645.

Wang, J., Raisbeck, G.M., Xu, X., Yiou, F., Bai, S., 2006. In situ cosmogenic 10Be dating of the Quaternary glaciations in the southern Shaluli Mountain on the Southeastern Tibetan Plateau. Science in China Series D: Earth Sciences 49, 1291-1298.

Wang, Y.J., Cheng, H., Edwards, R.L., An, Z.S., Wu, J.Y., Shen, C.C., Dorale, J.A., 2001. A high-resolution absolute-dated late Pleistocene Monsoon record from Hulu Cave, China. Science 294, 2345-2348.

Whipple, K.X., 2004. Bedrock Rivers and the Geomorphology of Active Orogens. Annual Review of Earth and Planetary Sciences 32, 151-185.

Whipple, K.X., 2009. The influence of climate on the tectonic evolution of mountain belts. Nat. Geosci. 2, 97.

Whipple, K.X., Tucker, G.E., 2002. Implications of sediment-flux-dependent river incision models for landscape evolution. J. Geophys. Res.-Solid Earth 107, ETG 3-1-ETG 3-20.

Wittmann, H., von Blanckenburg, F., Maurice, L., Guyot, J.L., Kubik, P.W., 2011. Recycling of Amazon floodplain sediment quantified by cosmogenic ^{26}Al and ^{10}Be. Geology 39, 467-470.

Wu, T., Xiao, L., Wilde, S.A., Ma, C.-Q., Zhou, J.-X., 2017. A mixed source for the Late Triassic Garzê-Daocheng granitic belt and its implications for the tectonic evolution of the Yidun arc belt, eastern Tibetan Plateau. Lithos 288-289, 214-230.

Xu, L., Ou, X., Lai, Z., Zhou, S., Wang, J., Fu, Y., 2010. Timing and style of Late Pleistocene glaciation in the Queer Shan, northern Hengduan Mountains in the eastern Tibetan Plateau. J. Quat. Sci. 25, 957-966.

Xu, L., Zhou, S., 2009. Quaternary glaciations recorded by glacial and fluvial landforms in the Shaluli Mountains, Southeastern Tibetan Plateau. Geomorphology 103, 268-275.

Xu, X., Wang, J., Zhu, J., Jiang, H., Yang, Y., 2004. Study on glacial erosion surface of the southeast of Qinghai-Xizang Plateau using cosmogenic isotopes dating. Scientia Geographica Sinica 24, 101-104 (in Chinese with English abstract).

Yan, B., Lin, A., 2017. Holocene activity and paleoseismicity of the Selaha Fault, southeastern segment of the strike-slip Xianshuihe Fault Zone, Tibetan Plateau. Tectonophysics 694, 302-318.

Yin, A., Harrison, T.M., 2000. Geologic Evolution of the Himalayan-Tibetan Orogen. Annual Review of Earth & Planetary Sciences 28, 211-280.

Yuan, D., Cheng, H., Edwards, R.L., Dykoski, C.A., Kelly, M.J., Zhang, M., Qing, J., Lin, Y., Wang, Y., Wu, J., Dorale, J.A., An, Z., Cai, Y., 2004. Timing, Duration, and Transitions of the Last Interglacial Asian Monsoon. Science 304, 575-578.

Zhang, B., Ou, X., Lai, Z., 2012. OSL ages revealing the glacier retreat in the Dangzi valley in the eastern Tibetan Plateau during the Last Glacial Maximum. Quat. Geochronol. 10, 244-249.

Zhang, J., Liu-Zeng, J., Scherler, D., Yin, A., Wang, W., Tang, M., Li, Z., 2018.

Spatiotemporal variation of late Quaternary river incision rates in southeast Tibet, constrained by dating fluvial terraces. Lithosphere 10, 662-675.

Zhang, Z., Wang, J., Xu, X., BAI, S., Chang, Z.Y., 2015. Cosmogenic ^{10}Be and ^{26}Al Chronology of the Last Glaciation of the Palaeo-Daocheng Ice Cap, Southeastern Qinghai-Tibetan Plateau. Acta Geologica Sinica (English Edition) 89, 575-584.

Zhao, Z.J., Liu, Y., Chen, Y., Zhang, M.H., Shu, Q., Li, C.L., 2013. Quaternary fluvial incision rates of the Western Sichuan Plateau inferred from ESR chronology. Journal of Lanzhou University 49, 160-172 (in Chinese with English abstract).

Zhou, S., Xu, L., Cui, J., Zhang, X., Zhao, J., 2005. Geomorphologic evolution and environmental changes in the Shaluli Mountain region during the Quaternary. Chin. Sci. Bull. 50, 52-57.

Figure captions

Fig. 1. (a) Topographic map of eastern Tibetan Plateau based on 90-m-resolution Shuttle Radar Topography Mission (SRTM) digital elevation model and major geologic structures (modified from Tapponnier et al., 2001; Clark et al., 2005; Taylor and Yin, 2009; Wu et al., 2017; Liu-Zeng et al., 2018). YGF, Yushu-Ganzi Fault; XSHF, Xianshuihe Fault; ANHF, Anninghe Fault; XJF, Xiaojiang Fault; LTF, Litang Fault; MJF, Minjiang Fault; KLF, Kunlun Fault; XJG, Xiaojinhe Fault; BRKF, Barkam Fault; DSF, Dianshan Fault; BNSZ, Bangongcuo-Nujiang Suture Zone; JSZ, Jinshajiang Suture Zone; GLSZ, Ganzi-Litang Suture Zone; LMSTB, Longmenshan Thrust Belt. Inset: Location of study area. Dashed line represents transition between Eastern Asian monsoon, Indian monsoon and Westerlies (Gao, 1962). (b) Spatial distribution of annually averaged precipitation in eastern Tibetan Plateau from Tropical Rainfall Measuring Mission (TRMM) data (Bookhagen, 2018).

1161 Fig. 2. Sample locations of Wumingshan regolith (a and d), Xianshuihe (b and e) and
1162 Zagunao rivers (c and f), superimposed on shaded relief and contour lines,
1163 respectively. (g) and (h) show cross-profile sketchs for Xianshuihe and Zagunao
1164 fluvial terrace sequences. Red bars indicate sampling sites of depth profiles. Green
1165 bars are burial samples. In b, black line is approximate position of synthetic section
1166 of figure 8.

1167

1168 Fig. 3. (a-b) Field photographs of Wumingshan regolith showing the vertical section
1169 with clear boundary between bedrock and overlying saprolite. (c-e) Field
1170 photographs showing location of sampling sites above Xianshuihe river and thick
1171 loess cover. (f-g) Field photographs showing five levels of fluvial terraces above
1172 Zagunao river and (h) important slope instabilities.

1173

1174 Fig. 4. (a) Correlation of ^{10}Be and ^{26}Al concentrations. Solid line is best fit, excluding
1175 two outliers (grey circles). Black dashed line presents production ratio of ^{26}Al/^{10}Be
1176 = 6.61 following Braucher et al. (2011). (b) Normalized ^{26}Al/^{10}Be ratios plotted
1177 against ^{10}Be concentrations (modified from Vermeesch (2007) and scaled to SLHL).
1178 Steady-state erosion island (shaded yellow) showing saturation values for ^{26}Al/^{10}Be
1179 for different erosion rates (red line). Open ellipses represent depth profile samples
1180 with 2σ uncertainties. Shaded grey ellipses are burial samples, excluding two
1181 outliers (dashed ellipses).

1182

1183 Fig. 5. Cosmogenic ^{10}Be depth profile data, field photographs and integrated bulk
1184 density of Wumingshan regolith (a), Xianshuihe (b, c, and d) and Zagunao rivers (e
1185 and f). Orange and blue curves show fitting solutions that match χ^2 values within
1186 limits of $[\chi^2_{min}; \chi^2_{min}+1]$ and best group with smallest χ^2 values ($\chi^2_{min}\times 1.01$),
1187 respectively. Red curves show variation of nuclide concentration in loess under the
1188 assumption of a constant inheritance. Inset text gives exposure age, denudation rate,
1189 and inheritance. Solid and dashed green lines, respectively, show integrated bulk
1190 density and bulk density. Purple curve shows forward model solution (e.g.,
1191 Perrineau et al., 2011) with two-stages model.
1192
1193 Fig. 6. (a) Spatial distribution of previous exposure/burial ages (circle), basin-wide
1194 denudation rates (triangle), and fluvial incision rates (square) over eastern Tibetan
1195 Plateau (data in supplementary Tables 3-5). (b) Distribution of basin-wide
1196 denudation rates for modern river sediments. We excluded 18 outliers greater than
1197 800 mm/ka (data in supplementary Table 3). (c) Distribution of exposure and burial
1198 ages (data in supplementary Table 4). Red curve represents relative probability
1199 density function with 1σ error.
1200
1201 Fig. 7. Comparison of fluvial terraces abandonment ages with b) paleoclimatic records
1202 from North Greenland Ice Core Project (NGRIP) oxygen isotope record (North
1203 Greenland Ice Core Project et al., 2004), Hulu cave stalagmites oxygen isotope
1204 record (Wang et al., 2001), Dongge cave stalagmites oxygen isotope record (Yuan

et al., 2004; Dykoski et al., 2005), and e) stacked Benthic oxygen isotope curve (Lisiecki and Raymo, 2005). Blue dashed lines in (a) and (d) show linear relationship between terrace elevations and abandonment ages at different timescales. Yellow bands in (b) indicate timing and duration of Younger Dryas (YD) and Heinrich events 1 and 2 (H1 and H2) (Bond et al., 1993; Hemming, 2004). Purple bands in (b) represent continuous glaciation termed monsoonal Himalayan-Tibetan stages (MOHITS) from MOHITS 1A to MOHITS 2D (Murari et al., 2014). Previous data in (c) are presented in supplementary Table 5. ESR ages of Xianshuihe and Zagunao rivers are from Zhao et al. (2013) and Liu et al. (2006), respectively. Red numbers in (d) represent average incision rate from formation of terrace to present.

Fig. 8. Simplified model to illustrate river bed evolution of Xianshuihe river and relationship between bedrock erosion, fluvial incision and terrace formation and abandonment. Yellow bars show the lag time between uplift and incision, when river incision is periodically cancelled during hyper-arid conditions or low sediment discharge (e.g., Whipple, 2004; Ouimet et al., 2010). Blue bars show episodic incision hiatuses, including river bed aggradation and return to pre-deposition (e.g., Finnegan et al., 2014). TCN and ESR ages are from this study and Zhao et al. (2013), respectively.

Figure captions in Appendix

Fig. A.1. Three-dimensional-graph visualization approach and statistical analysis of possible solutions. Data from Ackerer et al. (2016). (a) purple and black points represent possible solutions within 2σ and 1σ confidence levels, respectively; (b) black and orange points represent possible solutions within 1σ confidence level and $\chi^2_{min}+1$, respectively (see detail in Appendix A); (c-e) χ^2 value plots for denudation rate, exposure age and inheritance, in addition, inset diagrams show probability distribution functions (PDFs) and cumulative distribution functions (CDFs); (f) Cosmogenic nuclide concentration as a function of depth for possible solutions within confidence level.

Fig. B.1. Schematic diagrams illustrate variable-density approach with three different loess cover models. (a) Model 1: instantaneous loess deposition after terrace abandonment and post-deposition constant denudation； (b) Model 2: continuous loess deposition at a constant accumulation rate after terrace abandonment; (c) Model 3: experience a constant denudation of terrace before very recent loess deposition event.

Supplementary Figures

Fig. S.1. Model self-check using theoretical concentrations undergoing an exposure age of 20 ka or 800 ka, denudation rate of 10 mm/ka, and inheritance of 100,000 at/g. (a) Inverted solutions calculated from three-dimensional-graph visualization approach by using theoretical concentrations (presented in insert table with error of

about 5%). (b) Five colored curves show that largely different solutions can very well fit the same curve (black) using inversion approach. Inset table shows three free parameter values used for simulation. (c) and (d) 3D-graphs show the possible solutions within 1σ confidence. (e) and (f) Age-denudation rate solution spaces. Orange and blue curves show fitting solutions that match χ^2 values within limits of $[\chi^2_{min}; \chi^2_{min}+1]$ and best group with smallest χ^2 values ($\chi^2_{min}\times 1.01$), respectively.

Fig. S.2. Results of Wumingshan regolith. (a-c) Denudation rate, exposure age and inheritance versus χ^2 values diagrams; (g) Cosmogenic nuclide concentration as a function of depth.

Fig. S.3. Cosmogenic ^{26}Al depth profile data, field photographs and integrated bulk density of Wumingshan regolith (a), Xianshuihe (b, c, and d) and Zagunao (e and f) rivers. Orange and blue curves show fitting solutions that match χ^2 values within limits of $[\chi^2_{min}; \chi^2_{min}+1]$ and best group with smallest χ^2 values ($\chi^2_{min}\times 1.01$), respectively. Red curves show variation of nuclide concentration in loess under the assumption of a constant inheritance. Inset text gives exposure age, denudation rate, and inheritance. Solid and dashed green lines, respectively, show integrated bulk density and bulk density. Purple curve shows forward model solution (e.g., Perrineau et al., 2011) with two-stages model.

Fig. S.4. Results of Wumingshan regolith using method of Hidy et al. (2010).

Table captions

Table 1. Sampling sites, scaled surface cosmogenic ^{10}Be and ^{27}Al production rates and modeled exposure ages.

Table 2. ^{10}Be and ^{26}Al cosmogenic isotope data.

Supplementary table captions

Supplementary table 1. Statistical analysis for all possible solutions in shaded area of depth profile. Depth profiles of Ackerer et al. (2016) and Wumingshan (this study).

Supplementary table 2. Statistical analysis for all possible solutions in orange shaded area of ^{10}Be depth profile.

Supplementary table 3. Summary of published basin-wide denudation rates data.

Supplementary table 4. Summary of published exposure/burial ages data.

Supplementary table 5. Summary of published fluvial incision rates data.

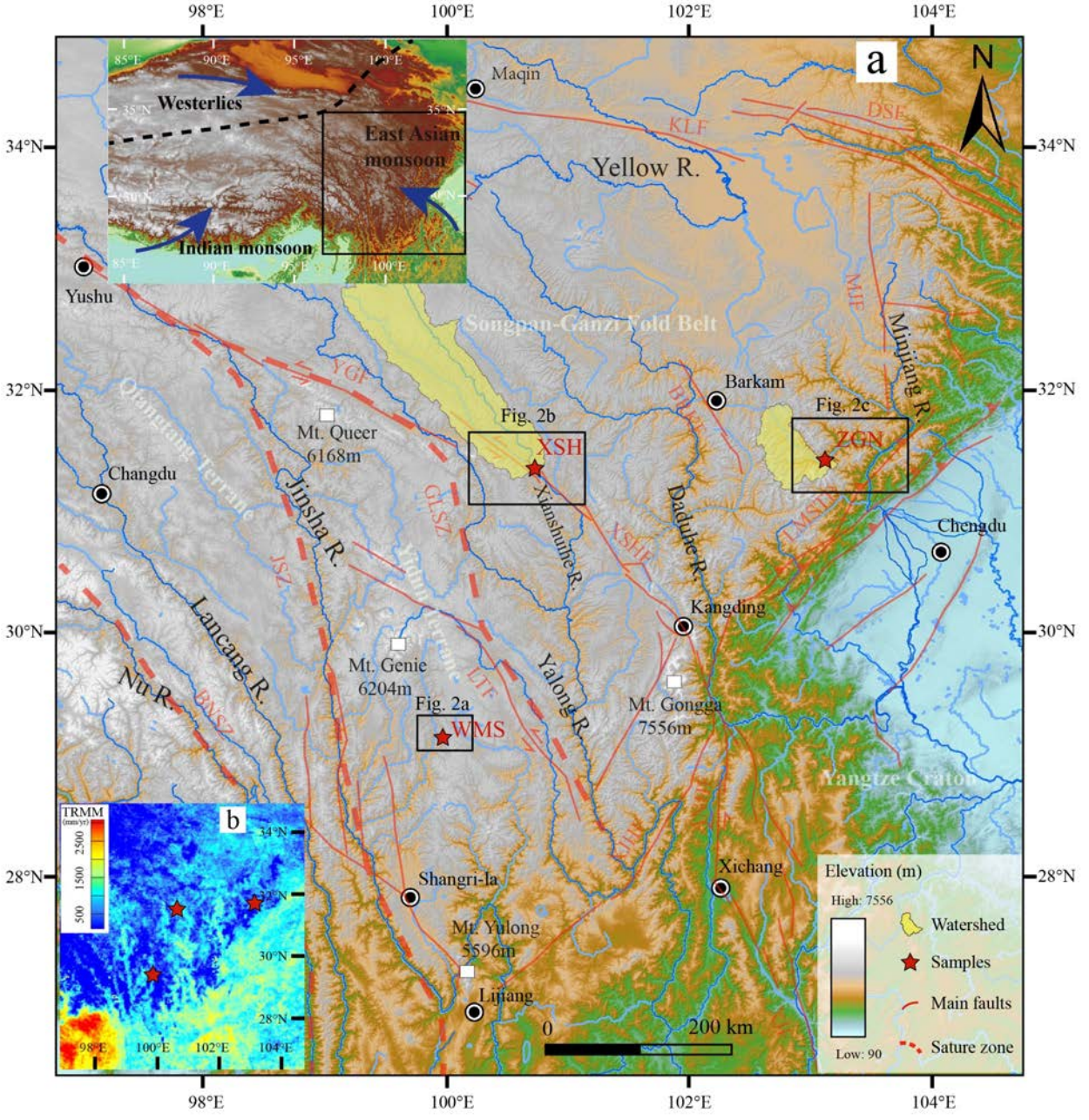
a
N
Westerlies
East Asian monsoon
Indian monsoon
Maqin
Yellow R.
KLF
DSF
Yushu
Songpan-Ganzi Fold Belt
MJF
Minjiang R.
YGF
Barkam
Fig. 2b
Fig. 2c
XSH
ZGN
Mt. Queer 6168m
Changdu
Qiangtang Terrane
Jinsha R.
GLSZ
Xianshuihe R.
XSHF
Daduhe R.
LMSZ
Chengdu
JSZ
Kangding
Lancang R.
Nu R.
Mt. Genie 6204m
Fig. 2a
WMS
LTF
Yalong R.
Mt. Gongga 7556m
BNSZ
Yangtze Craton
Shangri-la
Xichang
Mt. Yulong 5596m
Lijiang
0
200 km
Elevation (m)
High: 7556
Low: 90
Watershed
Samples
Main faults
Sature zone
b
TRMM
(mm/yr)
2500
1500
500
98°E
100°E
102°E
104°E
34°N
32°N
30°N
28°N

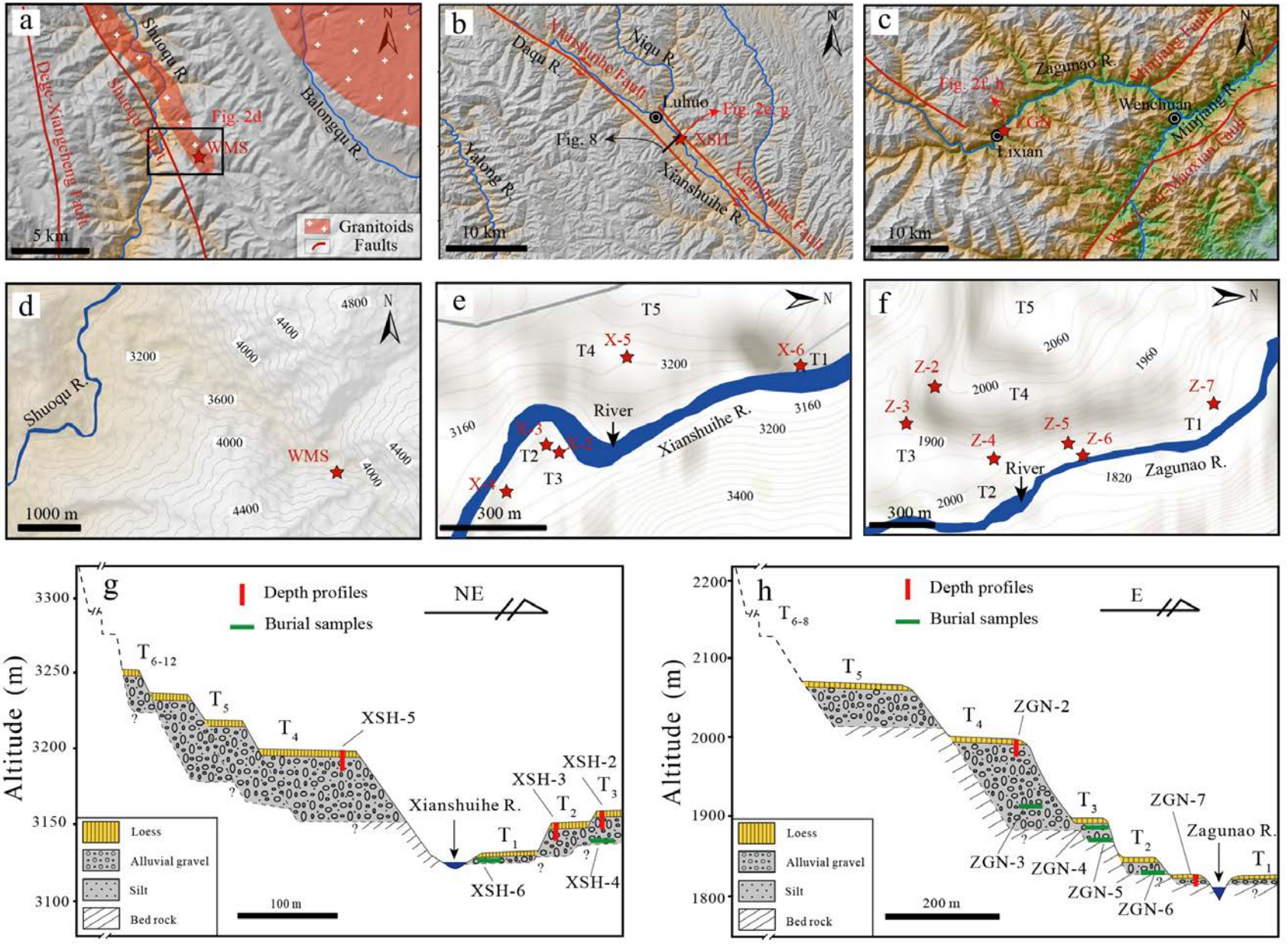
a
Deng-Xiangcheng Fault
Shuoqu R.
Shuoqu Fault
Fig. 2d
WMS
Balongqu R.
N
5 km
Granitoids
Faults
b
Daqu R.
Xianshuihe Fault
Niqu R.
Luhuo
Fig. 2e, g
XSH
Fig. 8
Yalong R.
Xianshuihe R.
Xianshuihe Fault
N
10 km
c
Zagunao R.
Minjiang Fault
Fig. 2f, h
ZGN
Wenchuan
Lixian
Minjiang R.
Huya-Tuanjie-Maoxian Fault
N
10 km
d
4800
N
4400
4000
3200
Shuoqu R.
3600
4000
WMS
4400
4000
4400
1000 m
e
T5
N
T4
X-5
X-6
T1
3200
River
3160
3160
X-3
X-2
Xianshuihe R.
3200
T2
T3
X-4
3400
300 m
f
T5
N
2060
1960
Z-2
2000
T4
Z-7
Z-3
Z-5
T1
1900
Z-4
Z-6
T3
River
Zagunao R.
1820
T2
2000
300 m
g
Depth profiles
Burial samples
NE
3300
3250
3200
3150
3100
Altitude (m)
T6-12
T5
T4
XSH-5
XSH-2
XSH-3
T3
T2
Xianshuihe R.
T1
XSH-6
XSH-4
Loess
Alluvial gravel
Silt
Bed rock
100 m
h
Depth profiles
Burial samples
E
2200
2100
2000
1900
1800
Altitude (m)
T6-8
T5
T4
ZGN-2
T3
ZGN-7
T2
Zagunao R.
ZGN-3
ZGN-4
T1
ZGN-5
ZGN-6
Loess
Alluvial gravel
Silt
Bed rock
200 m

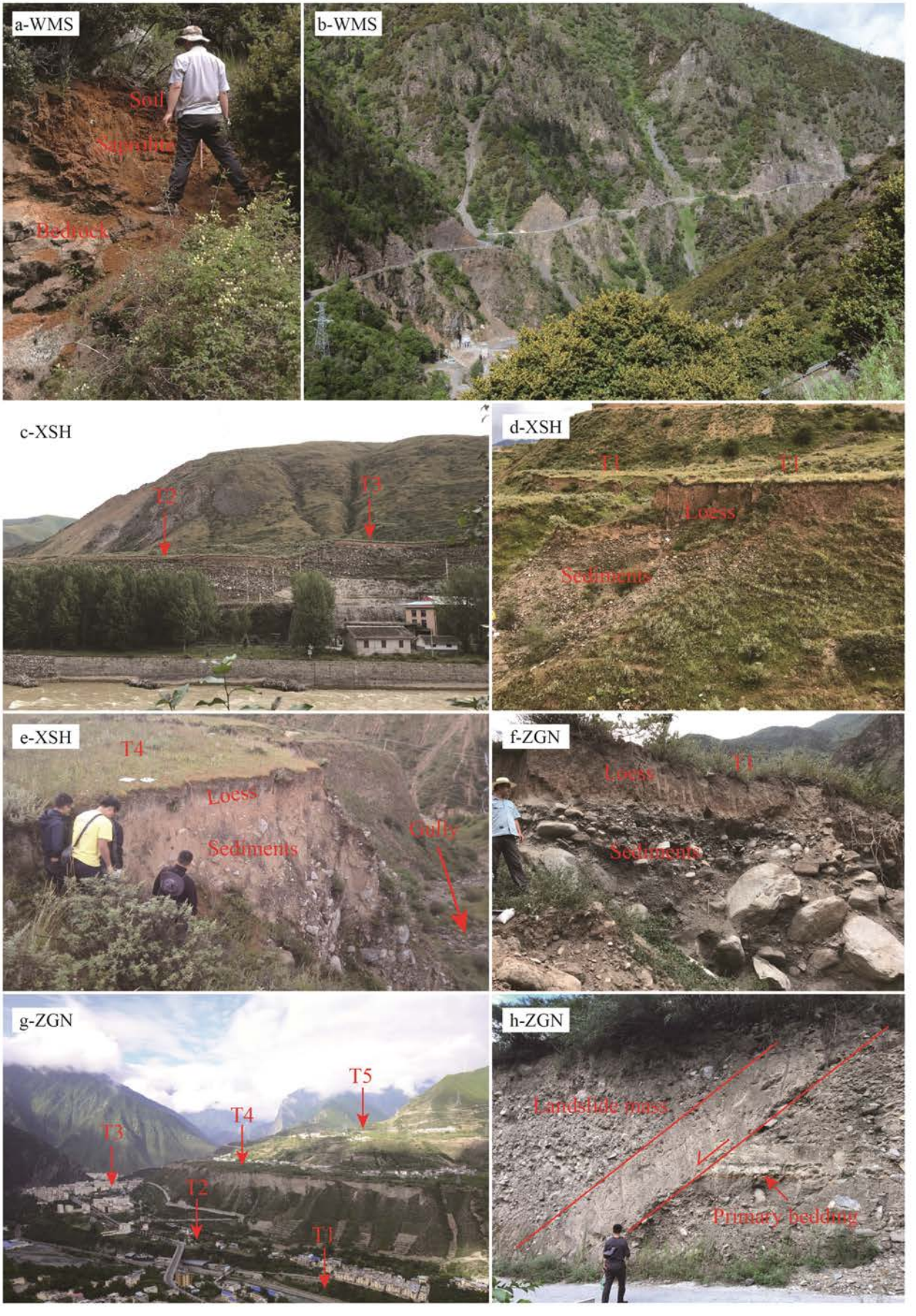
a-WMS
Soil
Saprolite
Bedrock
b-WMS
c-XSH
T2
T3
d-XSH
T1
T1
Loess
Sediments
e-XSH
T4
Loess
Sediments
Gully
f-ZGN
Loess
T1
Sediments
g-ZGN
T5
T4
T3
T2
T1
h-ZGN
Landslide mass
Primary bedding

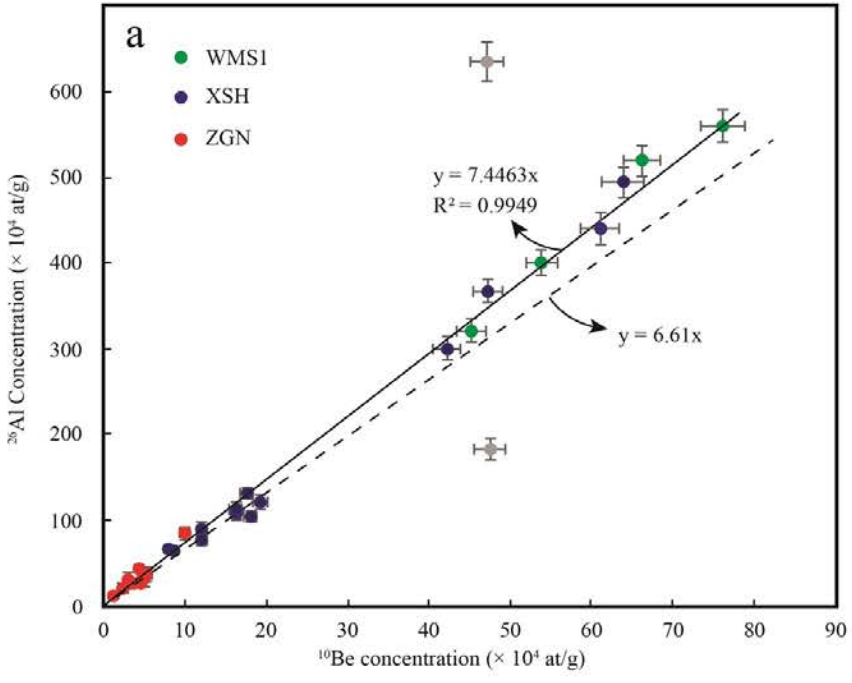
a
WMS1
XSH
ZGN
y = 7.4463x
R² = 0.9949
y = 6.61x
²⁶Al Concentration (× 10⁴ at/g)
¹⁰Be concentration (× 10⁴ at/g)
0
100
200
300
400
500
600
0
10
20
30
40
50
60
70
80
90

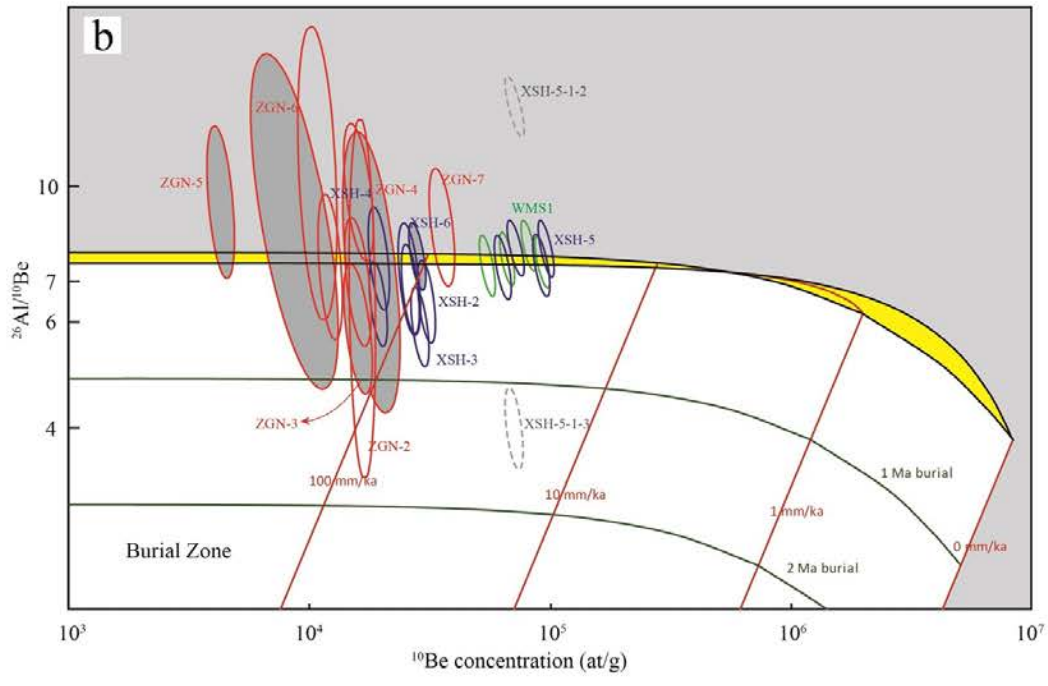
b
ZGN-6
XSH-5-1-2
ZGN-5
XSH-4
ZGN-4
ZGN-7
WMS1
XSH-6
XSH-5
XSH-2
XSH-3
ZGN-3
XSH-5-1-3
ZGN-2
100 mm/ka
10 mm/ka
1 mm/ka
0 mm/ka
1 Ma burial
2 Ma burial
Burial Zone
²⁶Al/¹⁰Be
¹⁰Be concentration (at/g)
4
6
7
10
10³
10⁴
10⁵
10⁶
10⁷

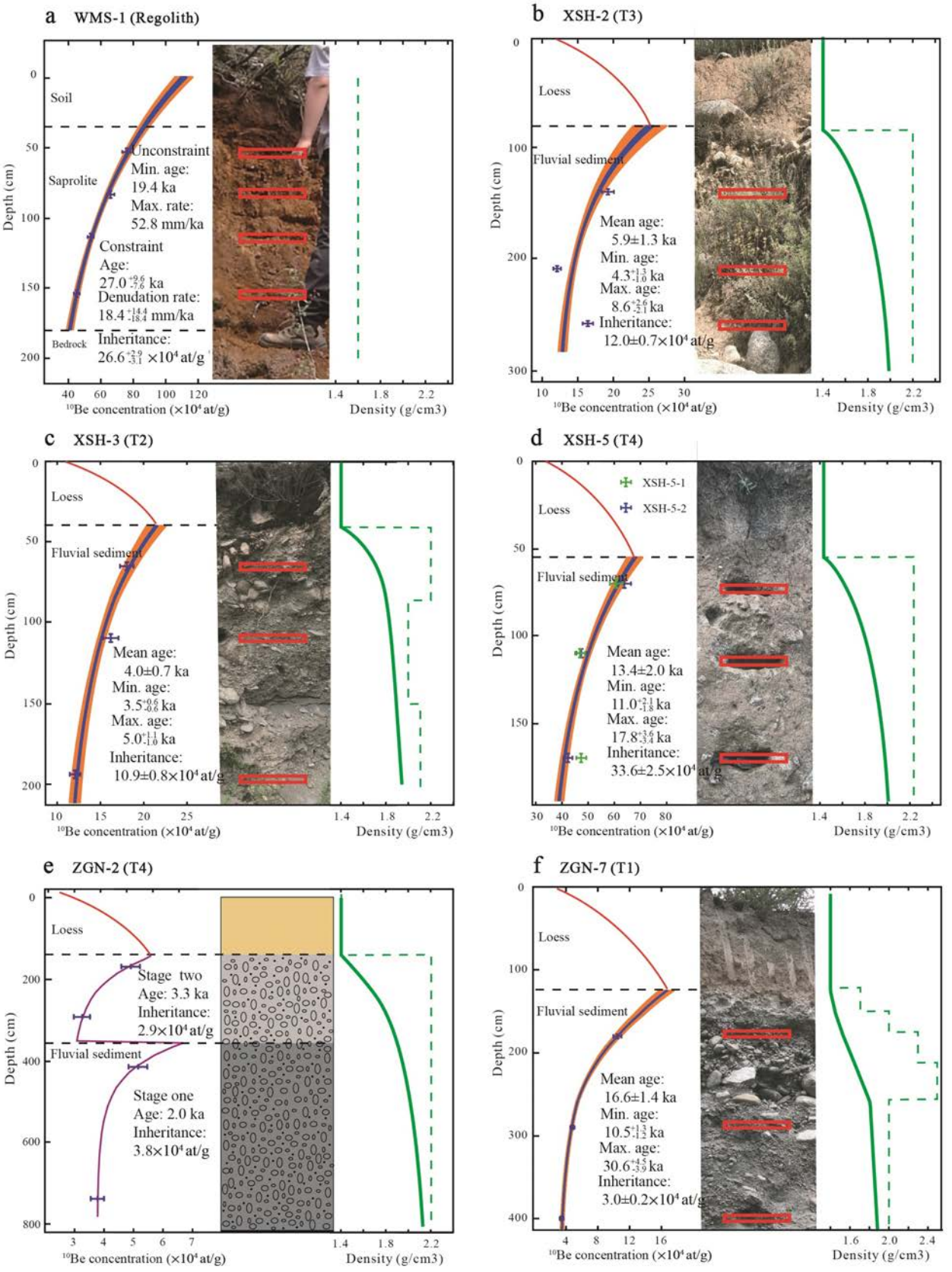
a WMS-1 (Regolith)
Soil
Saprolite
Bedrock
Unconstraint
Min. age:
19.4 ka
Max. rate:
52.8 mm/ka
Constraint
Age:
27.0 +9.6 -7.6 ka
Denudation rate:
18.4 +14.4 -18.4 mm/ka
Inheritance:
26.6 +2.9 -3.1 ×10⁴ at/g
Depth (cm)
10Be concentration (×10⁴ at/g)
Density (g/cm3)
b XSH-2 (T3)
Loess
Fluvial sediment
Mean age:
5.9±1.3 ka
Min. age:
4.3 +1.3 -1.0 ka
Max. age:
8.6 +2.6 -2.1 ka
Inheritance:
12.0±0.7×10⁴ at/g
c XSH-3 (T2)
Loess
Fluvial sediment
Mean age:
4.0±0.7 ka
Min. age:
3.5 +0.6 -0.6 ka
Max. age:
5.0 +1.1 -1.0 ka
Inheritance:
10.9±0.8×10⁴ at/g
d XSH-5 (T4)
XSH-5-1
XSH-5-2
Loess
Fluvial sediment
Mean age:
13.4±2.0 ka
Min. age:
11.0 +2.1 -1.8 ka
Max. age:
17.8 +3.6 -3.4 ka
Inheritance:
33.6±2.5×10⁴ at/g
e ZGN-2 (T4)
Loess
Stage two
Age: 3.3 ka
Inheritance:
2.9×10⁴ at/g
Fluvial sediment
Stage one
Age: 2.0 ka
Inheritance:
3.8×10⁴ at/g
f ZGN-7 (T1)
Loess
Fluvial sediment
Mean age:
16.6±1.4 ka
Min. age:
10.5 +1.3 -1.2 ka
Max. age:
30.6 +4.5 -3.9 ka
Inheritance:
3.0±0.2×10⁴ at/g

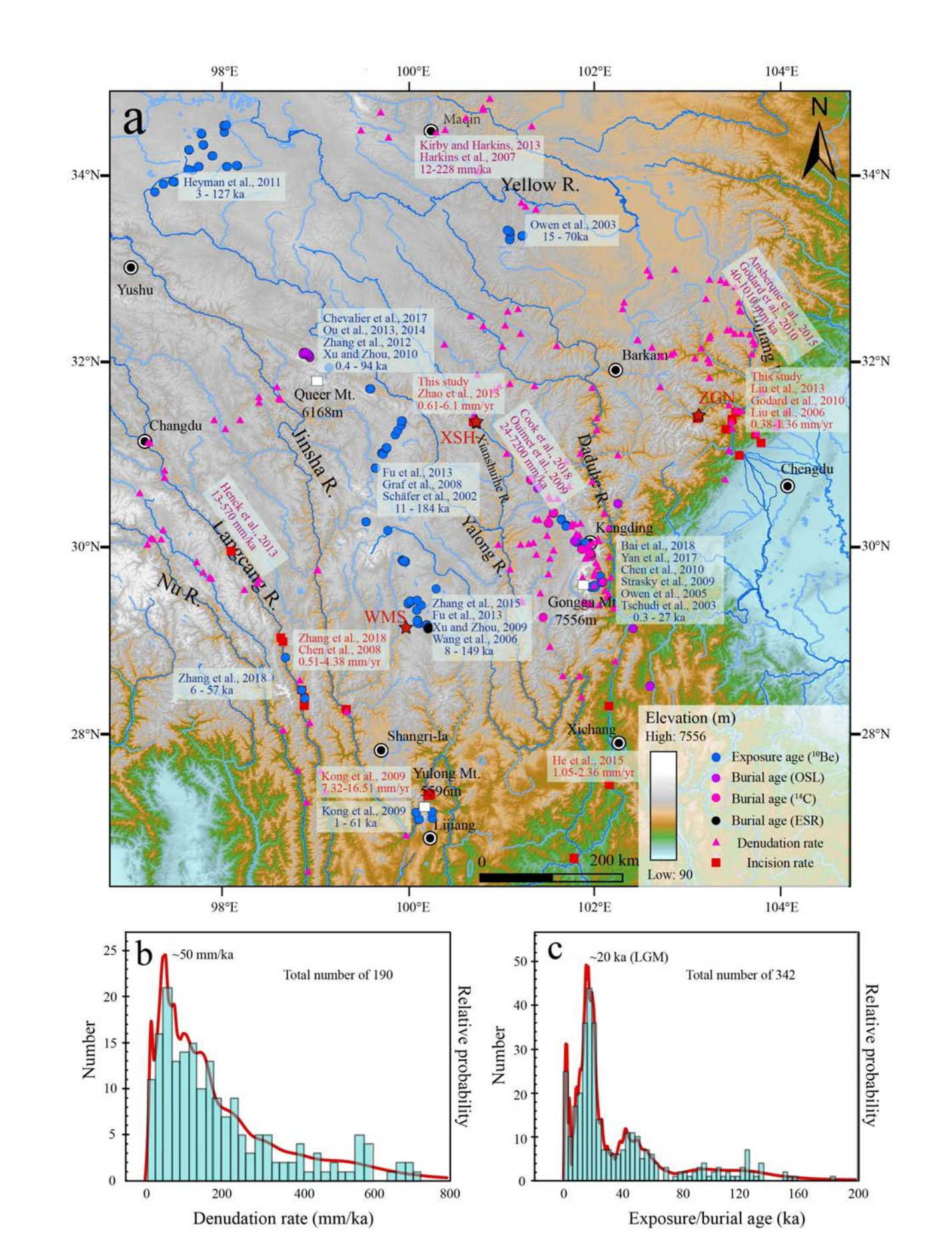
a
98°E
100°E
102°E
104°E
34°N
32°N
30°N
28°N
N
Maqin
Kirby and Harkins, 2013
Harkins et al., 2007
12-228 mm/ka
Yellow R.
Heyman et al., 2011
3 - 127 ka
Owen et al., 2003
15 - 70ka
Yushu
Ansberque et al., 2015
Godard et al., 2010
40-1010 mm/ka
Liujiang
Chevalier et al., 2017
Qu et al., 2013, 2014
Zhang et al., 2012
Xu and Zhou, 2010
0.4 - 94 ka
Barkam
Queer Mt.
6168m
This study
Zhao et al., 2013
0.61-6.1 mm/yr
This study
Liu et al., 2013
Godard et al., 2010
Liu et al., 2006
0.38-1.36 mm/yr
ZGN
XSH
Changdu
Jinsha R.
Xianshuihe R.
Cook et al., 2018
Quimet et al., 2009
24-7200 mm/ka
Daduhe R.
Chengdu
Fu et al., 2013
Graf et al., 2008
Schäfer et al., 2002
11 - 184 ka
Henck et al., 2013
13-570 mm/ka
Yalong R.
Kangding
Bai et al., 2018
Yan et al., 2017
Chen et al., 2010
Strasky et al., 2009
Owen et al., 2005
Tschudi et al., 2003
0.3 - 27 ka
Lancang R.
Nu R.
Zhang et al., 2015
Fu et al., 2013
Xu and Zhou, 2009
Wang et al., 2006
8 - 149 ka
WMS
Gongga Mt
7556m
Zhang et al., 2018
Chen et al., 2008
0.51-4.38 mm/yr
Zhang et al., 2018
6 - 57 ka
Shangri-la
Xichang
He et al., 2015
1.05-2.36 mm/yr
Kong et al., 2009
7.32-16.51 mm/yr
Yulong Mt.
5596m
Kong et al., 2009
1 - 61 ka
Lijiang
0
200 km
Elevation (m)
High: 7556
Low: 90
Exposure age (10Be)
Burial age (OSL)
Burial age (14C)
Burial age (ESR)
Denudation rate
Incision rate
b
~50 mm/ka
Total number of 190
Number
Relative probability
Denudation rate (mm/ka)
c
~20 ka (LGM)
Total number of 342
Number
Relative probability
Exposure/burial age (ka)

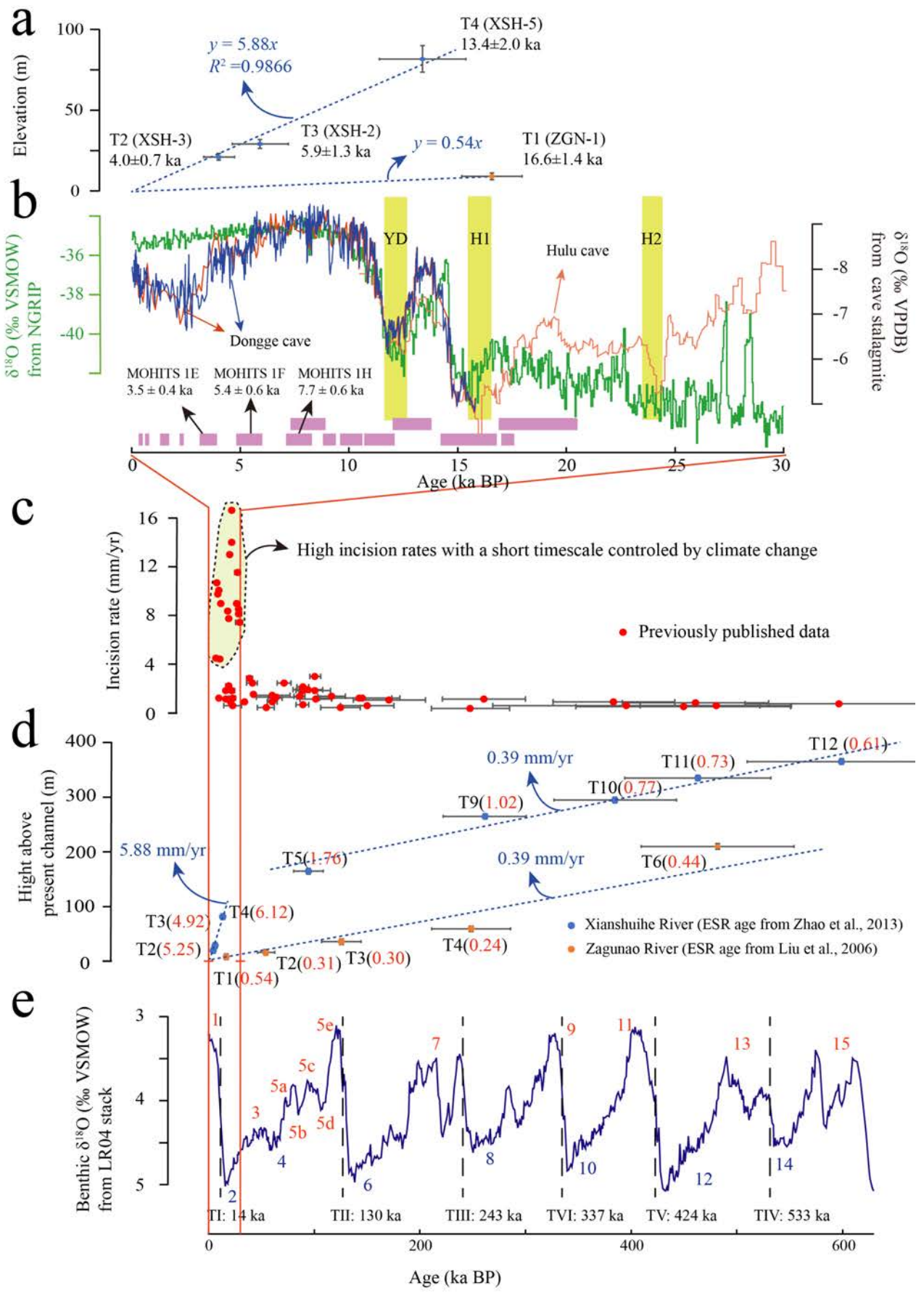
a
Elevation (m)
100
50
0
y = 5.88x
R² =0.9866
T4 (XSH-5)
13.4±2.0 ka
T2 (XSH-3)
4.0±0.7 ka
T3 (XSH-2)
5.9±1.3 ka
y = 0.54x
T1 (ZGN-1)
16.6±1.4 ka
b
δ18O (‰ VSMOW)
from NGRIP
-36
-38
-40
YD
H1
H2
Hulu cave
Dongge cave
δ18O (‰ VPDB)
from cave stalagmite
-8
-7
-6
MOHITS 1E
3.5 ± 0.4 ka
MOHITS 1F
5.4 ± 0.6 ka
MOHITS 1H
7.7 ± 0.6 ka
0
5
10
15
20
25
30
Age (ka BP)
c
Incision rate (mm/yr)
16
12
8
4
0
High incision rates with a short timescale controled by climate change
Previously published data
d
Hight above
present channel (m)
400
300
200
100
0
0.39 mm/yr
T12 (0.61)
T11(0.73)
T10(0.77)
T9(1.02)
5.88 mm/yr
T5(1.76)
0.39 mm/yr
T6(0.44)
T3(4.92)
T4(6.12)
T2(5.25)
T1(0.54)
T2(0.31)
T3(0.30)
T4(0.24)
Xianshuihe River (ESR age from Zhao et al., 2013)
Zagunao River (ESR age from Liu et al., 2006)
e
Benthic δ18O (‰ VSMOW)
from LR04 stack
3
4
5
1
2
3
4
5a
5b
5c
5d
5e
6
7
8
9
10
11
12
13
14
15
TI: 14 ka
TII: 130 ka
TIII: 243 ka
TVI: 337 ka
TV: 424 ka
TIV: 533 ka
0
200
400
600
Age (ka BP)

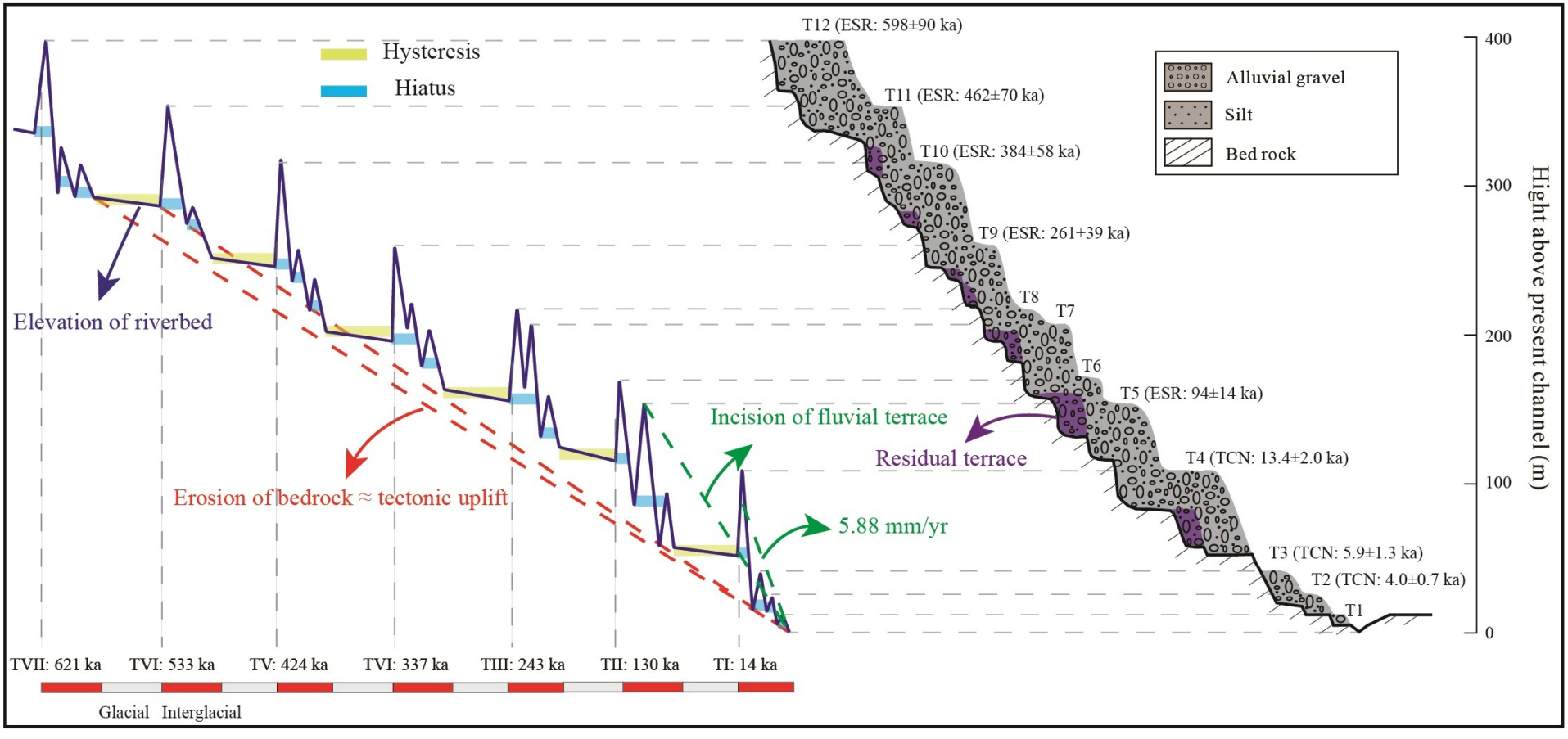
Hysteresis
Hiatus
Elevation of riverbed
Erosion of bedrock ≈ tectonic uplift
Incision of fluvial terrace
5.88 mm/yr
Residual terrace
T12 (ESR: 598±90 ka)
T11 (ESR: 462±70 ka)
T10 (ESR: 384±58 ka)
T9 (ESR: 261±39 ka)
T8
T7
T6
T5 (ESR: 94±14 ka)
T4 (TCN: 13.4±2.0 ka)
T3 (TCN: 5.9±1.3 ka)
T2 (TCN: 4.0±0.7 ka)
T1
Alluvial gravel
Silt
Bed rock
Hight above present channel (m)
400
300
200
100
0
TVII: 621 ka
TVI: 533 ka
TV: 424 ka
TVI: 337 ka
TIII: 243 ka
TII: 130 ka
TI: 14 ka
Glacial
Interglacial

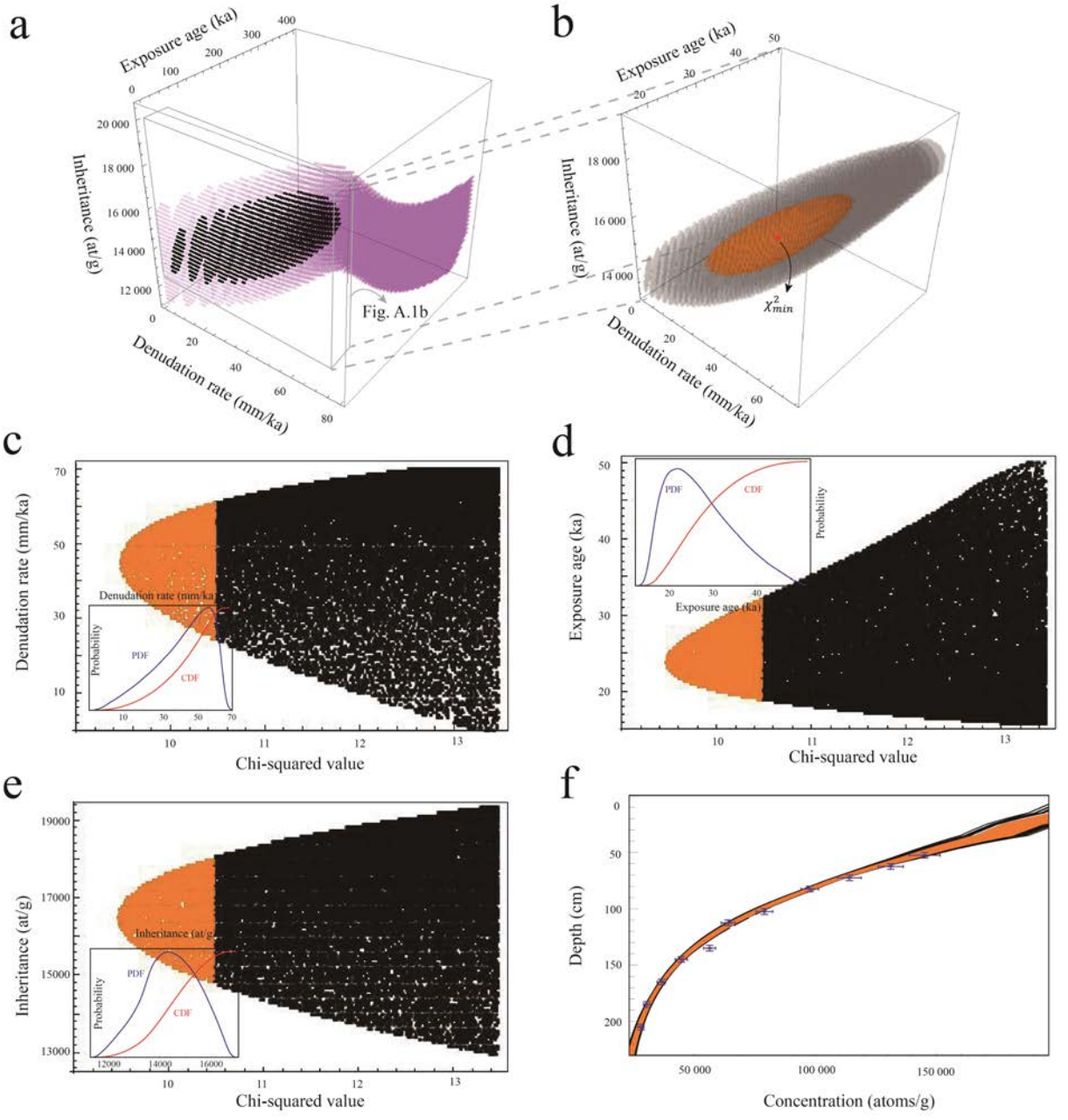
a
Exposure age (ka)
Inheritance (at/g)
Denudation rate (mm/ka)
Fig. A.1b
b
Exposure age (ka)
Inheritance (at/g)
Denudation rate (mm/ka)
χ^2_{min}
c
Denudation rate (mm/ka)
Chi-squared value
Probability
PDF
CDF
d
Exposure age (ka)
Chi-squared value
Probability
PDF
CDF
e
Inheritance (at/g)
Chi-squared value
Probability
PDF
CDF
f
Depth (cm)
Concentration (atoms/g)

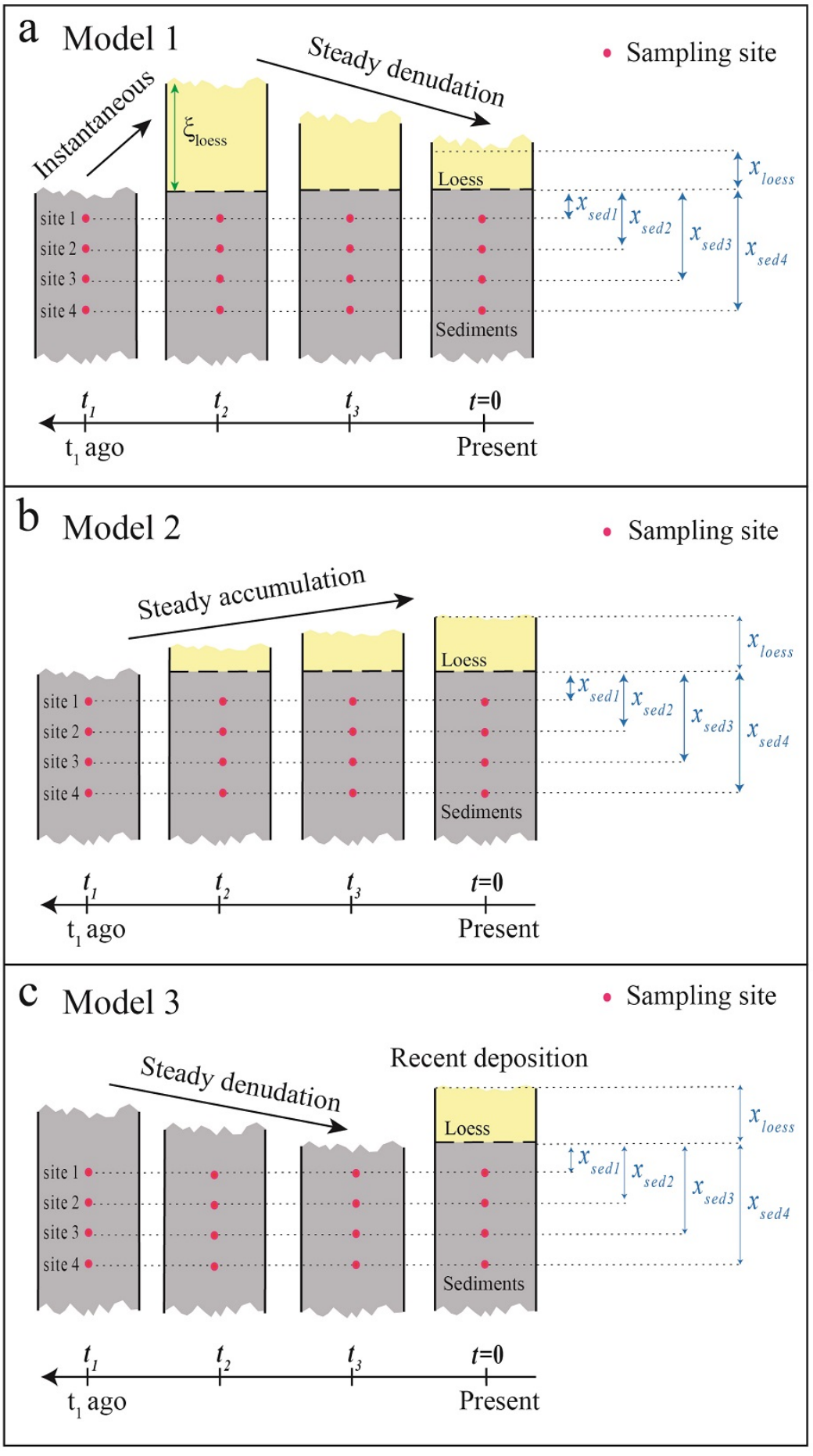
a
Model 1
Sampling site
Instantaneous
Steady denudation
ξloess
Loess
site 1
site 2
site 3
site 4
Sediments
xloess
xsed1
xsed2
xsed3
xsed4
t1
t2
t3
t=0
t1 ago
Present
b
Model 2
Sampling site
Steady accumulation
Loess
site 1
site 2
site 3
site 4
Sediments
xloess
xsed1
xsed2
xsed3
xsed4
t1
t2
t3
t=0
t1 ago
Present
c
Model 3
Sampling site
Recent deposition
Steady denudation
Loess
site 1
site 2
site 3
site 4
Sediments
xloess
xsed1
xsed2
xsed3
xsed4
t1
t2
t3
t=0
t1 ago
Present

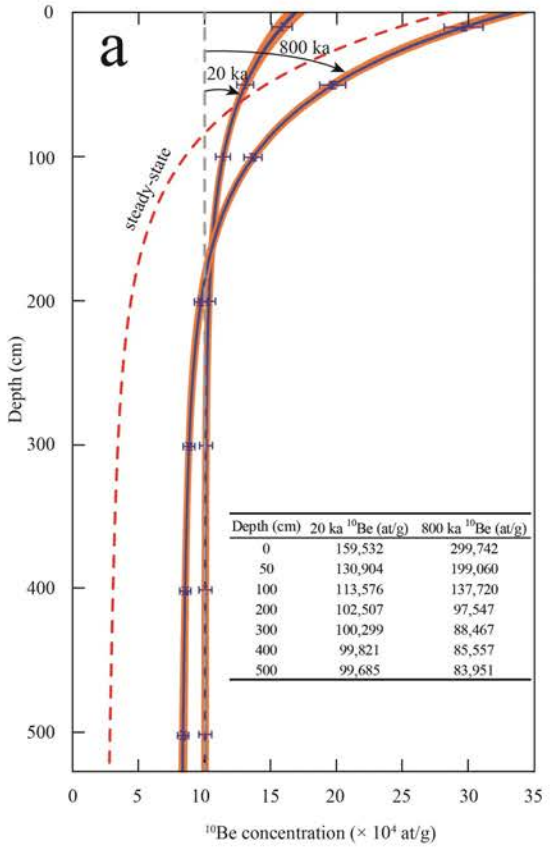

Depth (cm)	20 ka ^{10}Be (at/g)	800 ka ^{10}Be (at/g)
0	159,532	299,742
50	130,904	199,060
100	113,576	137,720
200	102,507	97,547
300	100,299	88,467
400	99,821	85,557
500	99,685	83,951

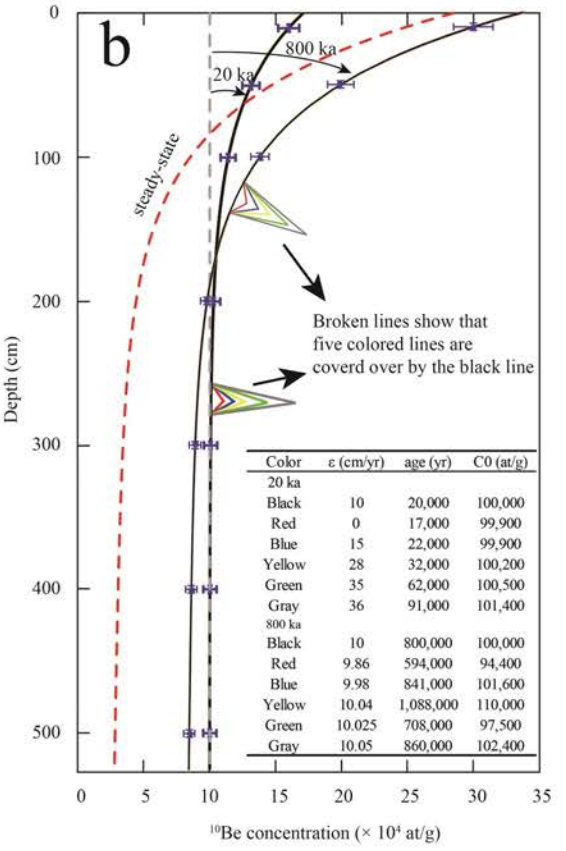

Color	ε (cm/yr)	age (yr)	C0 (at/g)
20 ka			
Black	10	20,000	100,000
Red	0	17,000	99,900
Blue	15	22,000	99,900
Yellow	28	32,000	100,200
Green	35	62,000	100,500
Gray	36	91,000	101,400
800 ka			
Black	10	800,000	100,000
Red	9.86	594,000	94,400
Blue	9.98	841,000	101,600
Yellow	10.04	1,088,000	110,000
Green	10.025	708,000	97,500
Gray	10.05	860,000	102,400

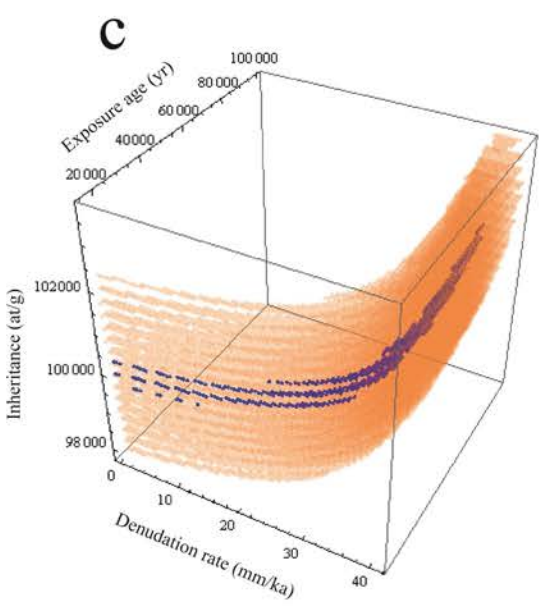

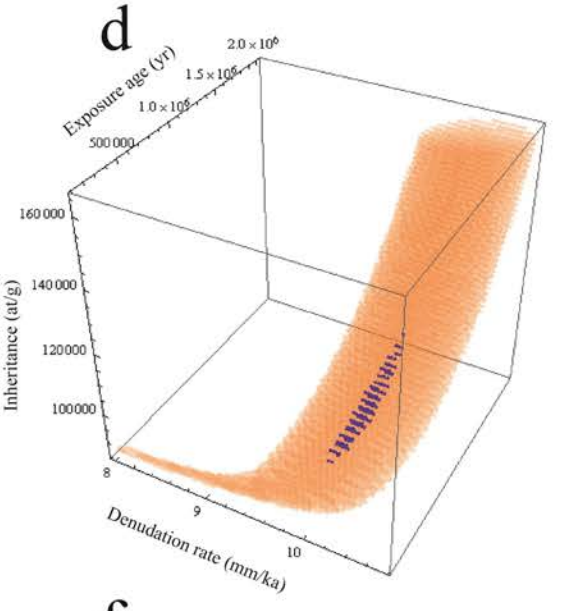

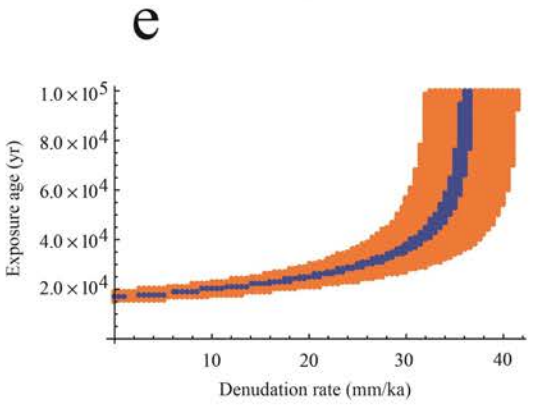

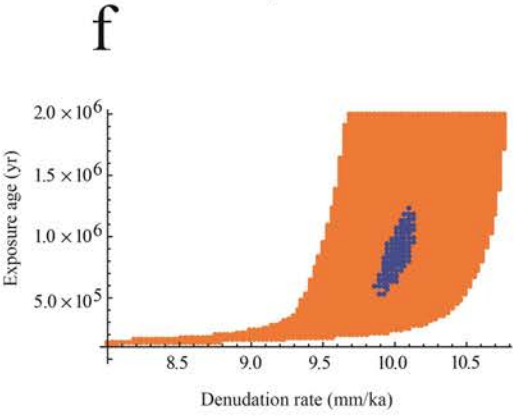

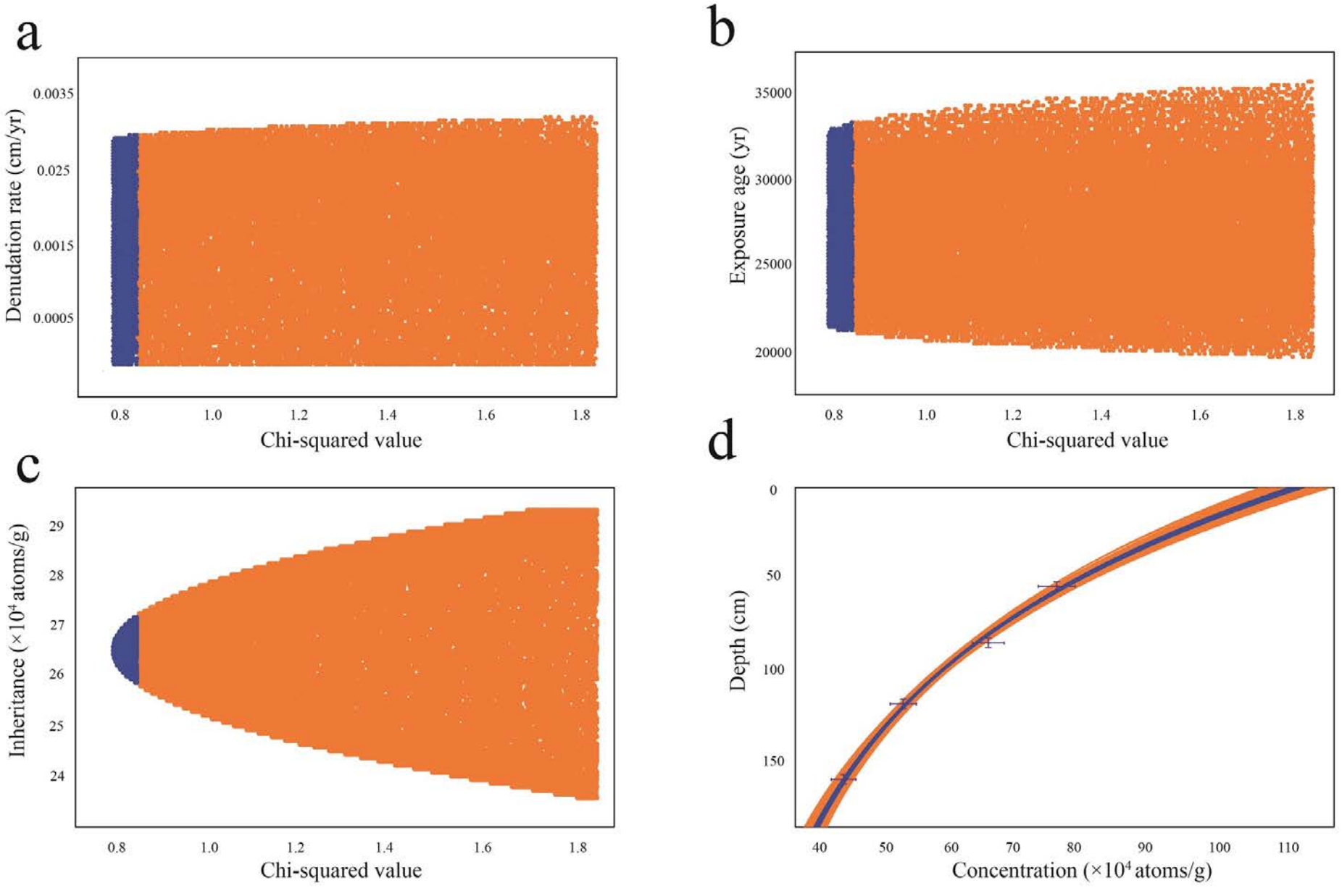
a
Denudation rate (cm/yr)
0.0035
0.025
0.0015
0.0005
0.8
1.0
1.2
1.4
1.6
1.8
Chi-squared value
b
Exposure age (yr)
35000
30000
25000
20000
0.8
1.0
1.2
1.4
1.6
1.8
Chi-squared value
c
Inheritance (×10⁴ atoms/g)
29
28
27
26
25
24
0.8
1.0
1.2
1.4
1.6
1.8
Chi-squared value
d
Depth (cm)
0
50
100
150
40
50
60
70
80
90
100
110
Concentration (×10⁴ atoms/g)

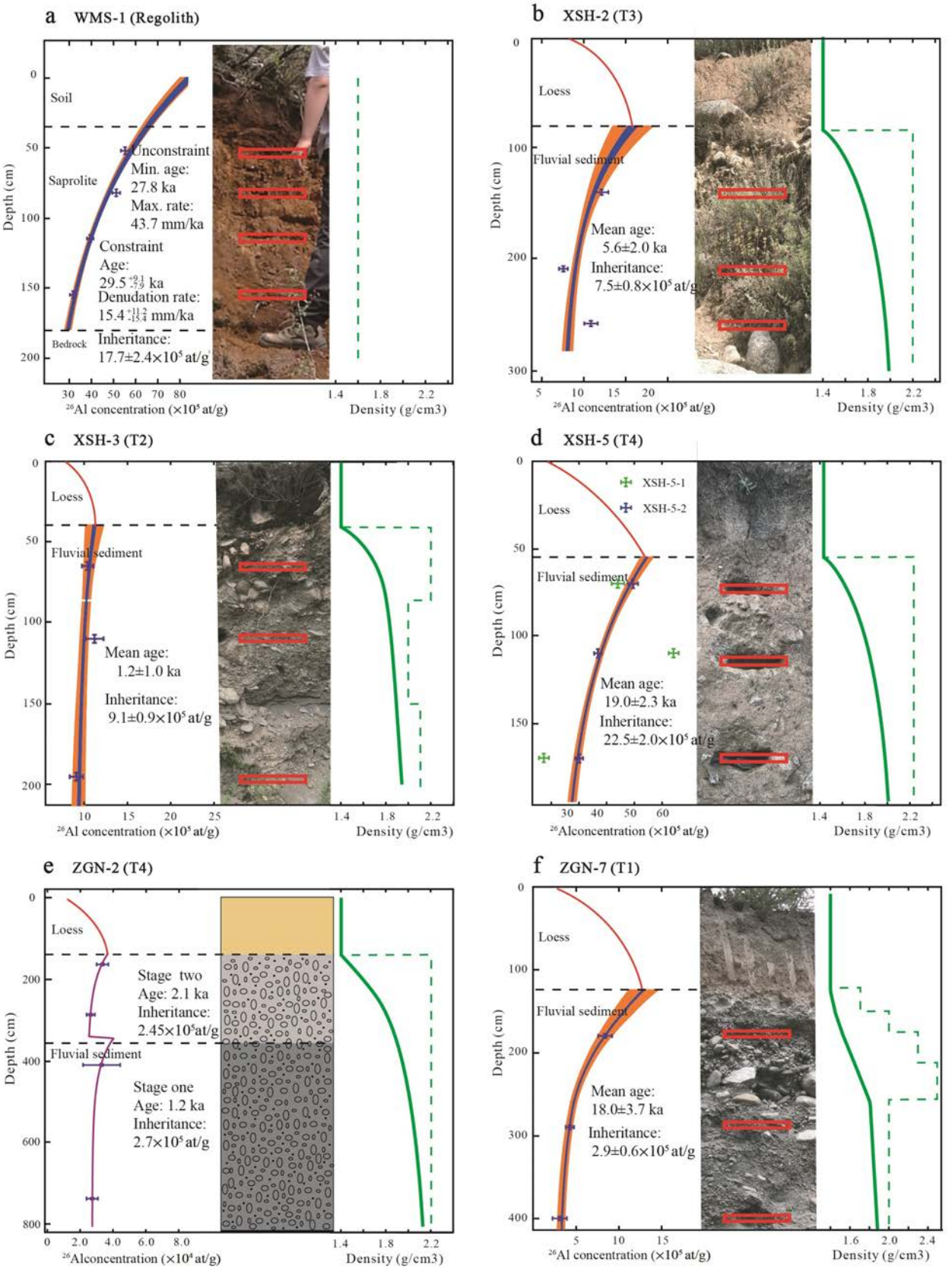
a WMS-1 (Regolith)
Soil
Saprolite
Bedrock
Unconstraint
Min. age:
27.8 ka
Max. rate:
43.7 mm/ka
Constraint
Age:
29.5 +9.1 -7.9 ka
Denudation rate:
15.4 +11.2 -15.4 mm/ka
Inheritance:
17.7±2.4×10⁵ at/g
Depth (cm)
26Al concentration (×10⁵ at/g)
Density (g/cm3)
b XSH-2 (T3)
Loess
Fluvial sediment
Mean age:
5.6±2.0 ka
Inheritance:
7.5±0.8×10⁵ at/g
c XSH-3 (T2)
Loess
Fluvial sediment
Mean age:
1.2±1.0 ka
Inheritance:
9.1±0.9×10⁵ at/g
d XSH-5 (T4)
XSH-5-1
XSH-5-2
Loess
Fluvial sediment
Mean age:
19.0±2.3 ka
Inheritance:
22.5±2.0×10⁵ at/g
e ZGN-2 (T4)
Loess
Stage two
Age: 2.1 ka
Inheritance:
2.45×10⁵at/g
Fluvial sediment
Stage one
Age: 1.2 ka
Inheritance:
2.7×10⁵ at/g
26Alconcentration (×10⁴ at/g)
f ZGN-7 (T1)
Loess
Fluvial sediment
Mean age:
18.0±3.7 ka
Inheritance:
2.9±0.6×10⁵ at/g

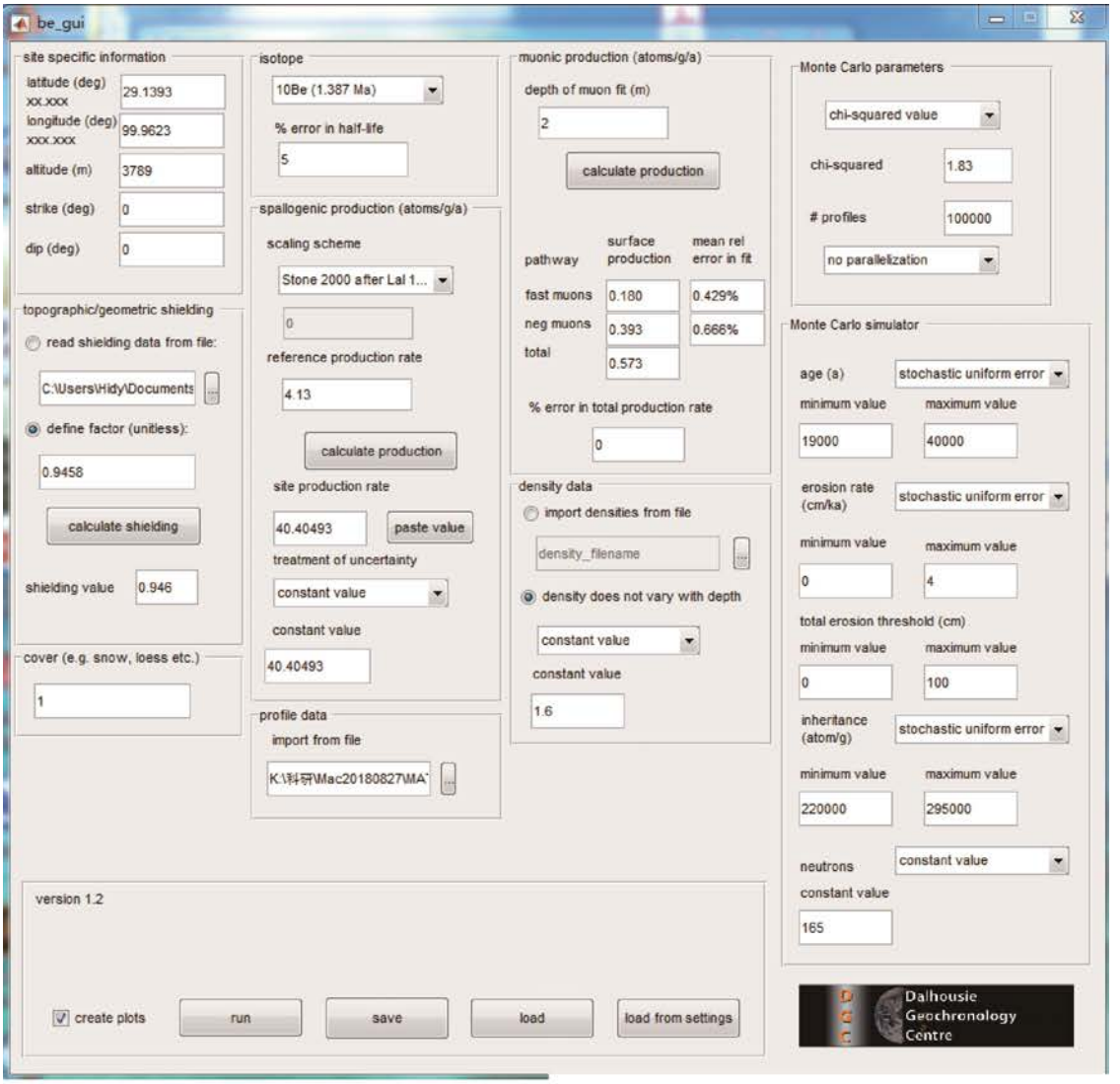

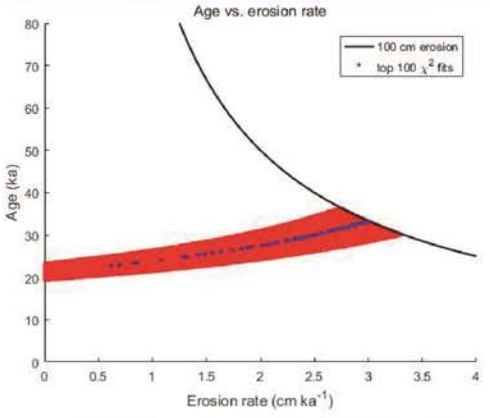

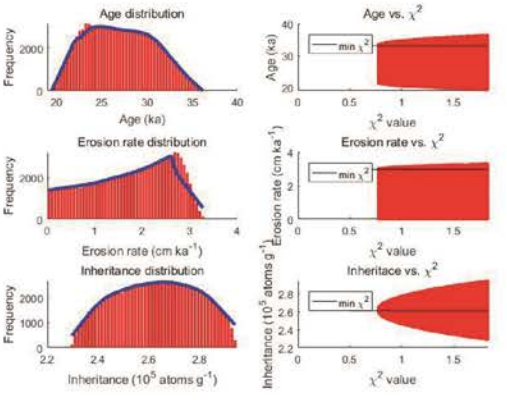

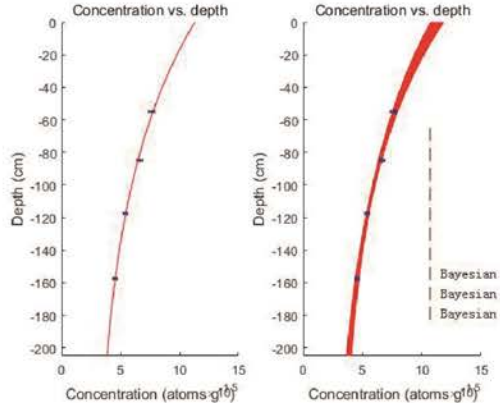

	age (ka)	inheritance (10^4 atoms g^-1)	erosion rate (cm ka^-1)
mean	27.0	26.29	1.75
median	26.9	26.32	1.87
mode	26.1	26.81	2.76
min chi^2	33.0	26.13	2.96
maximum	36.5	29.47	3.31
minimum	19.3	22.91	0.00
Bayesian most probable	24.5	26.24	2.65
Bayesian 2-sigma upper	34.8	29.27	3.07
Bayesian 2-sigma lower	20.5	22.30	0.07

Table 1. Sampling sites, scaled surface cosmogenic ^{10}Be and ^{27}Al production rates and modeled exposure ages.

Sample	Latitude (N)	Longitude (E)	Elevation (m)	River elevation (m)	Shielding factor[a]	Loess depth (cm)	$P10_{spal}$[b] (at g^{-1} a^{-1})	$P10_{slow}$[c] (at g^{-1} a^{-1})	$P10_{fast}$[c] (at g^{-1} a^{-1})	$P26_{spal}$[b] (at g^{-1} a^{-1})	$P26_{slow}$[c] (at g^{-1} a^{-1})	$P26_{fast}$[c] (at g^{-1} a^{-1})	Be age[d] (ka)	Be incision rate[e] (mm/yr)	Al age[d] (ka)	Al incision rate[e] (mm/yr)
Depth profile																
WMS1	29.1393	99.9623	3789	-	0.9458	0	39.63	0.0489	0.0777	261.3	3.4232	0.1613	>19.4	<52.8 mm/ka[f]	>27.8	<43.7 mm/ka
XSH-2	31.3470	100.7273	3152	29 ± 3	0.9945	80	30.92	0.0417	0.0734	204.0	2.9193	0.1524	5.9 ± 1.3	4.9 ± 1.1	5.6 ± 2.0	5.2 ±1.9
XSH-3	31.3468	100.7272	3144	21 ± 2	0.9945	40	30.85	0.0416	0.0733	203.5	2.9153	0.1523	4.0 ± 0.7	5.3 ± 0.9	1.2 ± 1.0	17.5 ± 14.6
XSH-5	31.3495	100.7241	3205	82 ± 8	0.9968	55	32.04	0.0426	0.0743	211.3	2.9827	0.1543	13.4 ± 2.0	6.1 ± 1.0	19.0 ± 2.3	4.3 ± 0.6
ZGN-2	31.4461	103.1700	1980	149 ± 15	0.9873	140	14.83	0.0272	0.0589	97.9	1.9060	0.1222	-	-	-	-
ZGN-7	31.4577	103.1708	1821	9 ± 1	0.9829	125	13.27	0.0255	0.0568	87.6	1.7853	0.1180	16.6 ± 1.4	0.5 ± 0.1	18.0 ± 3.7	0.5 ± 0.1
Burial samples																
XSH-4	31.3453	100.7288	3147	24 ± 3	0.9945	-	30.91	0.0417	0.0734	203.82	2.9183	0.1524	-	-	-	-
XSH-6	31.3556	100.7244	3155	7 ± 1	0.9936	-	31.03	0.0418	0.0734	204.64	2.9235	0.1525	-	-	-	-
ZGN-3	31.4451	103.1716	1916	85± 9	0.9834	-	14.15	0.0265	0.0579	93.38	1.8527	0.1202	-	-	-	-
ZGN-4	31.4487	103.1731	1894	68± 7	0.9834	-	13.94	0.0262	0.0576	92.02	1.8371	0.1197	-	-	-	-
ZGN-5	31.4516	103.1725	1859	35± 4	0.9805	-	13.58	0.0258	0.0571	89.61	1.8072	0.1186	-	-	-	-
ZGN-6	31.4524	103.1730	1833	13± 2	0.9834	-	13.38	0.0256	0.0570	88.30	1.7945	0.1183	-	-	-	-

^{10}Be spallogenic production rates (SLHL) is 4.13 atoms/(g(qtz) yr) (Martin et al., 2017). The ^{26}Al/^{10}Be spallogenic production ratio induced by the standardization used at ASTER is 6.61 ± 0.52. Slow and fast muons production rates (SLHL: 0.012 atom/(g(qtz) yr) and 0.039 atom/(g(qtz) yr) for ^{10}Be and 0.84 atom/(g(qtz) yr) and 0.081 atom/(g(qtz) yr) for ^{26}Al, respectively) are only scaled relatively to atmospheric pressure (Braucher et al., 2011).

[a] Determined by CRONUS online calculator (Balco et al., 2008).

[b] As stated by Stone (2000).

[c] According to Braucher et al. (2011).

[d] Calculated from results of model 2 (mean age).

[e] Average incision rate from formation of fluvial terrace to present.

[f] Denudation rate of Wumingshan regolith in mm/ka

Table 2. ^{10}Be and ^{26}Al cosmogenic isotope data.

Sample	Depth[a] (cm)	Density[b] (g/cm^3)	Qtz mass (g)	Total ^{9}Be (μg)	Total ^{27}Al (μg)	^{10}Be/^{9}Be[c] (10^{-14})	± (%)	[^{10}Be] (10^4 at/g)	± (%)	^{26}Al/^{27}Al[d] (10^{-14})	± (%)	[^{26}Al] (10^4 at/g)	± (%)
Wumingshan regolith													
WMS1-11	52.5	1.6	31.02	253	2300	155.06	2.9	76.06	3.5	325.78	2.8	559.97	3.4
WMS1-17	82.5	1.6	34.00	258	2534	144.83	2.8	66.13	3.5	300.74	2.7	519.40	3.4
WMS1-22	115	1.6	35.62	259	2554	122.89	2.9	53.79	3.5	240.74	3.1	400.04	3.7
WMS1-26	155	1.6	30.35	261	2221	87.23	3.4	45.13	4.0	189.52	3.8	321.46	4.3
Xianshuihe river													
XSH-2-1	60	2.2	11.86	228	1438	16.64	3.8	19.25	4.3	43.16	6.4	121.30	6.7
XSH-2-2	130	2.2	12.83	232	1514	11.16	3.9	12.11	4.4	27.76	6.6	75.88	6.9
XSH-2-3	180	2.2	12.42	238	1843	14.28	4.0	16.43	4.5	31.67	7.1	108.75	7.3
XSH-3-1	25	2.2	14.48	242	1566	17.97	3.8	18.06	4.3	41.32	6.0	103.55	6.3
XSH-3-2	70	2.1	4.61	257	1380	4.84	5.1	16.23	5.4	16.10	9.1	111.63	9.3
XSH-3-3	155	2.1	6.46	261	1382	5.00	4.6	12.14	5.0	18.24	8.2	90.43	8.5
XSH-5-1-1	15	2.2	11.80	262	2025	45.56	3.4	60.91	3.9	111.25	4.0	442.58	4.4
XSH-5-1-2	55	2.2	5.12	251	2441	15.90	4.0	46.94	4.4	57.72	3.1	638.21	3.7
XSH-5-1-3	115	2.2	14.44	253	3639	44.90	3.7	47.36	4.2	31.56	6.3	184.28	6.6
XSH-5-2-1	15	2.2	20.43	254	3468	85.43	3.4	63.80	4.0	125.68	3.1	494.49	3.7
XSH-5-2-2	55	2.2	23.02	252	3998	71.77	3.4	47.28	3.9	91.34	3.1	367.68	3.7
XSH-5-2-3	115	2.2	20.93	251	3800	58.58	3.6	42.20	4.1	71.43	4.2	300.57	4.6
XSH-4-1	~2000	2.2	22.22	252	1528	11.61	3.8	7.92	4.3	42.01	6.2	66.96	6.5
XSH-4-2	~2500	2.2	32.37	255	2838	18.24	3.7	8.66	4.2	31.58	4.0	64.15	4.5
XSH-6	~500	2.2	36.60	254	4082	42.09	3.5	17.58	4.0	51.09	4.5	132.04	4.9
Zagunao river													
ZGN-2-1	24	2.2	14.56	261	5843	4.57	6.1	4.91	6.4	3.62	10.4	33.65	10.6
ZGN-2-2	147	2.2	11.55	254	2626	2.47	7.7	3.26	8.0	5.02	9.1	26.45	9.3
ZGN-2-3	270	2.2	15.14	265	38400	4.90	6.0	5.15	6.4	0.56	34.1	33.10	34.2
ZGN-2-4	597	2.2	14.30	268	1922	3.35	5.5	3.77	5.9	8.79	12.5	27.37	12.6
ZGN-7-1	55	1.8	6.53	266	1873	4.06	5.5	9.95	5.9	12.70	9.5	84.38	9.7
ZGN-7-2	165	2.2	9.93	253	1973	2.91	6.6	4.45	6.9	9.39	11.0	43.24	11.2
ZGN-7-3	275	2.1	8.30	262	1769	1.59	9.2	3.01	9.4	6.36	26.6	31.42	26.7
ZGN-3	~2000	2.2	8.86	278	2291	2.50	6.4	4.72	6.7	4.51	10.3	27.01	10.5
ZGN-4	~2000	2.2	2.38	263	1655	0.80	13.5	5.29	13.7	2.34	23.2	37.60	23.2
ZGN-5	~1500	2.2	31.72	253	2156	2.52	6.4	1.21	6.7	7.16	12.8	11.28	13.0
ZGN-6	~1500	2.2	3.34	260	1684	0.52	20.7	2.43	20.8	1.80	24.4	21.01	24.5

Total ^{9}Be and ^{27}Al have been measured by inductively coupled plasma atomic emission spectrometry (ICP-AES) and uncertainty of 2% has been considered. ^{10}Be and ^{26}Al concentration measurements were performed at ASTER AMS (CEREGE, Aix-en-Provence, France). STD-11 and SM-A1-11 standard materials with isotope ratio ^{10}Be/^{9}Be of $(1.1911 \pm 0.013) \times 10^{-11}$ and ^{26}Al/^{27}Al of $(7.401 \pm 0.013) \times 10^{-12}$ have been used to measure ^{10}Be and ^{26}Al concentrations (Arnold et al., 2010; Braucher et al., 2015).

[a] Total depth excluding loess thickness.

[b] Average density of 1.6 g/cm^3 have been assumed for regolith according to previous data (Ackerer et al., 2016; Cui et al., 2016); integrated bulk density excluding loess (1.4 g/cm^3) for fluvial sediments.

[c] Corrected by blank ratio (6.8×10^{-15} for Wumingshan regolith and average 2.9×10^{-15} of three blank ratios for Xianshuihe and Zagunao rivers).

[d] Corrected by average blank ratio of 1.5×10^{-15} .

	χ^2_{min}*	Min.	Max.	Mean	Mode	Median
Data from Ackerer et al. (2016)	p-value = 30.4 %			$\chi^2_{min} = 9.5$		
Denudation rate (mm/ka)	44.9	0	72.0	49.4	64.8	52.8
Exposure age (ka)	23.8	15.4	54.2	28.5	22.6	27.0
Inheritance (10^4 atoms/g)	1.65	1.29	1.93	1.68	11.78	1.70
WMS1 ^{10}Be ($\varepsilon \times t < 100$ cm)	p-value = 36.3 %			$\chi^2_{min} = 0.8$		
Denudation rate (mm/ka)	-	0	32.8	17.3	27.2	18.4
Exposure age (ka)	-	19.4	36.6	27.1	23.4	27.0
Inheritance (10^4 atoms/g)	27.1	23.5	29.5	26.6	26.6	26.6
WMS1 ^{26}Al ($\varepsilon \times t < 100$ cm)	p-value = 11.5 %			$\chi^2_{min} = 6.4$		
Denudation rate (mm/ka)	-	0	26.6	14.3	22.4	15.4
Exposure age (ka)	-	23.9	44..3	33.1	28.4	32.9
Inheritance (10^4 atoms/g)	177	152	200	177	176	177
WMS1 ^{26}Al and 10Be ($\varepsilon \times t < 100$ cm)	p-value = 1.2 %			$\chi^2_{min} = 14.4$		
Denudation rate (mm/ka)	27.6	0	29.6	16.8	25.6	18.0
Exposure age (ka)	36.0	21.6	38.6	29.5	32.9	29.5
^{10}Be inheritance (10^4 atoms/g)	25.9	23.3	28.4	25.9	26.0	25.9
^{26}Al inheritance (10^4 atoms/g)	193	173	211	193	194	193

Supplementary table 1. Statistical analysis for all possible solutions in shaded area of depth profile. Depth profiles of Ackerer et al. (2016) and Wumingshan (this study).

Previous data (Ackerer et al., 2016) and Wumingshan regolith use $\chi^2_{min} + 1$ confidence level.

χ^2_{min}*: Local optimal solution is unavailable when the data is excessively scattered or when number of samples is insufficient (See details in section 4.2 and Fig. S.2).

Supplementary table 2. Statistical analysis for all possible solutions in orange shaded area of ^{10}Be depth profile.

	Model 1						Model 2						Model 3					
	χ^2_{min}*	Min.	Max.	Mean	Mode	Median	χ^2_{min}*	Min.	Max.	Mean	Mode	Median	χ^2_{min}*	Min.	Max.	Mean	Mode	Median
X-2 (T3)	p-value < 0.1 %						p-value < 0.1 %						p-value < 0.1 %					
Denudation rate (mm/ka)	-	0	27.9	11.4	17.4	11.4	-136.6	-111.4	-176.2	-138.4	-137.0	-136.7	-	0	28.2	11.5	17.7	11.4
Exposure age (ka)	-	6.5	11.2	8.7	8.2	8.6	5.9	4.5	7.2	5.9	5.9	5.9	-	3.3	5.6	4.3	4.2	4.3
Inheritance (10^4 atoms/g)	12.0	11.2	12.7	12.0	12.1	12.0	12.0	11.3	1.312.7	12.0	12.0	12.0	12.0	11.3	12.7	12.0	12.1	12.0
X-3 (T2)	p-value = 17.0 %						p-value = 17.4 %						p-value = 20.8 %					
Denudation rate (mm/ka)	-	0	45.0	19.8	33.0	19.8	-99.9	-85.9	-119.3	-100.6	-99.9	-99.9	25.4	0	31.9	14.2	24.2	14.4
Exposure age (ka)	-	4.0	6.1	5.0	5.0	5.0	4.0	3.3	4.7	4.0	4.0	4.0	3.6	2.9	4.1	3.5	3.5	3.5
Inheritance (10^4 atoms/g)	10.9	10.1	11.6	10.9	11.0	10.9	10.9	10.1	11.7	10.9	10.9	10.9	10.9	10.3	11.6	10.9	11.0	10.9
X-5 (T4)	p-value = 6.3 %						p-value = 6.3 %						p-value = 6.3 %					
Denudation rate (mm/ka)	-	0	12.5	5.5	9.2	5.6	-40.9	-35.7	47.6	-41.1	-41.0	-40.9	-	0	10.0	4.5	7.5	4.5
Exposure age (ka)	-	14.6	21.4	17.8	17.5	17.8	13.4	11.4	15.4	13.4	13.4	13.4	-	9.2	13.1	11.0	10.8	11.0
Inheritance (10^4 atoms/g)	33.6	31.2	36.0	33.7	33.8	33.7	33.6	31.1	36.1	33.6	33.6	33.6	33.5	31.1	36.0	33.6	33.9	33.6
Z-7 (T1)	p-value = 50.4 %						p-value = 44.4 %						p-value = 50.2 %					
Denudation rate (mm/ka)	-	0	6.8	3.2	5.6	3.2	-75.2	-69.6	-81.8	-75.3	-75.2	-75.2	0	0	10.1	4.7	8.3	4.7
Exposure age (ka)	-	26.7	34.9	30.6	30.7	30.6	16..6	15.2	18.0	16.6	16.6	16.6	10.2	9.3	11.8	10.5	10.4	10.5
Inheritance (10^4 atoms/g)	2.6	2.3	2.8	2.6	2.6	2.6	3.0	2.8	3.2	3.0	3.0	3.0	2.7	2.4	2.9	2.7	2.7	2.7

χ^2_{min}*: Local optimal solution is unavailable when the data is excessively scattered or when number of samples is insufficient (See detail in section 4.2 and Fig. S.2).

Supplementary table 3. Summary of published basin-wide denudation rates data.

Number	Sample	Location	Latitude (N)	Longitude (E)	Sea elevation (m)	[^{10}Be] (10^4 at/g)	± （%）	Erosion rate (mm/ka)	Error (1δ) (mm/ka)	References
1	GS01	Gongga	29.7380	102.0250	4381	27360	14170	1220	620	Cook et al., 2018
2	GS02	Gongga	29.7960	102.0600	4017	30320	15370	1000	520	Cook et al., 2018
3	GS03	Gongga	29.3810	102.0780	3277	30020	18150	670	400	Cook et al., 2018
4	GS05	Gongga	29.3870	101.9860	3900	29290	16890	950	570	Cook et al., 2018
5	GS06	Gongga	29.8910	101.9300	4721	42950	16630	970	380	Cook et al., 2018
6	GS07	Gongga	29.8880	101.9270	4721	40570	35290	1020	890	Cook et al., 2018
7	GS08	Gongga	29.9890	101.9110	4266	279700	64170	120	29	Cook et al., 2018
8	GS09	Gongga	30.2400	101.7720	4326	396300	77060	87	18	Cook et al., 2018
9	GS10	Gongga	29.9010	101.9340	4576	74390	3810	520	45	Cook et al., 2018
10	GS12	Gongga	29.9670	101.9650	4374	90390	4150	405	34	Cook et al., 2018
11	GS15	Gongga	30.2660	101.7790	4391	145850	7240	246	22	Cook et al., 2018
12	GS16	Gongga	30.2630	101.8140	4420	174150	10170	210	20	Cook et al., 2018
13	GS18	Gongga	30.2720	101.8710	4228	173740	8140	192	16	Cook et al., 2018
14	GS19	Gongga	30.1600	101.8290	4309	213870	9920	161	14	Cook et al., 2018
15	GS20	Gongga	30.1430	101.8590	4132	227350	10780	138	12	Cook et al., 2018
16	GS21	Gongga	30.0590	102.0040	4040	45790	3830	682	76	Cook et al., 2018
17	GS22	Gongga	30.0460	101.9650	4244	104120	4660	326	27	Cook et al., 2018
18	GS25	Gongga	30.5420	101.5420	4055	404850	18950	75	6	Cook et al., 2018
19	GS26	Gongga	30.5670	101.5250	4185	231830	14960	142	14	Cook et al., 2018
20	GS35	Gongga	29.8420	102.0400	4307	14420	1760	2390	340	Cook et al., 2018
21	GS37	Gongga	29.7020	102.0210	4640	4860	1520	7610	2460	Cook et al., 2018
22	GS38	Gongga	29.4160	101.9080	4469	19550	1580	1800	190	Cook et al., 2018
23	GS39	Gongga	29.4000	101.9630	3680	15240	1610	1610	210	Cook et al., 2018
24	GS40	Gongga	29.4650	102.1680	2575	5130	1030	2700	580	Cook et al., 2018
25	GS41	Gongga	29.6820	101.8960	4958	11280	1530	3560	550	Cook et al., 2018
26	wbo302	Yalong	30.2700	101.5300	3816-4316	1087600	19400	36	2	Ouimet et al., 2009
27	wbo305	Yalong	29.8900	101.5400	4207-4403	1805000	48900	24	2	Ouimet et al., 2009
28	wbo316	Yalong	29.4300	101.2300	3152-5150	196000	8500	248	23	Ouimet et al., 2009
29	wbo424	Minjiang	31.3000	103.5300	1999-4002	66500	3400	323	33	Ouimet et al., 2009
30	wbo439	Yalong	29.4100	101.2300	2894-5443	124200	5400	397	37	Ouimet et al., 2009
31	wbo444	Dadu	29.3700	102.2400	1000-2806	42400	4900	243	40	Ouimet et al., 2009
32	wbo445	Dadu	29.5000	102.1800	1173-2778	19500	1700	573	79	Ouimet et al., 2009
33	wbo448	Dadu	29.9100	102.1900	1685-5918	65800	2400	455	39	Ouimet et al., 2009
34	wbo450	Dadu	30.2300	102.1800	1740-4695	84400	3700	326	31	Ouimet et al., 2009
35	wbo501	Minjiang	31.5600	103.4900	1623-4184	89600	3600	241	22	Ouimet et al., 2009
36	wbo502	Minjiang	31.7600	102.7400	3178-4987	202300	5800	216	17	Ouimet et al., 2009
37	wbo505	Dadu	32.2100	101.6100	2765-4410	189300	10000	191	20	Ouimet et al., 2009
38	wbo506	Dadu	31.8900	100.7500	3397-4891	274300	6500	170	13	Ouimet et al., 2009
39	wbo508	Dadu	32.2000	101.0200	3277-4623	968400	16100	44	3	Ouimet et al., 2009
40	wbo510	Dadu	31.7200	100.9300	3634-4444	1024500	33400	37	3	Ouimet et al., 2009
41	wbo511	Dadu	31.7700	100.9900	3525-4671	472800	9500	97	7	Ouimet et al., 2009
42	wbo512	Dadu	31.7900	101.1000	3259-4548	370200	8300	111	8	Ouimet et al., 2009
43	wbo513	Dadu	31.7700	101.3700	3004-4781	267900	8800	168	14	Ouimet et al., 2009
44	wbo514	Dadu	31.7500	102.0000	2480-4495	211500	5300	164	12	Ouimet et al., 2009
45	wbo515	Dadu	31.4200	102.0500	2278-4164	170900	4500	156	12	Ouimet et al., 2009
46	wbo518	Dadu	30.9500	101.7200	2461-4636	127300	5000	256	23	Ouimet et al., 2009
47	wbo519	Dadu	31.0200	102.2800	2497-4218	178000	6600	154	13	Ouimet et al., 2009
48	wbo521	Dadu	30.5400	101.6200	3478-4945	142200	8100	301	32	Ouimet et al., 2009
49	wbo522	Dadu	30.6800	101.7500	2718-4881	78300	5200	489	57	Ouimet et al., 2009
50	wbo523	Dadu	30.7300	102.0000	1903-5268	27900	1800	1125	127	Ouimet et al., 2009
51	wbo524	Dadu	30.3800	102.1300	1850-5026	45800	1800	549	49	Ouimet et al., 2009

Continued

52	wbo529	Dadu	30.1000	102.0600	2408-4764	57700	3700	582	66	Ouimet et al., 2009
53	wbo530	Dadu	30.0800	102.0700	2057-5614	74300	3600	487	48	Ouimet et al., 2009
54	wbo536	Yalong	30.0400	100.9800	2745-4662	346000	14100	98	9	Ouimet et al., 2009
55	wbo538	Yalong	30.0400	101.2200	3192-4616	412200	11200	95	7	Ouimet et al., 2009
56	wbo544	Yalong	29.9800	101.5800	3455-4606	808600	20300	46	3	Ouimet et al., 2009
57	wbo545	Yalong	30.3300	101.5200	3745-4200	1581800	46300	23	2	Ouimet et al., 2009
58	wbo549	Dadu	29.6500	102.1100	1656-6865	16300	1200	3171	388	Ouimet et al., 2009
59	wbo550	Dadu	29.5400	102.1400	1340-4159	14300	1700	1177	199	Ouimet et al., 2009
60	wbo551	Dadu	29.3400	102.2500	960-4571	96500	8600	163	23	Ouimet et al., 2009
61	wbo604	Minjiang	32.0200	103.2800	2015-4646	98800	4200	286	26	Ouimet et al., 2009
62	wbo605	Minjiang	32.1300	102.8900	2549-4142	112300	3600	285	86	Ouimet et al., 2009
63	wbo607	Dadu	32.2700	102.4900	3600-4438	203000	6000	203	61	Ouimet et al., 2009
64	wbo609	Dadu	32.4200	100.8100	3493-4676	272000	6100	170	51	Ouimet et al., 2009
65	wbo610s	Dadu	32.5300	100.6700	3594-4582	455900	15000	99	30	Ouimet et al., 2009
66	wbo610q	Dadu	32.5300	100.6700	3594-4582	359600	12200	125	10	Ouimet et al., 2009
67	wbo612	Dadu	32.2200	100.3900	3817-4604	769800	30000	61	18	Ouimet et al., 2009
68	wbo613	Dadu	32.6100	101.1900	3179-4632	389800	12400	117	35	Ouimet et al., 2009
69	wbo614	Dadu	32.5800	101.0800	3307-4431	314800	10000	129	39	Ouimet et al., 2009
70	wbo616	Dadu	32.4300	101.0500	3367-4387	228100	9100	164	49	Ouimet et al., 2009
71	wbo617	Dadu	32.3400	101.2200	3507-4453	548000	14600	72	22	Ouimet et al., 2009
72	wbo618	Yalong	31.4500	100.7200	3230-4562	358300	12400	109	33	Ouimet et al., 2009
73	wbo619	Yalong	31.0300	101.0700	3034-4849	174900	6200	227	68	Ouimet et al., 2009
74	wbo621	Yalong	30.3200	101.3800	3993-4510	914200	29600	48	14	Ouimet et al., 2009
75	wbo622	Yalong	30.3100	101.4200	4061-4370	633600	13200	68	20	Ouimet et al., 2009
76	wbo623	Yalong	30.1400	101.5100	3511-4148	763700	15500	44	13	Ouimet et al., 2009
77	wbo624s	Yalong	29.7700	101.1000	2573-4762	318500	11000	108	32	Ouimet et al., 2009
78	wbo624q	Yalong	29.7700	101.1000	2573-4762	232600	6700	148	12	Ouimet et al., 2009
79	wbo625	Yalong	30.0500	101.3100	3822-4596	366000	12900	119	36	Ouimet et al., 2009
80	wbo626	Yalong	30.0600	101.3600	4253-4559	900600	19700	51	15	Ouimet et al., 2009
81	wbo633	Dadu	29.5900	102.0200	2852-5815	16700	1100	3036	358	Ouimet et al., 2009
82	wbo637	Anning	28.7700	102.2500	2178-3383	11500	1100	1447	211	Ouimet et al., 2009
83	wbo638	Yalong	28.3800	101.8800	1589-4077	52600	2200	397	36	Ouimet et al., 2009
84	wbo639	Yalong	28.6100	101.8600	1540-4550	18400	1200	1210	138	Ouimet et al., 2009
85	wbo641	Yalong	28.6100	101.6800	1983-4824	94600	4300	301	29	Ouimet et al., 2009
86	wbo642	Yalong	28.9300	101.5400	2875-4710	100200	3600	384	115	Ouimet et al., 2009
87	wbo643	Yalong	29.5100	101.4300	3379-4997	204800	7200	225	67	Ouimet et al., 2009
88	wbo644	Yalong	29.7200	101.5200	3407-4690	756300	22100	56	17	Ouimet et al., 2009
89	wbo645	Yalong	29.9300	101.3900	3597-4565	1418700	24500	29	9	Ouimet et al., 2009
90	wbo647	Dadu	29.6800	102.2000	1284-3583	31200	1600	477	49	Ouimet et al., 2009
91	wbo651	Dadu	31.2900	102.0500	2221-4420	267600	7500	116	9	Ouimet et al., 2009
92	wbo653	Dadu	31.0300	101.8700	2046-5094	99100	4800	364	36	Ouimet et al., 2009
93	06-3R-52-SAL	Lancang	29.7800	96.7100	5074	277111	14909	220	30	Henck et al., 2011
94	06-3R-53-SAL	Lancang	29.7800	96.7100	5075	111701	7259	550	90	Henck et al., 2011
95	06-3R-50-SAL	Lancang	30.0400	97.1500	4973	105850	5784	550	80	Henck et al., 2011
96	06-3R-49-SAL	Lancang	30.1100	97.1900	4873	231103	10285	240	30	Henck et al., 2011
97	06-3R-48-SAL	Lancang	30.1000	97.2100	4770	784949	20449	70	8	Henck et al., 2011
98	06-3R-46-SAL	Lancang	30.1000	97.3000	4351	367464	15764	120	16	Henck et al., 2011
99	06-3R-30-SAL	Lancang	30.6000	97.0700	4784	2078252	62058	26	3	Henck et al., 2011
100	06-3R-32-SAL	Lancang	30.2000	97.3200	4766	2120444	58616	25	3	Henck et al., 2011
101	06-3R-33-SAL	Lancang	29.8500	97.6900	4801	1553608	50391	34	4	Henck et al., 2011
102	06-3R-34-SAL	Lancang	29.7400	97.7600	4714	1092820	26768	48	5	Henck et al., 2011
103	06-3R-35-SAL	Lancang	29.6800	97.8300	4694	1237683	50806	41	6	Henck et al., 2011
104	06-3R-36-SAL	Lancang	29.6700	97.8500	4708	1772162	37815	29	3	Henck et al., 2011

Continued

105	05-3R-9-SAL	Lancang	28.0200	98.6300	4748	518500	12296	110	11	Henck et al., 2011
106	05-3R-10-SAL	Lancang	27.5800	98.7900	4739	427659	11859	130	15	Henck et al., 2011
107	05-3R-11a-SAL	Lancang	27.2300	98.8900	2018	161438	7129	80	10	Henck et al., 2011
108	05-3R-11b-SAL	Lancang	27.2300	98.8900	4733	532386	18243	100	13	Henck et al., 2011
109	05-3R-11b-SAL	Lancang	27.2300	98.8900	4733	591943	14123	90	10	Henck et al., 2011
110	05-3R-12-SAL	Lancang	26.4800	98.9000	4720	402267	15524	130	17	Henck et al., 2011
111	05-3R-13b-SAL	Lancang	25.8500	98.8600	4706	294362	12158	180	20	Henck et al., 2011
112	06-3R-26-MEK	Lancang	31.1500	97.1600	4642	296760	10966	170	20	Henck et al., 2011
113	06-3R-26-MEK	Lancang	31.1500	97.1600	4642	317841	9684	180	20	Henck et al., 2011
114	06-3R-27-MEK	Lancang	31.1500	97.1800	4550	375523	13219	140	17	Henck et al., 2011
115	06-3R-27-MEK	Lancang	31.1500	97.1800	4550	432965	12691	120	14	Henck et al., 2011
116	06-3R-28-MEK	Lancang	30.8500	97.3400	4569	399126	18332	130	18	Henck et al., 2011
117	06-3R-29-MEK	Lancang	30.7700	97.3400	4638	678376	26294	80	10	Henck et al., 2011
118	06-3R-38-MEK	Lancang	29.6200	98.3500	4544	352113	10049	140	17	Henck et al., 2011
119	06-3R-39-MEK	Lancang	29.6600	98.3700	4077	344713	14531	110	15	Henck et al., 2011
120	06-3R-43-MEK	Lancang	29.5500	98.2100	4550	2768030	67592	17	2	Henck et al., 2011
121	05-3R-4-MEK	Lancang	28.5600	98.8100	4152	70117	5195	570	100	Henck et al., 2011
122	05-3R-6-MEK	Lancang	28.1000	98.9200	4507	308766	17071	160	20	Henck et al., 2011
123	05-3R-7-MEK	Lancang	27.5700	99.0400	4485	295439	12621	170	20	Henck et al., 2011
124	05-3R-8-MEK	Lancang	27.3500	99.0900	4473	352419	10543	140	16	Henck et al., 2011
125	05-3R-14a-MEK	Lancang	25.4300	99.2900	4288	261412	14464	170	30	Henck et al., 2011
126	06-3R-15-YANG	Lancang	31.7600	98.5600	4384	360619	11421	130	16	Henck et al., 2011
127	06-3R-16-YANG	Lancang	31.6400	98.5900	4352	384297	13299	120	15	Henck et al., 2011
128	06-3R-17-YANG	Lancang	31.6300	98.5900	4744	4215088	94795	13	1	Henck et al., 2011
129	06-3R-17-YANG	Lancang	31.6300	98.5900	4744	4063015	59101	14	1	Henck et al., 2011
130	06-3R-21-YANG	Lancang	31.4000	98.1600	4327	949300	36916	48	6	Henck et al., 2011
131	06-3R-20-YANG	Lancang	31.5900	98.3700	4317	948113	30610	48	6	Henck et al., 2011
132	06-3R-19b-YANG	Lancang	31.6500	98.3700	4337	924199	20444	49	5	Henck et al., 2011
133	06-3R-19a-YANG	Lancang	31.6500	98.3700	4333	651735	29344	70	10	Henck et al., 2011
134	06-3R-18-YANG	Lancang	31.6200	98.6000	4142	360839	26401	120	21	Henck et al., 2011
135	06-3R-22-YANG	Lancang	31.3000	98.0000	4327	782810	33147	58	8	Henck et al., 2011
136	06-3R-24-YANG	Lancang	31.4000	97.8800	4681	881427	39199	60	8	Henck et al., 2011
137	06-3R-41-YANG	Lancang	29.7600	99.0000	4695	3262761	97513	17	2	Henck et al., 2011
138	06-3R-42-YANG	Lancang	29.7600	99.0100	4253	984334	38432	43	6	Henck et al., 2011
139	05-3R-3-YANG	Lancang	28.2200	99.3200	4651	2814015	45255	19	2	Henck et al., 2011
140	05-3R-1b-YANG	Lancang	26.8700	99.9700	4605	2661264	52493	20	2	Henck et al., 2011
141	NH-KE-04-2	Yellow River	34.1000	100.7610	3700	125766	2845	56	4	Harkins et al., 2007
142	NH-KE-04-3	Yellow River	34.8980	100.8850	3850	634156	3135	59	5	Harkins et al., 2007
143	NH-KE-04-4A	Yellow River	34.7990	100.8110	3810	707902	4107	83	6	Harkins et al., 2007
144	NH-KE-04-4B	Yellow River	34.7970	100.8110	3810	426520	2237	81	6	Harkins et al., 2007
145	NH-KCB-05-1	Yellow River	34.7770	100.8130	4010	439792	13786	84	7	Harkins et al., 2007
146	NH-KCB-05-3	Yellow River	34.5620	100.3970	4320	545990	80426	85	17	Harkins et al., 2007
147	NH-KCB-05-2	Yellow River	34.7520	99.6930	4900	448257	16764	107	9	Harkins et al., 2007
148	NH-KCB-05-6	Yellow River	33.6930	101.3880	3610	567528	21790	70	6	Harkins et al., 2007
149	KE-04-2	Yellow River	35.0969	100.7618	3502-3778	634157	14849	57.81	4.88	Kirby 2013
150	KE-04-3	Yellow River	34.8979	100.8850	3783-4097	707902	11393	53.73	4.46	Kirby 2013
151	KE-04-4a	Yellow River	34.7993	100.8108	3476-3892	426521	8828	79.07	6.56	Kirby 2013
152	KE-05-1	Yellow River	34.7767	100.8134	3397-4011	430129	13786	80.69	6.99	Kirby 2013
153	KE-05-2	Yellow River	34.7523	99.6930	3752-4728	448257	16764	100.2	8.99	Kirby 2013
154	KE-05-3	Yellow River	34.5270	100.3000	3829-4547	545990	80462	11.64	0.02	Kirby 2013
155	KE-05-6	Yellow River	33.6932	101.3878	3559-4355	567528	21790	64.69	5.80	Kirby 2013
156	NHKCB06-1	Yellow River	34.5976	101.3413	3455-4344	631165	25623	55.87	5.07	Kirby 2013
157	NHKCB06-2	Yellow River	33.7648	101.2257	3605-4630	516597	16856	77.41	6.78	Kirby 2013

Continued

158	NHKCB06-3	Yellow River	33.7237	101.2713	3597-4678	622602	34544	66.28	6.55	Kirby 2013
159	NHKCB06-4	Yellow River	34.5566	99.4807	4506-5084	910600	34614	61.64	5.62	Kirby 2013
160	NHKCB06-5	Yellow River	34.4791	99.7782	4082-4870	461097	18586	106.23	9.69	Kirby 2013
161	NHKCB06-6	Yellow River	34.6886	100.6226	3078-4537	154030	7239	227.91	21.13	Kirby 2013
162	LM253	Minjiang	31.0620	103.4840*	3554	44900	8750	640	190	Godard et al., 2010
163	LM254	Minjiang	31.0663	103.4903*	3492	60340	8560	450	110	Godard et al., 2010
164	LM259	Minjiang	31.5034	103.5675*	3622	43250	12550	680	260	Godard et al., 2010
165	LM261	Minjiang	31.4976	103.6304*	3524	27070	13560	1010	600	Godard et al., 2010
166	LM263	Minjiang	31.3795	103.5172*	3531	61070	12600	450	140	Godard et al., 2010
167	SC004	Minjiang	30.7526	103.4493*	1942	61910	15590	180	60	Godard et al., 2010
168	SC016	Minjiang	31.2511	103.7897*	2695	78240	35070	230	120	Godard et al., 2010
169	SC031	Minjiang	31.3809	104.0157*	2938	28690	7220	720	250	Godard et al., 2010
170	SC033	Minjiang	31.3162	104.0088*	1427	39280	10960	200	70	Godard et al., 2010
171	SC049	Minjiang	31.6971	103.8507*	3558	75530	11870	370	90	Godard et al., 2010
172	SC059	Minjiang	31.0641	103.4965*	1556	26190	5910	320	100	Godard et al., 2010
173	SC071	Minjiang	31.5058	104.1259*	2294	56690	13120	250	80	Godard et al., 2010
174	SC082	Minjiang	31.0620	103.4840*	3556	48880	9190	590	170	Godard et al., 2010
175	SC086	Minjiang	31.0663	103.4903*	3492	50170	15200	540	220	Godard et al., 2010
176	SP20	Heishui	32.1100	102.8600	3552 – 4420	44710	4340	670	90	Ansberque et al., 2015
177	SP19	Heishui	32.1900	102.6500	4103 – 4669	93990	5210	420	48	Ansberque et al., 2015
178	SP18	Dadu	32.2700	102.5000	3999 – 4429	199630	19580	190	26	Ansberque et al., 2015
179	SP17	Yellow	32.6100	102.3300	3668 – 4058	645020	28660	50	5	Ansberque et al., 2015
180	SP16	Yellow	32.6800	102.3500	3706 – 4055	781290	25180	40	4	Ansberque et al., 2015
181	SP15	Yellow	32.9700	102.6300	3718 – 3955	548610	17470	60	6	Ansberque et al., 2015
182	SP14	Yellow	33.0300	102.6000	3686 – 4042	479820	15210	70	7	Ansberque et al., 2015
183	SP13	Yellow	33.0400	102.9000	3853 – 4202	368120	12480	100	10	Ansberque et al., 2015
184	SP12	Yellow	32.9300	103.2800	3883 – 4106	786940	39020	50	5	Ansberque et al., 2015
185	SP11	Minjiang	32.9200	103.4000	3840 – 4265	251140	11000	140	15	Ansberque et al., 2015
186	SP10	Minjiang	32.9200	103.4000	3733 – 4117	169250	6310	200	21	Ansberque et al., 2015
187	SP09	Minjiang	32.8900	103.4600	3666 – 4087	192970	6290	170	17	Ansberque et al., 2015
188	SP08	Minjiang	32.8500	103.5600	3591 – 4144	154450	21200	200	34	Ansberque et al., 2015
189	SP07	Minjiang	32.6800	103.6000	3445 – 4280	85990	10700	330	52	Ansberque et al., 2015
190	SP06	Minjiang	32.600	103.6100	3558 – 4476	124600	4030	240	26	Ansberque et al., 2015
191	SP05	Minjiang	32.5800	103.6200	3685 – 4315	156010	9380	210	24	Ansberque et al., 2015
192	SP04	Minjiang	32.3300	103.7200	3512 – 4657	54010	5290	550	77	Ansberque et al., 2015
193	SP03	Minjiang	32.2600	103.7500	3489 – 4687	84970	3440	340	37	Ansberque et al., 2015
194	SP02	Minjiang	32.2200	103.7700	3324 – 4031	65930	2670	400	43	Ansberque et al., 2015
195	SP01	Minjiang	32.1200	103.7400	3348 – 4303	47820	2840	560	65	Ansberque et al., 2015
196	Ma02	Minjiang	32.3400	103.6300	3360 – 4123	101630	6310	270	30	Ansberque et al., 2015
197	Ma03	Minjiang	32.3400	103.5500	3455 – 4397	128070	8330	220	30	Ansberque et al., 2015
198	Ma04	Minjiang	32.3800	103.5100	3527 – 4117	203170	10860	150	20	Ansberque et al., 2015
199	Ma05	Minjiang	32.3800	103.4700	3540 – 4369	137870	10010	220	30	Ansberque et al., 2015
200	Ma06	Minjiang	32.7200	103.2400	3716 – 4248	109670	9080	300	40	Ansberque et al., 2015
201	Ma07	Heishui	32.1000	102.7500	3830 – 5049	91580	6210	380	50	Ansberque et al., 2015
202	Ma09	Heishui	32.1000	102.7500	3794 – 4669	115140	7530	300	40	Ansberque et al., 2015
203	HS01	Heishui	32.0700	103.1200	3467 – 4582	82840	7080	350	50	Ansberque et al., 2015
204	HS03	Heishui	32.1800	103.1900	3430 – 4422	108540	7440	260	30	Ansberque et al., 2015
205	HS04	Heishui	32.2900	103.2800	3653 – 4426	139970	7780	230	30	Ansberque et al., 2015
206	HS05	Heishui	32.3200	103.2900	3573 – 4282	246210	11720	120	10	Ansberque et al., 2015
207	HS06	Heishui	32.0600	103.2600	3188 – 4087	156770	7950	160	20	Ansberque et al., 2015
208	HS07	Heishui	31.8600	103.2800	3383 – 4315	93533	5920	300	40	Ansberque et al., 2015

* Sampling locations are derived from the geological map in the references.

Supplementary table 4. Summary of published exposure/burial ages data**.**

Number	Sample	Type	Location	Method	Latitude (N)	Longitude (E)	Sea elevation (m)	Exposure age (ka)	Error (ka)	References
1	ZDG-1	Moraine	Zhuqing	10Be	32.1100	98.8513	4144	14.0	1.3	Chevalier et al., 2017
2	ZDG-2	Moraine	Zhuqing	10Be	32.1104	98.8513	4138	14.9	1.4	Chevalier et al., 2017
3	ZDG-3	Moraine	Zhuqing	10Be	32.1122	98.8510	4111	17.4	1.5	Chevalier et al., 2017
4	ZDG-4	Moraine	Zhuqing	10Be	32.1121	98.8511	4110	19.5	1.7	Chevalier et al., 2017
5	ZDG-5	Moraine	Zhuqing	10Be	32.1146	98.8512	4060	20.7	1.8	Chevalier et al., 2017
6	ZDG-6	Moraine	Zhuqing	10Be	32.1150	98.8520	4049	22.5	2.0	Chevalier et al., 2017
7	ZDG-7	Moraine	Zhuqing	10Be	32.1145	98.8524	4050	17.9	1.6	Chevalier et al., 2017
8	ZDG-8	Moraine	Zhuqing	10Be	32.1177	98.8520	4038	19.3	1.8	Chevalier et al., 2017
9	ZDG-9	Moraine	Zhuqing	10Be	32.1184	98.8523	4037	21.6	1.9	Chevalier et al., 2017
10	ZDG-10	Moraine	Zhuqing	10Be	32.1193	98.8528	4036	15.0	1.4	Chevalier et al., 2017
11	GZ-1	Moraine	Ganzi	10Be	31.7285	99.5791	4037	47.9	4.1	Chevalier et al., 2017
12	GZ-2	Moraine	Ganzi	10Be	31.7284	99.5791	4037	30.6	2.6	Chevalier et al., 2017
13	GZ-3	Moraine	Ganzi	10Be	31.7286	99.5779	4046	22.9	2.0	Chevalier et al., 2017
14	GZ-4	Moraine	Ganzi	10Be	31.7287	99.5774	4050	92.6	8.1	Chevalier et al., 2017
15	GZ-5	Moraine	Ganzi	10Be	31.7287	99.5764	4059	8.6	0.8	Chevalier et al., 2017
16	GZ-6	Moraine	Ganzi	10Be	31.7286	99.5759	4064	12.8	1.1	Chevalier et al., 2017
17	GZ-7	Moraine	Ganzi	10Be	31.7288	99.5738	4086	61.9	5.4	Chevalier et al., 2017
18	GZ-8	Moraine	Ganzi	10Be	31.7311	99.5806	3998	63.0	5.5	Chevalier et al., 2017
19	GZ-10B	Moraine	Ganzi	10Be	31.7320	99.5818	3981	47.5	4.2	Chevalier et al., 2017
20	GZ-11	Moraine	Ganzi	10Be	31.7316	99.5812	3992	94.1	8.4	Chevalier et al., 2017
21	GZ-12	Moraine	Ganzi	10Be	31.7313	99.5807	3999	74.8	6.7	Chevalier et al., 2017
22	GZ-13	Moraine	Ganzi	10Be	31.7315	99.5812	3993	38.0	3.3	Chevalier et al., 2017
23	MGT-2	Depth profile	Mangangong	10Be	31.9641	99.1356	3992	19.0	2.3	Chevalier et al., 2017
24	TG-1	Moraine	Kangding	10Be	30.3097	101.6669	4500	15.5	1.5	Bai et al., 2018
25	TG-2	Moraine	Kangding	10Be	30.3096	101.6667	4498	11.1	1.1	Bai et al., 2018
26	TG-3	Moraine	Kangding	10Be	30.3096	101.6665	4499	10.1	1.0	Bai et al., 2018
27	TG-4	Moraine	Kangding	10Be	30.3096	101.6665	4499	12.2	1.2	Bai et al., 2018
28	TG-5	Moraine	Kangding	10Be	30.3087	101.6649	4447	14.5	1.4	Bai et al., 2018
29	TG-6	Moraine	Kangding	10Be	30.3087	101.6647	4443	12.4	1.2	Bai et al., 2018
30	TG-7	Moraine	Kangding	10Be	30.3088	101.6646	4441	10.3	1.0	Bai et al., 2018
31	TG-8	Moraine	Kangding	10Be	30.3086	101.6640	4435	13.0	1.2	Bai et al., 2018
32	TG-9	Moraine	Kangding	10Be	30.3086	101.6635	4427	14.4	1.4	Bai et al., 2018
33	SLH-1	Moraine	Kangding	10Be	30.2451	101.7174	4271	20.3	1.9	Bai et al., 2018
34	SLH-2	Moraine	Kangding	10Be	30.2446	101.7176	4265	18.0	1.7	Bai et al., 2018
35	SLH-3	Moraine	Kangding	10Be	30.2442	101.7168	4242	18.5	1.8	Bai et al., 2018
36	SLH-4	Moraine	Kangding	10Be	30.2435	101.7162	4241	17.0	1.6	Bai et al., 2018
37	SLH-5	Moraine	Kangding	10Be	30.2425	101.7161	4234	17.9	1.7	Bai et al., 2018
38	SLH-6	Moraine	Kangding	10Be	30.2407	101.7163	4231	18.8	1.8	Bai et al., 2018
39	SLH-7	Moraine	Kangding	10Be	30.2392	101.7153	4229	21.2	2.0	Bai et al., 2018
40	SLH-8	Moraine	Kangding	10Be	30.2390	101.7146	4223	22.3	2.1	Bai et al., 2018
41	SLH-9	Moraine	Kangding	10Be	30.2386	101.7137	4224	20.3	1.9	Bai et al., 2018
42	SLH-10	Moraine	Kangding	10Be	30.2385	101.7124	4224	26.8	2.6	Bai et al., 2018
43	YJG-1	Moraine	Kangding	10Be	30.0512	101.9288	3502	17.7	1.7	Bai et al., 2018
44	YJG-2	Moraine	Kangding	10Be	30.0507	101.9283	3514	9.8	1.0	Bai et al., 2018
45	YJG-3	Moraine	Kangding	10Be	30.0503	101.9280	3521	10.4	1.0	Bai et al., 2018
46	YJG-4	Moraine	Kangding	10Be	30.0491	101.9265	3562	10.7	1.2	Bai et al., 2018
47	YJG-5	Moraine	Kangding	10Be	30.0535	101.9296	3475	18.4	1.8	Bai et al., 2018
48	YJG-6	Moraine	Kangding	10Be	30.0537	101.9296	3477	8.8	0.9	Bai et al., 2018
49	YJG-7	Moraine	Kangding	10Be	30.0548	101.9297	3475	10.9	1.1	Bai et al., 2018
50	YJG-8	Moraine	Kangding	10Be	30.0561	101.9300	3458	8.0	0.8	Bai et al., 2018
51	YJG-9	Moraine	Kangding	10Be	30.0543	101.9297	3475	16.2	1.5	Bai et al., 2018

Continued

52	15-8-30-(1)	Fluvial terrance	Deqin	10Be	28.8079	98.6559	2335	56.8	5.9	Zhang et al., 2018
53	15-8-30-(2)	Fluvial terrance	Deqin	10Be	28.8079	98.6559	2335	46.1	4.7	Zhang et al., 2018
54	15-6-2-(1)	Fluvial terrance	Deqin	10Be	28.4519	98.8293	2244	46.4	4.8	Zhang et al., 2018
55	15-6-2-(5)	Fluvial terrance	Deqin	10Be	28.4487	98.8322	2102	17.1	1.7	Zhang et al., 2018
56	15-6-3-(2)	Fluvial terrance	Deqin	10Be	28.3605	98.8672	2022	6.0	6.1	Zhang et al., 2018
57	X8	Granitoid	Daocheng	10Be	29.3200	100.0850	4310	123.3	12.3	Xu et al., 2004
58	X9	Granitoid	Daocheng	10Be	29.3200	100.0850	4310	121.8	12.1	Xu et al., 2004
59	X6	Granitoid	Daocheng	10Be	29.5558	100.2981	4279	18.5	1.9	Xu et al., 2004
60	KAN101	erratic boulders	Kangding	10Be	30.0714	101.8244	4069	16.3	0.7	Strasky et al., 2009
61	KAN102	erratic boulders	Kangding	10Be	30.0639	101.8353	4061	13.7	0.5	Strasky et al., 2009
62	KAN103	erratic boulders	Kangding	10Be	30.0653	101.8328	4071	14.9	0.6	Strasky et al., 2009
63	KAN104	erratic boulders	Kangding	10Be	30.0631	101.8319	4058	14.6	0.7	Strasky et al., 2009
64	KAN105	erratic boulders	Kangding	10Be	30.0606	101.8283	3993	13.4	0.6	Strasky et al., 2009
65	KAN1	erratic boulders	Kangding	10Be	30.0833	101.8333	4240	12.9	1.1	Tschudi et al., 2003
66	KAN2	erratic boulders	Kangding	10Be	30.0833	101.8333	4260	11.0	0.9	Tschudi et al., 2003
67	S16	Granitoid	Daocheng	10Be	29.3739	100.1371	4510	16.9	1.6	Zhang et al., 2015
68	S17	Granitoid	Daocheng	10Be	29.3739	100.1371	4510	15.9	1.5	Zhang et al., 2015
69	S18	Granitoid	Daocheng	10Be	29.3739	100.1371	4510	15.1	1.4	Zhang et al., 2015
70	S6	Granitoid	Daocheng	10Be	29.3739	100.1371	4500	14.9	1.3	Zhang et al., 2015
71	X3	Moraine	Daocheng	10Be	29.1604	100.1987	4302	18.7	1.7	Zhang et al., 2015
72	X2	Moraine	Daocheng	10Be	29.1576	100.1935	4262	24.7	2.2	Zhang et al., 2015
73	X1	Moraine	Daocheng	10Be	29.1558	100.1891	4203	45.2	3.9	Zhang et al., 2015
74	DC	Moraine	Daocheng	10Be	29.1356	100.2194	4011	37.1	3.4	Zhang et al., 2015
75	TB-08-10	Moraine	Daocheng	10Be	29.1242	100.2216	3871	40.3	3.7	Fu et al., 2013
76	TB-08-18	Moraine	Daocheng	10Be	29.1255	100.2224	3892	149.2	13.5	Fu et al., 2013
77	TB-09-119	Moraine	Daocheng	10Be	29.1285	100.2181	3919	121.3	10.8	Fu et al., 2013
78	TB-09-121	Moraine	Daocheng	10Be	29.1295	100.2182	3929	135.3	13.1	Fu et al., 2013
79	TB-09-120	Moraine	Daocheng	10Be	29.1291	100.2181	3924	150.7	14.2	Fu et al., 2013
80	TB-08-34	Moraine	Daocheng	10Be	29.1190	100.2099	3867	85.7	7.8	Fu et al., 2013
81	TB-08-33	Moraine	Daocheng	10Be	29.1189	100.2096	3864	96.4	8.6	Fu et al., 2013
82	TB-08-32	Moraine	Daocheng	10Be	29.1188	100.2095	3864	106.9	9.6	Fu et al., 2013
83	TB-08-24	Moraine	Daocheng	10Be	29.1236	100.2120	3931	50.6	4.6	Fu et al., 2013
84	TB-08-23	Moraine	Daocheng	10Be	29.1234	100.2119	3928	54.7	5.1	Fu et al., 2013
85	TB-08-22	Moraine	Daocheng	10Be	29.1229	100.2115	3916	117.2	10.9	Fu et al., 2013
86	TB-08-19	Moraine	Daocheng	10Be	29.1235	100.2096	3904	105.7	9.3	Fu et al., 2013
87	TB-08-20	Moraine	Daocheng	10Be	29.1230	100.2091	3904	112.4	10.2	Fu et al., 2013
88	TB-08-21	Moraine	Daocheng	10Be	29.1226	100.2088	3904	123.8	11.7	Fu et al., 2013
89	TB-08-27	Moraine	Daocheng	10Be	29.1753	100.1068	4056	80.5	7.7	Fu et al., 2013
90	TB-08-26	Moraine	Daocheng	10Be	29.1746	100.1077	4067	81.5	8.9	Fu et al., 2013
91	TB-08-28	Moraine	Daocheng	10Be	29.1754	100.1066	4053	116.2	10.5	Fu et al., 2013
92	TB-08-31	Moraine	Daocheng	10Be	29.1778	100.0952	4064	25.5	2.3	Fu et al., 2013
93	TB-08-30	Moraine	Daocheng	10Be	29.1777	100.0952	4062	57.3	5.2	Fu et al., 2013
94	TB-08-29	Moraine	Daocheng	10Be	29.1777	100.0953	4062	95.9	8.7	Fu et al., 2013
95	TB-08-03	Moraine	Daocheng	10Be	29.2090	100.0930	4231	51.4	4.8	Fu et al., 2013
96	TB-08-02	Moraine	Daocheng	10Be	29.2090	100.0930	4215	82.6	7.8	Fu et al., 2013
97	TB-08-01	Moraine	Daocheng	10Be	29.2067	100.0906	4216	102.3	10	Fu et al., 2013
98	TB-09-100	Moraine	Daocheng	10Be	29.3903	99.9908	4506	8.1	0.8	Fu et al., 2013
99	TB-09-102	Moraine	Daocheng	10Be	29.4025	99.9922	4512	68.1	6.1	Fu et al., 2013
100	TB-09-101	Moraine	Daocheng	10Be	29.3974	99.9939	4499	156	14.1	Fu et al., 2013
101	TB-09-14	Moraine	Daocheng	10Be	29.4188	100.0223	4446	15.2	1.4	Fu et al., 2013
102	TB-09-15	Moraine	Daocheng	10Be	29.4118	100.0208	4424	15.3	1.4	Fu et al., 2013
103	TB-09-12	Moraine	Daocheng	10Be	29.4185	100.0178	4424	16.0	1.5	Fu et al., 2013
104	TB-09-13	Moraine	Daocheng	10Be	29.4189	100.0176	4431	17.1	1.6	Fu et al., 2013

Continued

105	TB-09-114	Moraine	Daocheng	10Be	29.4266	100.0889	4459	12.9	1.2	Fu et al., 2013
106	TB-09-112	Moraine	Daocheng	10Be	29.4266	100.0886	4461	13.0	1.2	Fu et al., 2013
107	TB-09-128	Moraine	Daocheng	10Be	29.8653	99.9272	4504	24.6	2.3	Fu et al., 2013
108	TB-09-129	Moraine	Daocheng	10Be	29.8608	99.9320	4485	92.3	8.3	Fu et al., 2013
109	TB-09-130	Moraine	Daocheng	10Be	29.8538	99.9372	4440	131.2	11.8	Fu et al., 2013
110	TB-09-79	Moraine	Daocheng	10Be	29.8461	99.9657	4455	97.6	8.6	Fu et al., 2013
111	TB-09-77	Moraine	Daocheng	10Be	29.8476	99.9651	4444	102.6	9.6	Fu et al., 2013
112	TB-09-78	Moraine	Daocheng	10Be	29.8466	99.9654	4450	106.7	10.1	Fu et al., 2013
113	TB-09-74	Moraine	Daocheng	10Be	29.8574	99.9531	4339	17.1	1.6	Fu et al., 2013
114	TB-09-75	Moraine	Daocheng	10Be	29.8567	99.9531	4313	20.2	1.8	Fu et al., 2013
115	TB-09-76	Moraine	Daocheng	10Be	29.8566	99.9532	4311	21.6	2.0	Fu et al., 2013
116	TB-09-64	Moraine	Daocheng	10Be	31.0325	99.7082	4379	104.9	9.7	Fu et al., 2013
117	TB-09-65	Moraine	Daocheng	10Be	31.0323	99.7083	4373	123.1	11.1	Fu et al., 2013
118	TB-09-63	Moraine	Daocheng	10Be	31.0311	99.7082	4369	128.7	11.6	Fu et al., 2013
119	TB-09-62	Moraine	Daocheng	10Be	31.0313	99.7083	4371	135	12.1	Fu et al., 2013
120	TB-09-56	Moraine	Daocheng	10Be	31.0264	99.7241	4258	124.8	11.2	Fu et al., 2013
121	TB-09-57	Moraine	Daocheng	10Be	31.0260	99.7237	4250	126	11.4	Fu et al., 2013
122	TB-09-58	Moraine	Daocheng	10Be	31.0239	99.7214	4233	88.1	7.9	Fu et al., 2013
123	TB-09-04	Moraine	Daocheng	10Be	30.8676	99.6377	4063	120.1	10.6	Fu et al., 2013
124	TB-09-02	Moraine	Daocheng	10Be	30.8682	99.6430	4043	155.1	14.4	Fu et al., 2013
125	TB-09-03	Moraine	Daocheng	10Be	30.8684	99.6430	4036	183.6	17.0	Fu et al., 2013
126	TB-09-20	Moraine	Daocheng	10Be	30.1871	99.7731	4241	59	5.4	Fu et al., 2013
127	Lit 3	Moraine	Litang	10Be	30.2833	99.5333	4560	13.7	1.4	Schäfer et al., 2002
128	Lit 4a	Moraine	Litang	10Be	30.2833	99.5333	4560	17.7	2.0	Schäfer et al., 2002
129	Lit 4bc	Moraine	Litang	10Be	30.2833	99.5333	4560	14.8	1.7	Schäfer et al., 2002
130	Lit 5a	Moraine	Litang	10Be	30.2833	99.5333	4610	15.1	1.6	Schäfer et al., 2002
131	Lit 5b	Moraine	Litang	10Be	30.2833	99.5333	4610	15.0	1.5	Schäfer et al., 2002
132	Lit 6	Moraine	Litang	10Be	30.2833	99.5333	4570	15.3	1.4	Schäfer et al., 2002
133	Lit 7	Moraine	Litang	10Be	30.2833	99.5333	4480	13.1	1.4	Schäfer et al., 2002
134	GS5	Moraine	Gongga	10Be	29.5744	102.0095	3010	0.31	0.09	Owen et al., 2005
135	GS6	Moraine	Gongga	10Be	29.5750	102.0093	2988	2.4	0.90	Owen et al., 2005
136	GS7	Moraine	Gongga	10Be	29.5727	102.0093	2979	0.37	0.04	Owen et al., 2005
137	GS1	Moraine	Gongga	10Be	29.5720	101.9870	3174	0.86	0.11	Owen et al., 2005
138	GS2	Moraine	Gongga	10Be	29.5720	101.9870	3160	1.33	0.17	Owen et al., 2005
139	GS3	Moraine	Gongga	10Be	29.5818	102.0061	3056	0.72	0.10	Owen et al., 2005
140	GS4	Moraine	Gongga	10Be	29.5818	102.0061	3056	2.42	0.41	Owen et al., 2005
141	GS8	Moraine	Gongga	10Be	29.5835	102.0052	2972	0.66	0.31	Owen et al., 2005
142	GS9	Moraine	Gongga	10Be	29.5836	102.0051	2959	0.85	0.09	Owen et al., 2005
143	GS10	Moraine	Gongga	10Be	29.6900	102.0832	2043	6.25	0.52	Owen et al., 2005
144	GS11	Moraine	Gongga	10Be	29.6898	102.0833	2110	3.46	0.45	Owen et al., 2005
145	GS12	Moraine	Gongga	10Be	29.6899	102.0838	2039	5.6	0.46	Owen et al., 2005
146	GS13	Moraine	Gongga	10Be	29.6904	102.0849	2045	3.27	0.43	Owen et al., 2005
147	GS14	Moraine	Gongga	10Be	29.5707	102.0302	1670	6.27	0.47	Owen et al., 2005
148	GS15	Moraine	Gongga	10Be	29.5910	102.0241	1670	3.65	0.56	Owen et al., 2005
149	GS17	Moraine	Gongga	10Be	29.6203	102.1058	1858	9.15	0.50	Owen et al., 2005
150	GS19	Moraine	Gongga	10Be	29.6196	102.1081	1864	8.43	0.56	Owen et al., 2005
151	GS20	Moraine	Gongga	10Be	29.6196	102.1085	1884	7.94	0.68	Owen et al., 2005
152	GS19R	Moraine	Gongga	10Be	29.6196	102.1081	1864	7.99	0.64	Owen et al., 2005
153	GS20R	Moraine	Gongga	10Be	29.6192	102.1085	1884	7.57	0.73	Owen et al., 2005
154	TSO-2	Moraine	Daocheng	10Be	31.0867	99.7550	4138	20.1	1.0	Graf et al. (2008)
155	TSO-3	Moraine	Daocheng	10Be	31.0867	99.7550	4138	19.7	0.8	Graf et al. (2008)
156	TSO-4	Moraine	Daocheng	10Be	31.0867	99.7567	4150	19.1	1.0	Graf et al. (2008)
157	TSO-5	Moraine	Daocheng	10Be	31.0883	99.7550	4150	16.8	0.7	Graf et al. (2008)

Continued

158	TSO-6	Moraine	Daocheng	10Be	31.0883	99.7550	4150	18.0	0.7	Graf et al. (2008)
159	TSO-1	Moraine	Daocheng	10Be	31.0900	99.7517	4175	20.4	1.0	Graf et al. (2008)
160	TSO-8	Moraine	Daocheng	10Be	31.0900	99.7583	4161	16.8	0.7	Graf et al. (2008)
161	TSO-7	Moraine	Daocheng	10Be	31.0900	99.7600	4156	18.5	0.9	Graf et al. (2008)
162	TSO-7	Moraine	Daocheng	10Be	31.0900	99.7600	4156	17.0	0.8	Graf et al. (2008)
163	TSO-9	Moraine	Daocheng	10Be	31.0933	99.7583	4172	20.8	0.8	Graf et al. (2008)
164	HAI-1	Moraine	Ganzi	10Be	31.2317	99.8533	4453	42.7	1.7	Graf et al. (2008)
165	HAI-2	Moraine	Ganzi	10Be	31.2317	99.8533	4453	32.1	1.8	Graf et al. (2008)
166	HAI-5	Moraine	Ganzi	10Be	31.2800	99.8800	4370	14.5	1.0	Graf et al. (2008)
167	HAI-6	Moraine	Ganzi	10Be	31.2800	99.8800	4370	14.3	0.6	Graf et al. (2008)
168	HAI-3	Moraine	Ganzi	10Be	31.3383	99.9183	4224	15.0	0.7	Graf et al. (2008)
169	HAI-4	Moraine	Ganzi	10Be	31.3383	99.9183	4224	14.9	0.9	Graf et al. (2008)
170	HAI-7	Moraine	Ganzi	10Be	31.3800	99.9300	4169	21.9	1.1	Graf et al. (2008)
171	HAI-8	Moraine	Ganzi	10Be	31.3833	99.9200	4081	10.7	0.6	Graf et al. (2008)
172	TB-07-34	Moraine	Bayan Har	10Be	33.8759	97.2314	4493	10.980	1.083	Heyman et al. (2011)
173	TB-07-31	Moraine	Bayan Har	10Be	33.8768	97.2316	4500	43.393	3.787	Heyman et al. (2011)
174	TB-07-32	Moraine	Bayan Har	10Be	33.8769	97.2316	4501	57.762	5.045	Heyman et al. (2011)
175	TB-07-33	Moraine	Bayan Har	10Be	33.8770	97.2314	4498	39.998	3.483	Heyman et al. (2011)
176	TB-07-38	Moraine	Bayan Har	10Be	33.9618	97.3270	4536	14.445	1.340	Heyman et al. (2011)
177	TB-07-39	Moraine	Bayan Har	10Be	33.9644	97.3256	4556	110.513	9.946	Heyman et al. (2011)
178	TB-07-40	Moraine	Bayan Har	10Be	33.9644	97.3256	4557	128.661	11.630	Heyman et al. (2011)
179	TB-07-41	Moraine	Bayan Har	10Be	33.9648	97.3253	4560	88.5	7.8	Heyman et al. (2011)
180	TB-05-050	Moraine	Bayan Har	10Be	33.9862	97.4484	4576	18.5	1.7	Heyman et al. (2011)
181	TB-05-049	Moraine	Bayan Har	10Be	33.9867	97.4491	4573	11.5	1.0	Heyman et al. (2011)
182	TB-07-29	Moraine	Bayan Har	10Be	33.9879	97.4485	4574	59.2	5.3	Heyman et al. (2011)
183	TB-05-048	Moraine	Bayan Har	10Be	33.9893	97.4492	4576	13.6	1.4	Heyman et al. (2011)
184	TB-06-07	Moraine	Bayan Har	10Be	33.9896	97.4297	4590	17.9	1.6	Heyman et al. (2011)
185	TB-06-05	Moraine	Bayan Har	10Be	33.9919	97.4305	4593	34.7	3.3	Heyman et al. (2011)
186	TB-07-30	Moraine	Bayan Har	10Be	33.9919	97.4305	4589	69.9	6.6	Heyman et al. (2011)
187	TB-05-051	Moraine	Bayan Har	10Be	34.1082	97.6459	4780	30.4	2.7	Heyman et al. (2011)
188	TB-07-68	Moraine	Bayan Har	10Be	34.1232	97.5969	4723	6.4	0.6	Heyman et al. (2011)
189	TB-07-69	Moraine	Bayan Har	10Be	34.1234	97.5966	4722	3.1	0.4	Heyman et al. (2011)
190	TB-07-67	Moraine	Bayan Har	10Be	34.1237	97.5974	4724	44.3	3.8	Heyman et al. (2011)
191	TB-06-46	Moraine	Bayan Har	10Be	34.1535	98.0190	4573	41.8	3.7	Heyman et al. (2011)
192	TB-06-47	Moraine	Bayan Har	10Be	34.1554	98.0202	4583	49.0	4.4	Heyman et al. (2011)
193	TB-07-22	Moraine	Bayan Har	10Be	34.1558	97.7084	4655	43.6	3.8	Heyman et al. (2011)
194	TB-07-23	Moraine	Bayan Har	10Be	34.1560	97.7086	4657	20.1	1.9	Heyman et al. (2011)
195	TB-07-25	Moraine	Bayan Har	10Be	34.1561	97.7085	4657	29.6	2.8	Heyman et al. (2011)
196	TB-07-24	Moraine	Bayan Har	10Be	34.1561	97.7084	4656	21.2	1.9	Heyman et al. (2011)
197	TB-06-48	Moraine	Bayan Har	10Be	34.1570	98.0203	4592	79.9	7.2	Heyman et al. (2011)
198	TB-07-117	Moraine	Bayan Har	10Be	34.1640	98.1318	4648	32.6	2.8	Heyman et al. (2011)
199	TB-07-120	Moraine	Bayan Har	10Be	34.1642	98.1318	4646	43.1	3.7	Heyman et al. (2011)
200	TB-07-118	Moraine	Bayan Har	10Be	34.1643	98.1315	4646	25.5	2.2	Heyman et al. (2011)
201	TB-07-119	Moraine	Bayan Har	10Be	34.1655	98.1230	4638	59.8	5.2	Heyman et al. (2011)
202	TB-05-018	Moraine	Bayan Har	10Be	34.2685	97.8584	4716	46.5	4.1	Heyman et al. (2011)
203	TB-05-019	Moraine	Bayan Har	10Be	34.2688	97.8654	4683	92.3	8.3	Heyman et al. (2011)
204	TB-07-92	Moraine	Bayan Har	10Be	34.3371	97.6070	4557	52.1	4.5	Heyman et al. (2011)
205	TB-07-95	Moraine	Bayan Har	10Be	34.3373	97.6059	4556	12.6	1.1	Heyman et al. (2011)
206	TB-07-93	Moraine	Bayan Har	10Be	34.3373	97.6061	4546	44.8	3.9	Heyman et al. (2011)
207	TB-07-94	Moraine	Bayan Har	10Be	34.3382	97.6062	4553	46.8	4.0	Heyman et al. (2011)
208	TB-06-27	Moraine	Bayan Har	10Be	34.3898	97.7629	4518	57.7	5.9	Heyman et al. (2011)
209	TB-06-25	Moraine	Bayan Har	10Be	34.3911	97.7628	4516	57.4	5.6	Heyman et al. (2011)
210	TB-06-26	Moraine	Bayan Har	10Be	34.3915	97.7596	4509	23.6	2.3	Heyman et al. (2011)

Continued

211	TB-07-90	Moraine	Bayan Har	10Be	34.3924	97.7608	4512	42.5	3.7	Heyman et al. (2011)
212	TB-06-31	Moraine	Bayan Har	10Be	34.5116	97.7408	4456	45.5	4.0	Heyman et al. (2011)
213	TB-06-33	Moraine	Bayan Har	10Be	34.5127	97.7416	4453	19.8	1.9	Heyman et al. (2011)
214	TB-06-32	Moraine	Bayan Har	10Be	34.5134	97.7407	4451	94.7	8.7	Heyman et al. (2011)
215	TB-06-17	Moraine	Bayan Har	10Be	34.5258	97.9875	4332	51.1	4.8	Heyman et al. (2011)
216	TB-07-13	Moraine	Bayan Har	10Be	34.5261	97.9869	4331	35.0	3.4	Heyman et al. (2011)
217	TB-06-16	Moraine	Bayan Har	10Be	34.5264	97.9872	4332	40.7	3.5	Heyman et al. (2011)
218	TB-07-12	Moraine	Bayan Har	10Be	34.5961	97.9863	4266	30.8	2.9	Heyman et al. (2011)
219	TB-06-02	Moraine	Bayan Har	10Be	34.5965	97.9869	4264	60.7	5.4	Heyman et al. (2011)
220	TB-06-01	Moraine	Bayan Har	10Be	34.5991	97.9846	4259	47.3	4.4	Heyman et al. (2011)
221	TB-06-37	Moraine	Bayan Har	10Be	34.5992	97.9946	4256	34.8	3.3	Heyman et al. (2011)
222	TB-07-125	Moraine	Bayan Har	10Be	34.6049	98.0151	4248	59.5	5.5	Heyman et al. (2011)
223	YN-50	Moraine	Yulong	10Be	27.0380	100.0973	2210	18.9	1.2	Kong et al., 2009
224	YN-48	Moraine	Yulong	10Be	27.0383	100.1137	2440	1.27	0.14	Kong et al., 2009
225	YN-64	Moraine	Yulong	10Be	27.0523	100.2555	2930	8.71	0.61	Kong et al., 2009
226	YN-65	Moraine	Yulong	10Be	27.0530	100.2543	2960	11.3	0.8	Kong et al., 2009
227	YN-52	Moraine	Yulong	10Be	27.1153	100.0800	2240	49.6	3.4	Kong et al., 2009
228	YN-53	Moraine	Yulong	10Be	27.1153	100.0800	2240	61.1	3.8	Kong et al., 2009
229	YN-54	Moraine	Yulong	10Be	27.1158	100.0793	2250	38.2	2.7	Kong et al., 2009
230	YN-55	Moraine	Yulong	10Be	27.1158	100.0793	2250	57.0	3.6	Kong et al., 2009
231	YN-56	Moraine	Yulong	10Be	27.1158	100.0793	2250	48.6	3.2	Kong et al., 2009
232	YN-62	Moraine	Yulong	10Be	27.1217	100.2547	3070	11.9	1.0	Kong et al., 2009
233	YN-63	Moraine	Yulong	10Be	27.1218	100.2543	3060	10.1	0.9	Kong et al., 2009
234	N15	Moraine	Nianbaoyeze	10Be	33.3566	101.0987	4048	38.46	0.92	Owen et al., 2003
235	N14	Moraine	Nianbaoyeze	10Be	33.3572	101.0984	4046	16.60	0.57	Owen et al., 2003
236	N13	Moraine	Nianbaoyeze	10Be	33.3580	101.0974	4055	33.31	0.80	Owen et al., 2003
237	N12	Moraine	Nianbaoyeze	10Be	33.3582	101.0970	4048	16.12	0.40	Owen et al., 2003
238	N11	Moraine	Nianbaoyeze	10Be	33.3582	101.0969	4057	16.79	0.44	Owen et al., 2003
239	N17	Moraine	Nianbaoyeze	10Be	33.3993	101.2363	4214	42.24	1.09	Owen et al., 2003
240	N18	Moraine	Nianbaoyeze	10Be	33.3994	101.2367	4217	18.69	0.45	Owen et al., 2003
241	N16	Moraine	Nianbaoyeze	10Be	33.3994	101.2362	4212	41.39	0.99	Owen et al., 2003
242	N20	Moraine	Nianbaoyeze	10Be	33.3995	101.2367	4216	26.99	0.92	Owen et al., 2003
243	N19	Moraine	Nianbaoyeze	10Be	33.3999	101.2376	4204	27.14	0.92	Owen et al., 2003
244	N1	Moraine	Nianbaoyeze	10Be	33.4006	101.2452	4235	41.96	1.57	Owen et al., 2003
245	N2	Moraine	Nianbaoyeze	10Be	33.4025	101.2450	4227	29.35	0.70	Owen et al., 2003
246	N10	Moraine	Nianbaoyeze	10Be	33.4029	101.1045	4045	20.66	0.55	Owen et al., 2003
247	N9	Moraine	Nianbaoyeze	10Be	33.4030	101.1045	4045	14.71	0.59	Owen et al., 2003
248	N3	Moraine	Nianbaoyeze	10Be	33.4030	101.2456	4230	29.44	1.00	Owen et al., 2003
249	N8	Moraine	Nianbaoyeze	10Be	33.4034	101.1052	4043	20.06	0.6	Owen et al., 2003
250	N6	Moraine	Nianbaoyeze	10Be	33.4034	101.1054	4053	20.89	0.5	Owen et al., 2003
251	N7	Moraine	Nianbaoyeze	10Be	33.4034	101.1054	4047	19.23	0.49	Owen et al., 2003
252	N4	Moraine	Nianbaoyeze	10Be	33.4036	101.2452	4232	36.64	0.87	Owen et al., 2003
253	N5	Moraine	Nianbaoyeze	10Be	33.4039	101.2456	4233	25.53	0.62	Owen et al., 2003
254	N24	Moraine	Nianbaoyeze	10Be	33.4419	101.0982	4085	30.92	0.97	Owen et al., 2003
255	N25	Moraine	Nianbaoyeze	10Be	33.4423	101.0981	4086	25.76	0.57	Owen et al., 2003
256	N26	Moraine	Nianbaoyeze	10Be	33.4427	101.0991	4099	18.41	0.59	Owen et al., 2003
257	N27	Moraine	Nianbaoyeze	10Be	33.4437	101.0986	4101	50.35	1.17	Owen et al., 2003
258	N28	Moraine	Nianbaoyeze	10Be	33.4478	101.0958	4113	55.83	1.69	Owen et al., 2003
259	N22	Moraine	Nianbaoyeze	10Be	33.4581	101.0770	3974	19.60	0.51	Owen et al., 2003
260	N23	Moraine	Nianbaoyeze	10Be	33.4583	101.0771	3965	38.35	0.99	Owen et al., 2003
261	N21	Moraine	Nianbaoyeze	10Be	33.4585	101.0764	4017	70.25	3.00	Owen et al., 2003
262	X14	Moraine	Haizi Shan	10Be	29.1247	100.2218	3890	123.55	22.95	Wang et al., 2006
263	X14a	Moraine	Haizi Shan	10Be	29.1247	100.2218	3890	123.55	22.95	Wang et al., 2006

Continued

264	X14b	Moraine	Haizi Shan	10Be	29.1247	100.2218	3890	123.55	22.95	Wang et al., 2006
265	YPGG001	Moraine	Quershan	OSL	32.1105	98.8537	3950	16.6	1.3	Xu et al., 2010
266	YPGOSL002	Moraine	Quershan	OSL	32.1187	98.8543	3981	18.4	1.4	Xu et al., 2010
267	YPGOSL003	Moraine	Quershan	OSL	32.1185	98.8542	3985	24.3	2.0	Xu et al., 2010
268	YPGOSL004	Moraine	Quershan	OSL	32.1180	98.8538	3987	20.5	2.0	Xu et al., 2010
269	ZQXOSL001	Moraine	Quershan	OSL	32.1315	98.8555	3895	53.1	4.5	Xu et al., 2010
270	ZQDEOSL00	Moraine	Quershan	OSL	32.1240	98.8700	3972	62.4	5.2	Xu et al., 2010
271	ZQDEOSL00	Moraine	Quershan	OSL	32.1252	98.8703	3972	48.6	4.1	Xu et al., 2010
272	YP001	Moraine	Quershan	OSL	32.1167	98.8500*	4000	0.36	0.03	Ou et al., 2014
273	YP002	Moraine	Quershan	OSL	32.1167	98.8500*	4000	15.3	1.5	Ou et al., 2014
274	YP101	Moraine	Quershan	OSL	32.1167	98.8500*	4000	1.92	0.20	Ou et al., 2014
275	YP102	Moraine	Quershan	OSL	32.1167	98.8500*	4000	18.8	1.8	Ou et al., 2014
276	YP201	Moraine	Quershan	OSL	32.1167	98.8500*	4000	1.79	0.13	Ou et al., 2014
277	YP306	Moraine	Quershan	OSL	32.1167	98.8500*	4000	12.2	1.1	Ou et al., 2014
278	YP307	Moraine	Quershan	OSL	32.1167	98.8500*	4000	16.2	1.4	Ou et al., 2014
279	YP318	Moraine	Quershan	OSL	32.1167	98.8500*	4000	22.1	1.7	Ou et al., 2014
280	YP308	Moraine	Quershan	OSL	32.1167	98.8500*	4000	20.9	1.7	Ou et al., 2014
281	YP301	Moraine	Quershan	OSL	32.1167	98.8500*	4000	22.2	1.7	Ou et al., 2014
282	YP309	Moraine	Quershan	OSL	32.1167	98.8500*	4000	19.7	1.4	Ou et al., 2014
283	YP319	Moraine	Quershan	OSL	32.1167	98.8500*	4000	16.6	1.3	Ou et al., 2014
284	YP402	Moraine	Quershan	OSL	32.1167	98.8500*	4000	20.1	1.8	Ou et al., 2014
285	YP320c	Moraine	Quershan	OSL	32.1167	98.8500*	4000	51.3	3.9	Ou et al., 2014
286	YP310	Moraine	Quershan	OSL	32.1167	98.8500*	4000	42.8	3.8	Ou et al., 2014
287	YP305	Moraine	Quershan	OSL	32.1167	98.8500*	4000	50.9	4.5	Ou et al., 2014
288	YP304	Moraine	Quershan	OSL	32.1167	98.8500*	4000	61.8	5.5	Ou et al., 2014
289	YP302	Moraine	Quershan	OSL	32.1167	98.8500*	4000	41.2	3.1	Ou et al., 2014
290	DZ301	Moraine	Quershan	OSL	32.1000	98.9000	3985	16.5	1.3	Ou et al., 2013
291	DZ302	Moraine	Quershan	OSL	32.1000	98.9000	3967	16.3	1.3	Ou et al., 2013
292	DZ303	Moraine	Quershan	OSL	32.1000	98.9000	3962	24.7	2.0	Ou et al., 2013
293	DZ304	Moraine	Quershan	OSL	32.1000	98.9000	3938	20.7	1.8	Ou et al., 2013
294	DZ305	Moraine	Quershan	OSL	32.1000	98.9000	3954	22.4	2.2	Ou et al., 2013
295	DZ306	Moraine	Quershan	OSL	32.1000	98.9000	3886	47.3	4.7	Ou et al., 2013
296	DZ307	Moraine	Quershan	OSL	32.1000	98.9000	3886	54.0	4.7	Ou et al., 2013
297	DZ301	Moraine	Quershan	OSL	32.0753	98.9203	3985	16.5	1.3	Zhang et al., 2012
298	DZ302	Moraine	Quershan	OSL	32.0782	98.9230	3967	16.3	1.3	Zhang et al., 2012
299	DZ303	Moraine	Quershan	OSL	32.0976	98.9126	3962	24.7	2.0	Zhang et al., 2012
300	DZ304	Moraine	Quershan	OSL	32.1075	98.9057	3938	20.7	1.8	Zhang et al., 2012
301	DZ305	Moraine	Quershan	OSL	32.1149	98.8979	3954	22.4	2.2	Zhang et al., 2012
302	DZ307	Moraine	Quershan	OSL	32.1296	98.8809	3886	54.0	4.7	Zhang et al., 2012
303	CNL-TL-1	Fluvial terrance	Daofu	OSL	30.6510	101.4090*	3625	12.1	2.1	Chen et al., 2010
304	LDB-TL-2	Fluvial terrance	Daofu	OSL	30.7411	101.3389*	3913	23.3	2.0	Chen et al., 2010
305	P-TL-3	Fluvial terrance	Luding	OSL	29.6262	102.1126*	1665	9.1	1.0	Chen et al., 2010
306	PX-TL-3	Fluvial terrance	Puxiong	OSL	28.4943	102.6302*	2015	13.5	1.4	Chen et al., 2010
307	PX-TL-3	Fluvial terrance	Puxiong	OSL	28.4943	102.6302*	2015	11.8	1.2	Chen et al., 2010
308	PX-TL-6	Fluvial terrance	Puxiong	OSL	28.4875	102.6263*	1934	10.9	1.0	Chen et al., 2010
309	SLK-TL-06	Fluvial terrance	Daofu	OSL	30.2664	101.5231*	3572	7.4	0.8	Chen et al., 2010
310	SMK-TL-2	Fluvial terrance	Shimian	OSL	29.1194	102.4442*	1641	25.2	2.0	Chen et al., 2010
311	TJX-TL-3	Fluvial terrance	Kangding	OSL	30.4809	102.2778*	2428	20.0	1.7	Chen et al., 2010
312	XYL-TL-1	Fluvial terrance	Kangding	OSL	29.9684	101.9583*	2924	9.1	0.7	Chen et al., 2010
313	ZS-TL-1	Fluvial terrance	Zheduoshan	OSL	30.0748	101.8071*	4308	16.4	1.3	Chen et al., 2010
314	DHZ-C-1	Organic sediment	Kangding	14C	29.9110	101.9930*	3771	7.1	0.2	Chen et al., 2010
315	JLC-03	Organic sediment	Jiulong	14C	29.2423	101.4650*	3808	4.5	0.1	Chen et al., 2010
316	JLC-C-2	Organic sediment	Daofu	14C	30.3768	101.5779*	3814	2.7	0.1	Chen et al., 2010

Continued

317	JLC-C-3	Organic sediment	Daofu	14C	30.3791	101.5790*	3809	1.8	0.1	Chen et al., 2010
318	LDB-C-1	Organic sediment	Daofu	14C	30.7434	101.3306*	3864	2.6	0.2	Chen et al., 2010
319	LDB-C-2	Organic sediment	Daofu	14C	30.7434	101.3306*	3864	1.8	0.1	Chen et al., 2010
320	SLK-C-1	Organic sediment	Daofu	14C	30.2664	101.5231*	3572	1.2	0.1	Chen et al., 2010
321	SLK-C-2	Organic sediment	Daofu	14C	30.2664	101.5231*	3572	1.4	0.1	Chen et al., 2010
322	ZT-C-1	Organic sediment	Kangding	14C	29.9897	101.8876*	3194	2.3	0.2	Chen et al., 2010
323	C07	Organic sediment	Kangding	14C	29.9299	101.9823*	3675	3.6	0.1	Yan et al., 2017
324	C08	Organic sediment	Kangding	14C	29.9299	101.9823*	3675	15.3	0.1	Yan et al., 2017
325	C10	Organic sediment	Kangding	14C	29.9299	101.9823*	3675	2.6	0.1	Yan et al., 2017
326	C11	Organic sediment	Kangding	14C	29.9299	101.9823*	3675	3.9	0.1	Yan et al., 2017
327	C12	Organic sediment	Kangding	14C	29.9299	101.9823*	3675	4.0	0.1	Yan et al., 2017
328	C15	Organic sediment	Kangding	14C	29.9381	101.9811*	3558	1.2	0.1	Yan et al., 2017
329	C16	Organic sediment	Kangding	14C	29.9381	101.9811*	3558	2.3	0.1	Yan et al., 2017
330	C17	Organic sediment	Kangding	14C	29.9381	101.9811*	3558	2.1	0.1	Yan et al., 2017
331	C19	Organic sediment	Kangding	14C	29.9381	101.9811*	3558	2.6	0.1	Yan et al., 2017
332	KZR01	Moraine	Daocheng	ESR	29.1267	100.2175	3871	21.7	1.5	Xu and Zhou, 2009
333	KZR02	Moraine	Daocheng	ESR	29.1267	100.2175	3997	134.2	17.6	Xu and Zhou, 2009
334	KZR03	Moraine	Daocheng	ESR	29.1267	100.2175	4098	41.1	4.7	Xu and Zhou, 2009
335	KZR04	Moraine	Daocheng	ESR	29.1267	100.2175	4087	46.1	4.4	Xu and Zhou, 2009
336	KZR05	Moraine	Daocheng	ESR	29.1267	100.2175	4082	26.3	2.9	Xu and Zhou, 2009
337	KZR06	Moraine	Daocheng	ESR	29.1267	100.2175	4150	16.2	1.6	Xu and Zhou, 2009
338	KZR07	Moraine	Daocheng	ESR	29.1267	100.2175	4134	22.1	2.5	Xu and Zhou, 2009
339	KZR09	Moraine	Daocheng	ESR	29.1267	100.2175	4078	39.4	5.3	Xu and Zhou, 2009
340	YZK01	Moraine	Daocheng	ESR	29.1267	100.2175	3772	20.2	3.5	Xu and Zhou, 2009
341	YZK02	Moraine	Daocheng	ESR	29.1267	100.2175	3774	16.4	1.4	Xu and Zhou, 2009
342	YZK03	Moraine	Daocheng	ESR	29.1267	100.2175	3801	135.1	10.4	Xu and Zhou, 2009

* Sampling locations are derived from the geological map in the references.

Supplementary table 5. Summary of published fluvial incision rates data.

Number	Sample	Type	Location	Method	Latitude (N)	Longitude (E)	River elevation (m)	Incision rate (mm/yr)	Age (ka)	Error (ka)	References
1	OSL-D005-1	Sediment	Yalong	OSL	26.6114	101.8006	38	2.09	18.19	1.89	He et al., 2015
2	OSL-D002-5	Sediment	Yalong	OSL	26.6222	101.8017	38	1.74	21.89	2.34	He et al., 2015
3	OSL-D079-1	Sediment	Yalong	OSL	28.2800	102.1847	97	2.36	41.1	5.12	He et al., 2015
4	OSL-D106-1	Sediment	Yalong	OSL	28.2800	102.1847	24	1.09	22.08	3.01	He et al., 2015
5	OSL-D115-1	Sediment	Yalong	OSL	27.4203	102.1881	66	1.05	63.06	6.53	He et al., 2015
6	MJ-1	Sediment	Minjiang	ESR	31.4750	103.5670	172	0.38	450	102	Liu et al., 2013
7	MJ-2	Sediment	Minjiang	ESR	31.4750	103.5670	172	0.43	396	127	Liu et al., 2013
8	MJ-3	Sediment	Minjiang	ESR	31.4750	103.5670	153	1.06	145	29	Liu et al., 2013
9	MJ-4	Sediment	Minjiang	ESR	31.4750	103.5670	153	1.07	143	38	Liu et al., 2013
10	MJ-5	Sediment	Minjiang	ESR	31.4750	103.5670	153	0.89	171	34	Liu et al., 2013
11	MJ-6	Sediment	Minjiang	ESR	31.4750	103.5670	101	1.00	101	15	Liu et al., 2013
12	MJ-7	Sediment	Minjiang	ESR	31.4750	103.5670	75	1.17	64	19	Liu et al., 2013
13	LH10	Sediment	Luhuo	ESR	31.3720	100.7050	165	1.76	94	14.1	Zhao et al., 2013
14	LH09	Sediment	Luhuo	ESR	31.3720	100.7050	265	1.02	261	39.15	Zhao et al., 2013
15	LH08	Sediment	Luhuo	ESR	31.3720	100.7050	295	0.77	384	57.6	Zhao et al., 2013
16	LH07	Sediment	Luhuo	ESR	31.3720	100.7050	335	0.73	462	69.3	Zhao et al., 2013
17	LH06	Sediment	Luhuo	ESR	31.3720	100.7050	365	0.61	598	89.7	Zhao et al., 2013
18	LX09	Sediment	Zagunao	ESR	31.4500	103.1700	17	0.31	54	8.1	Liu et al., 2006
19	LX08	Sediment	Zagunao	ESR	31.4500	103.1700	37	0.30	125	18.75	Liu et al., 2006
20	LX07	Sediment	Zagunao	ESR	31.4500	103.1700	60	0.24	248	37.2	Liu et al., 2006
21	LX05	Sediment	Zagunao	ESR	31.4500	103.1700	210	0.44	481	72.15	Liu et al., 2006
22	Lower T3	Sediment	Jinsha	OSL	28.2430	99.3160	79	1.32	59.8	16.9	Chen et al., 2008
23	Unit 12	Sediment	Jinsha	OSL	28.2430	99.3160	45	4.25	10.6	1.9	Chen et al., 2008
24	Upper T1	Sediment	Jinsha	OSL	28.2430	99.3160	28	4.38	6.4	1.8	Chen et al., 2008
25	YN-2	Sediment	Yulong	10Be	27.3064	100.2111	295	13.92	21.2	1.5	Kong et al., 2009
26	YN-9	Sediment	Yulong	10Be	27.3042	100.2058	305	11.38	26.8	2.2	Kong et al., 2009
27	YN-29	Sediment	Yulong	10Be	27.3031	100.2117	360	16.51	21.8	1.7	Kong et al., 2009
28	YN-34	Sediment	Yulong	10Be	27.3194	100.2417	250	12.89	19.4	1.5	Kong et al., 2009
29	YN-5	Sediment	Yulong	10Be	27.3025	100.2233	233	8.83	26.4	2.1	Kong et al., 2009
30	YN-6	Sediment	Yulong	10Be	27.3025	100.2233	233	8.35	27.9	2.1	Kong et al., 2009
31	YN-7	Sediment	Yulong	10Be	27.3103	100.2294	210	7.32	28.7	3.4	Kong et al., 2009
32	YN-11	Sediment	Yulong	10Be	27.3028	100.2267	226	7.96	28.4	2.0	Kong et al., 2009
33	YN-15	Sediment	Yulong	10Be	27.3139	100.2411	145	8.19	17.7	1.4	Kong et al., 2009
34	YN-16	Sediment	Yulong	10Be	27.3139	100.2411	145	7.63	19.0	1.5	Kong et al., 2009
35	YN-30	Sediment	Yulong	10Be	27.3217	100.2408	100	8.85	11.3	1.6	Kong et al., 2009
36	YN-31	Sediment	Yulong	10Be	27.3217	100.2408	90	9.89	9.1	1.0	Kong et al., 2009
37	YN-32	Sediment	Yulong	10Be	27.3217	100.2408	80	9.64	8.3	0.7	Kong et al., 2009
38	YN-33	Sediment	Yulong	10Be	27.3217	100.2408	80	10.53	7.6	1.0	Kong et al., 2009
39	MK14-01	Sediment	Mangkang	OSL	29.9652	98.0671	45	0.75	59.9	4.9	Zhang et al., 2018
40	MK14-02	Sediment	Mangkang	OSL	29.9688	98.0642	45	0.51	88.7	6.2	Zhang et al., 2018
41	YJ15-01	Sediment	Deqin	OSL	29.0216	98.6042	177	1.99	89.1	6.0	Zhang et al., 2018
42	YJ15-02	Sediment	Deqin	OSL	28.9808	98.6311	168	1.68	100.2	14.7	Zhang et al., 2018
43	DQ14-02	Sediment	Deqin	OSL	28.4556	98.8307	155	1.74	89.1	6.3	Zhang et al., 2018
44	XD15-01	Sediment	Deqin	OSL	28.4525	98.8344	16	1.03	15.6	0.7	Zhang et al., 2018
45	DQ14-03	Sediment	Deqin	OSL	28.3717	98.8634	10	1.11	9.0	0.3	Zhang et al., 2018
46	YL15-01	Sediment	Deqin	OSL	28.2983	98.8654	143	1.23	116.6	13.0	Zhang et al., 2018
47	DQ14-05	Sediment	Deqin	OSL	28.2833	98.8625	104	1.21	86.0	5.0	Zhang et al., 2018
48	DQ14-04	Sediment	Deqin	OSL	28.2910	98.8600	104	2.69	38.6	3.0	Zhang et al., 2018
49	TE15-07	Sediment	Yunlong	OSL	26.1648	99.1260	284	2.83	100.4	5.1	Zhang et al., 2018
50	TE15-08	Sediment	Yunlong	OSL	26.1632	99.1322	166	2.34	71.0	6.7	Zhang et al., 2018
51	LM197b	Charcoal	Jianjiang	14C	31.1455	103.8423*	27	1.70	15.9	0.4	Godard et al., 2010

Continued

52	LM197c	Charcoal	Jianjiang	14C	31.1455	103.8423*	27	0.81	33.5	0.4	Godard et al., 2010
53	LM206c	Charcoal	Jinhe	14C	31.3527	104.0326*	57	1.36	41.8	0.4	Godard et al., 2010
54	LM220c	Shell	Minjiang	14C	31.4021	103.5275*	16	0.80	20.1	0.2	Godard et al., 2010
55	LM230	Shell	Minjiang	14C	31.3954	103.5244*	16	0.77	20.8	0.4	Godard et al., 2010
56	SC021	Boulder	Minjiang	10Be	31.2394	103.7781*	10	0.45	22.4	8.3	Godard et al., 2010
57	LM212	Sediment	Minjiang	OSL	31.0118	103.6030*	75	0.50	150	25	Godard et al., 2010

* Sampling locations are derived from the geological map in the references.

Ackerer, J., Chabaux, F., Van der Woerd, J., Viville, D., Pelt, E., Kali, E., Lerouge, C., Ackerer, P., di Chiara Roupert, R., Négrel, P., 2016. Regolith evolution on the millennial timescale from combined U–Th–Ra isotopes and in situ cosmogenic ^{10}Be analysis in a weathering profile (Strengbach catchment, France). Earth and Planetary Science Letters 453, 33-43.

Ansberque, C., Godard, V., Bellier, O., De Sigoyer, J., Liu-Zeng, J., Xu, X., Ren, Z., Li, Y., Team, A.S.T.E.R., 2015. Denudation pattern across the Longriba fault system and implications for the geomorphological evolution of the eastern Tibetan margin. Geomorphology 246, 542-557.

Bai, M., Chevalier, M.-L., Pan, J., Replumaz, A., Leloup, P.H., Métois, M., Li, H., 2018. Southeastward increase of the late Quaternary slip-rate of the Xianshuihe fault, eastern Tibet. Geodynamic and seismic hazard implications. Earth and Planetary Science Letters 485, 19-31.

Chen, G., Xu, X., Yuan, R., Wen, X., Zheng, R., 2010. Late Quaternary climate and geomorphology on the northeastern margin of Sichuan-Yunnan block and their tectonomorphologic significance. Quaternary Sciences 30, 837-854 (in Chinese with English abstract).

Chen, J., Dai, F., Yao, X., 2008. Holocene debris-flow deposits and their implications on the climate in the upper Jinsha River valley, China. Geomorphology 93, 493-500.

Chevalier, M.-L., Leloup, P.H., Replumaz, A., Pan, J., Métois, M., Li, H., 2017. Temporally constant slip rate along the Ganzi fault, NW Xianshuihe fault system, eastern Tibet. Geological Society of America Bulletin 130, 396-410.

Cook, K.L., Hovius, N., Wittmann, H., Heimsath, A.M., Lee, Y.-H., 2018. Causes of rapid uplift and exceptional topography of Gongga Shan on the eastern margin of the Tibetan Plateau. Earth and Planetary Science Letters 481, 328-337.

Fu, P., Stroeven, A.P., Harbor, J.M., Hättestrand, C., Heyman, J., Caffee, M.W., Zhou, L., 2013. Paleoglaciation of Shaluli Shan, southeastern Tibetan Plateau. Quaternary Science Reviews 64, 121-135.

Godard, V., Lavé, J., Carcaillet, J., Cattin, R., Bourlès, D., Zhu, J., 2010. Spatial distribution of denudation in Eastern Tibet and regressive erosion of plateau margins. Tectonophysics 491, 253-274.

Graf, A.A., Strasky, S., Zhao, Z., Akcar, N., Ivy-Ochs, S., Kubik, P.W., Christal, M., Kasper, H.U., Wieler, R., Schlüchter, C., 2008. Glacier extension on the eastern Tibetan Plateau in response to MIS 2 cooling, with a contribution to ^{10}Be and ^{21}Ne methodology. In: Strasky, S. (ed.), Glacial response to global climate changes: cosmogenic nuclide chronologies from high and low latitudes. ETH Zürich (PhD Thesis).

Harkins, N., Kirby, E., Heimsath, A., Robinson, R., Reiser, U., 2007. Transient fluvial incision in the headwaters of the Yellow River, northeastern Tibet, China. Journal of Geophysical Research 112, F03S04.

He, Z., Zhang, X., Qiao, Y., Bao, S., Lu, C., He, X., 2015. Formation of the Yalong Downstream Terraces in the SE Tibetan Plateau and Its Implication for the Uplift of the Plateau. Acta Geologica Sinica (English Edition) 89, 542-560.

Henck, A.C., Huntington, K.W., Stone, J.O., Montgomery, D.R., Hallet, B., 2011. Spatial controls on erosion in the Three Rivers Region, southeastern Tibet and southwestern China. Earth and Planetary Science Letters 303, 71-83.

Heyman, J., Stroeven, A.P., Caffee, M.W., Hättestrand, C., Harbor, J.M., Li, Y., Alexanderson, H., Zhou, L., Hubbard, A., 2011. Palaeoglaciology of Bayan Har Shan, NE Tibetan Plateau: exposure ages reveal a missing LGM expansion. Quaternary Science Reviews 30, 1988-2001.

Kirby, E., Harkins, N., 2013. Distributed deformation around the eastern tip of the Kunlun fault. International Journal of Earth Sciences 102, 1759-1772.

Kong, P., Na, C., Fink, D., Zhao, X., Xiao, W., 2009. Moraine dam related to late Quaternary glaciation in the Yulong Mountains, southwest China, and impacts on the Jinsha River. Quaternary Science Reviews 28, 3224-3235.

Liu, C.-R., Yin, G.-M., Zhang, H.-P., Zheng, W.-J., Voinchet, P., Han, F., Wang, D., Song, W.-J., Bahain, J.-J., 2013. ESR geochronology of the Minjiang River terraces at Wenchuan, eastern margin of Tibetan Plateau, China. Geochronometria 40.

Liu, Y., Zhao, Z., Li, C., Zhang, M., Chen, Y., 2006. Formation of the Zagunao River Terraces in Western Sichuan Plateau, China. Acta Geographica Sinica 61, 249-254 (in Chinese with English abstract).

Ou, X., Lai, Z., Zhou, S., Zeng, L., 2014. Timing of glacier fluctuations and trigger mechanisms in eastern Qinghai–Tibetan Plateau during the late Quaternary. Quaternary Research 81, 464-475.

Ou, X., Zhang, B., Lai, Z., Zhou, S., Zeng, L., 2013. OSL dating study on the glacial evolutions during the Last Glaciation at Dangzi Valley in the eastern Qinghai-Tibetan Plateau. Progress in Geography 32, 262-269 (in Chinese with English abstract).

Ouimet, W.B., Whipple, K.X., Granger, D.E., 2009. Beyond threshold hillslopes: Channel adjustment to base-level fall in tectonically active mountain ranges. Geology 37, 579-582.

Owen, L.A., Finkel, R.C., Barnard, P.L., Haizhou, M., Asahi, K., Caffee, M.W., Derbyshire, E., 2005. Climatic and topographic controls on the style and timing of Late Quaternary glaciation throughout Tibet and the Himalaya defined by ^{10}Be cosmogenic radionuclide surface exposure dating. Quaternary Science Reviews 24, 1391-1411.

Owen, L.A., Finkel, R.C., Haizhou, M., Spencer, J.Q., Derbyshire, E., Barnard, P.L., Caffee, M.W., 2003. Timing and style of Late Quaternary glaciation in northeastern Tibet. Geological Society of America Bulletin 115, 1356-1364.

Schäfer, J.M., Tschudi, S., Zhao, Z., Wu, X., Ivy-Ochs, S., Wieler, R., Baur, H., Kubik, P.W., Schlüchter, C., 2002. The limited influence of glaciations in Tibet on global climate over the past 170 000 yr. Earth and Planetary Science Letters 194, 287-297.

Strasky, S., Graf, A.A., Zhao, Z., Kubik, P.W., Baur, H., Schlüchter, C., Wieler, R., 2009. Late Glacial ice advances in southeast Tibet. Journal of Asian Earth Sciences 34, 458-465.

Tschudi, S., Schäfer, J.M., Zhao, Z., Wu, X., Ivy-Ochs, S., Kubik, P.W., Schlüchter, C., 2003. Glacial advances in Tibet during the Younger Dryas? Evidence from cosmogenic ^{10}Be, ^{26}Al, and ^{21}Ne. Journal of Asian Earth Sciences 22, 301-306.

Wang, J., Raisbeck, G.M., Xu, X., Yiou, F., Bai, S., 2006. In situ cosmogenic 10Be dating of the Quaternary glaciations in the southern Shaluli Mountain on the Southeastern Tibetan Plateau. Science in China Series D: Earth Sciences 49, 1291-1298.

Xu, L., Ou, X., Lai, Z., Zhou, S., Wang, J., Fu, Y., 2010. Timing and style of Late Pleistocene glaciation in the Queer Shan, northern Hengduan Mountains in the eastern Tibetan Plateau. Journal of Quaternary Science 25, 957-966.

Xu, L., Zhou, S., 2009. Quaternary glaciations recorded by glacial and fluvial landforms in the Shaluli Mountains, Southeastern Tibetan Plateau. Geomorphology 103, 268-275.

Xu, X., Wang, J., Zhu, J., Jiang, H., Yang, Y., 2004. Study on glacial erosion surface of the southeast of Qinghai-Xizang Plateau using cosmogenic isotopes dating. Scientia Geographica Sinica 24, 101-104 (in Chinese with English abstract).

Yan, B., Lin, A., 2017. Holocene activity and paleoseismicity of the Selaha Fault, southeastern segment of the strike-slip Xianshuihe Fault Zone, Tibetan Plateau. Tectonophysics 694, 302-318.

Zhang, B., Ou, X., Lai, Z., 2012. OSL ages revealing the glacier retreat in the Dangzi valley in the eastern Tibetan Plateau during the Last Glacial Maximum. Quaternary Geochronology 10, 244-249.

Zhang, J., Liu-Zeng, J., Scherler, D., Yin, A., Wang, W., Tang, M., Li, Z., 2018. Spatiotemporal variation of late Quaternary river incision rates in southeast Tibet, constrained by dating fluvial terraces. Lithosphere 10, 662-675.

Zhang, Z., Wang, J., Xu, X., BAI, S., Chang, Z.Y., 2015. Cosmogenic ^{10}Be and ^{26}Al Chronology of the Last Glaciation of the Palaeo-Daocheng Ice Cap, Southeastern Qinghai-Tibetan Plateau. Acta Geologica Sinica (English Edition) 89, 575-584.

Zhao, Z.J., Liu, Y., Chen, Y., Zhang, M.H., Shu, Q., Li, C.L., 2013. Quaternary fluvial incision rates of the Western Sichuan Plateau inferred from ESR chronology. Journal of Lanzhou University 49, 160-172 (in Chinese with English abstract).